



Low Energy Neutrino Reconstruction in IceCube and the ICU

Master's Thesis

THOMAS S. HALBERG

Advisor: D. Jason Koskinen

Co-advisor: Tom Stuttard

September 3, 2019

Abstract

Thomas Schandorf HALBERG

Low Energy Neutrino Reconstruction in IceCube and the ICU

The upcoming Upgrade for the IceCube Neutrino Observatory will in 2022-23 deploy seven new strings featuring multi-PMT optical modules and new calibration devices, enhancing the sensitivity to $O(1-100)$ GeV neutrinos used in atmospheric neutrino oscillation measurements. Precision reconstruction of neutrino energy and direction is essential to maximizing the sensitivity of these oscillation analyses. Technical challenges are met when applying current reconstruction methods to the new detector hardware, as previous symmetries in the detector required by the method break.

Here a likelihood-based reconstruction method where neutrino event hypotheses are generated using direct simulation is presented. The direct reconstruction method is independent of symmetries in the detector, with the ability to fully utilize the new instrumentation and realistic ice models in the IceCube Upgrade.

The direct reconstruction method has been tested on Monte Carlo simulated event samples in DeepCore, the existing low energy extension of IceCube, and the IceCube Upgrade. In DeepCore, direct reconstruction has shown a performance close to the current reconstruction method. Although the successful reconstruction of events using the direct simulation method has been achieved during this work, both for DeepCore and the Upgrade, detailed investigations have revealed a number of limitations and challenges of the present implementation. These include the stability of the likelihood space, unexpected behavior from time binning of photons, and the execution speed of the algorithm. These issues should be the focus for future work on this technique in the lead-up to the first detector data from the IceCube Upgrade.

Contents

Abstract	ii
1 Neutrino Phenomenology	1
1.1 History of the Neutrino	1
1.2 Neutrino Properties	1
1.3 Neutrino Flavors	2
1.4 The Weak Force	3
1.5 Particle Handedness	4
1.6 Neutrino Oscillation	5
2 Detecting Neutrinos	9
2.1 Cherenkov Radiation	9
2.2 Neutrino-Nucleon Scattering	10
2.3 Electromagnetic and Hadronic Showers	12
2.4 Track-like Events	13
2.5 Atmospheric Neutrinos	14
2.6 Oscillation Analysis	15
3 The IceCube Detector	18
3.1 Digital Optical Module	19
3.2 Ice Properties	22
3.3 DeepCore	23
3.4 IceCube Upgrade	25
4 Simulation	28
4.1 CORSIKA	28
4.2 MuonGun	29
4.3 Simulating Neutrino Interactions	29
4.4 Simulating Light Propagation	30
4.5 PMT Response	31
4.6 Simulating noise	37
5 Neutrino Reconstruction	38
5.1 Impact of Uncertainties in Reconstruction	39
5.2 Reconstruction Parameters	40
5.3 The Likelihood Model	41
5.4 Table Reconstruction	42
5.5 Direct Reconstruction	43
5.6 Spline-tables versus Direct Simulation	45
5.7 Millipede	45

6 Reconstruction Studies	48
6.1 Investigating the Oversampling Factor	48
6.2 Likelihood Scans	52
6.3 Minimizer Movement	54
6.4 Final Reconstruction DeepCore	55
6.5 Direct Reconstruction in the ICU	56
6.6 Determining Reconstruction Settings	57
6.7 Investigating Badly Reconstructed Events	59
6.8 High Oversampling	61
6.9 Future Work	62
7 Conclusion	64
A Minimizer Movement	65
Bibliography	69

1 Neutrino Phenomenology

1.1 History of the Neutrino

One of the most fundamental rules we learn about in physics is the conservation of energy in all possible processes we observe. However, in the years 1910-1920, when physicists observed radioactive beta-decays from natural elements, they discovered a violation of this rule. It was observed that the total energy before and after the radioactive decay was not equal, as the total energy of emitted particles was lower than the particle that produced them. It was as if some of the energy had just disappeared.

In December 1930 Wolfgang Pauli proposed a solution to the missing energy problem[1]. The idea was the addition of a new invisible particle, which was created together with the electron and was carrying away energy. Even though it was a big claim, it was quickly adopted by the community, and in 1933, Enrico Fermi wrote the theory that implemented this new particle[2]. He named it *neutrino*, which means *little neutral* in Italian, and it's noted by the Greek letter ν .

1.2 Neutrino Properties

The neutrino is a subatomic particle and is currently one of the least understood particles in the Standard Model. It is the lightest subatomic particle with a non-zero rest mass. The neutrino is part of the lepton family but distinguishes itself from the other leptons by being neutral, as opposed to the electron, muon, and tau that all carry an electric charge.

Since it is neutral, it does not interact via the electromagnetic force, and by being a lepton, it does not interact via the strong nuclear force either. Neutrinos interact via the weak nuclear force and gravity, though the coupling strength of gravity is so weak that it can be neglected. This leaves only the weak force, and as the name suggests, this interaction is weak in comparison to the electromagnetic and strong forces. Because neutrinos interact so weakly with matter, they are very difficult to observe and are often called "ghost-particles" because they propagate through matter as if it was not there at all.

While neutrinos often get associated with being very difficult to observe, it is not due to the lack of their numbers. Neutrinos are some of the most abundant particles in our universe. They are so plentiful that about 100 trillion of them pass through our bodies every second here on Earth, and it would take, on average, 100 years for a neutrino to interact with a human.

Many of them are produced in nuclear fusion processes in the Sun, typically referred to as *solar neutrinos*, while others come from radioactive decay processes. Neutrino beams of high intensity can be generated using accelerators and is a popular method used for studying them. In addition, neutrinos are constantly being created from cosmic ray interactions in our atmosphere.

The elusive nature of neutrinos make them very challenging to study, but it also makes them excellent astrophysical messengers, enabling us to probe the far reaches of

the universe, as their trajectory is not disturbed by astrophysical magnetic fields and dust. If neutrinos can be observed, and their trajectory reconstructed, it would be possible to trace them back to their source.

1.3 Neutrino Flavors

Since the first discovery of the neutrino, two additional neutrino flavors have been observed. Each neutrino flavor is associated with one of the charged leptons e , μ , and τ , and are noted by ν_l , with the subscript l indicating the lepton flavor. Experiments measuring Z boson decays using the electron-positron colliders SCL and LEP reported a best fit value of $N_\nu = 2.9840 \pm 0.0082$ [3] for the number of active light neutrinos, which is in good agreement with the three flavors that have been observed. Neutrinos are part of the Standard Model of particle physics and are shown in the bottom left of Figure 1.1, immediately below their associated leptonic partner.

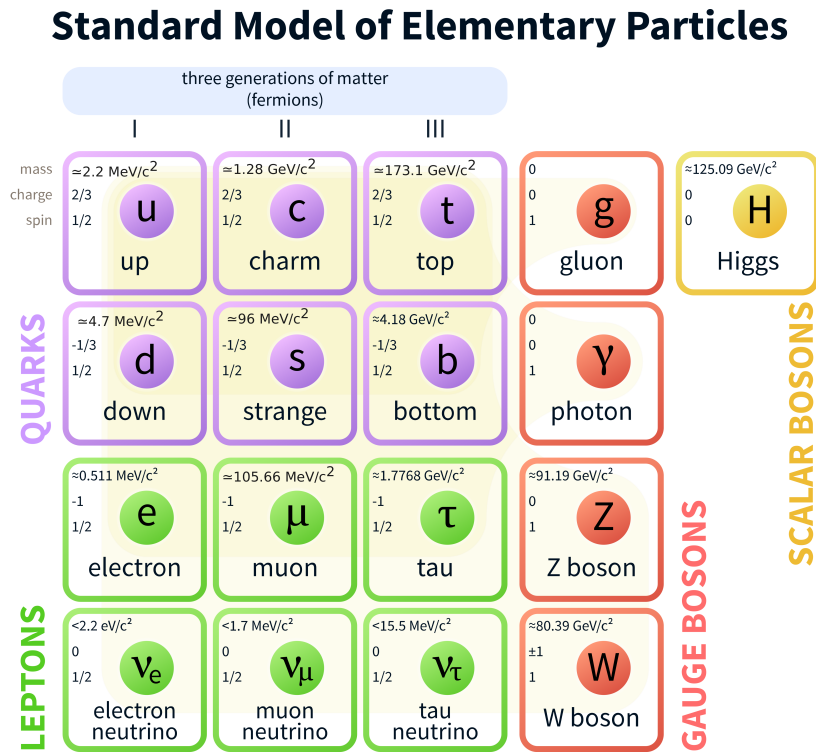


FIGURE 1.1: The Standard Model of elementary particles. The neutrinos can be seen in the bottom left, immediately below their associated leptonic partners.

All leptons (including neutrinos) have an associated lepton number (lepton charge). The lepton number takes values of ± 1 and there is a unique lepton number for each lepton flavor, noted by L_l with l indicating the flavor. The lepton number is shared by the neutrino-lepton pairs. The lepton number is important as it determines the possible interactions involving leptons, e.g. in neutrino-nucleon scattering

$$\nu_l + N \rightarrow l + N', \quad (1.1)$$

where ν_l is a neutrino with flavor l and N is a nucleon. For interaction to be allowed, the lepton number must be conserved on both sides of the equation. The conservation of lepton number is true in point-like neutrino interactions, but it is not universally conserved property. Neutrinos have been observed changing flavors as they propagate through

Neutrino	Lepton	L_l	L
$\nu_e(\bar{\nu}_e)$	$e^-(e^+)$	L_e	$1(-1)$
$\nu_\mu(\bar{\nu}_\mu)$	$\mu^-(\mu^+)$	L_μ	$1(-1)$
$\nu_\tau(\bar{\nu}_\tau)$	$\tau^-(\tau^+)$	L_τ	$1(-1)$

TABLE 1.1: Relationship between neutrinos and charged leptons, including their lepton number.

space, known as neutrino oscillation, which in turn break the conservation of lepton number.

Each of the three neutrino flavors have an associated anti-particle (anti-neutrino), i.e. $\bar{\nu}_e$, $\bar{\nu}_\mu$ and $\bar{\nu}_\tau$, for which the associated leptons become e^+ , μ^+ , and τ^+ . Anti-leptons (including anti-neutrinos) have identical lepton numbers, but with the sign reversed e.g. $\bar{\nu}_e$ have lepton number $L_e = -1$ (see table 1.1 for more). This property allows for interactions such a neutron decay,



where the sum of lepton numbers from the e^- and $\bar{\nu}_e$ equals 0, conserving the lepton number on both sides.

1.4 The Weak Force

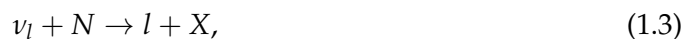
The weak force is mediated by two exchange particles, the Z^0 and W^\pm bosons. The W boson has a charge of either plus or minus 1, while the Z^0 boson is electrically neutral.

The W^+ and W^- bosons are involved in interactions that include neutrino emission and absorption and are known as charged current (CC) interactions. CC interactions in neutrino-nucleon scattering involve quarks changing flavor, as well as the production of a charged lepton in place of the neutrino. The flavor of the charged lepton is highly dependent on the flavor of the neutrino.

Weak interactions mediated by the Z^0 boson are called neutral current (NC) interactions since no transfer of electric charge is involved. Instead, NC interactions involve the transfer properties such as the energy, spin, and momentum. However, above neutrino energies of a few GeV NC interactions can destroy the nucleon, creating a shower of hadronic particles in the process.

The W^\pm and Z^0 bosons are heavy particles, with masses of around 80 GeV and 91 GeV respectively. In weak interactions, as the bosons are exchanged they are, what is known as, *virtual particles* that are spontaneously created to mediate the weak force. As this is violating conservation of energy, it is only allowed because of the uncertainty principle stating $\Delta t \Delta E \leq \hbar/2$. From this principle, given a very short interaction time, the uncertainty in energy can be very large. As a result, the W^\pm and Z^0 boson created in weak interactions are very short-lived, in turn making the interaction range short as well. The range of the weak interaction is about 1/1000 times the diameter of a proton.

In neutrino-nucleon scattering a CC interaction is described as



where ν_l is a neutrino of flavor l , N is a nucleon, l is a lepton, and X is one or more hadrons. NC interactions from neutrino-nucleon scattering can be described as

$$\nu_l + N \rightarrow \nu_l + X. \quad (1.4)$$

1.5 Particle Handedness

Particles have a quantum property called *spin*, which is especially important in neutrino interactions for reasons that will soon be described. Spin defines a particles *handedness*. The handedness depend on the direction of the particles spin in relation to its direction of motion. If a particles spin-direction is parallel to its motion, the particle is considered *right-handed*, while in the case where they are anti-parallel the particle is considered *left-handed*. An illustration of handedness is shown in Figure 1.2.

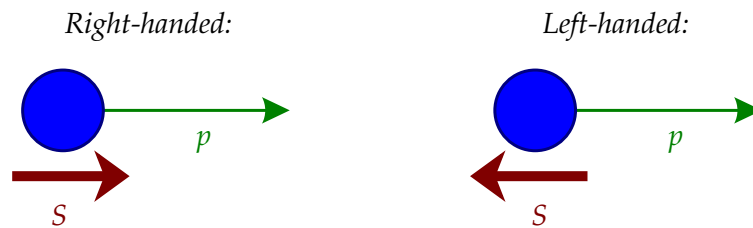


FIGURE 1.2: Illustration of handedness (helicity). When the spin of a particle is pointing in the same direction as its motion, the particle is said to be right-handed as seen on the right. A particle is left-handed if the spin direction is opposite to its motion as seen on the left. Figure taken from [4].

For massless particles the handedness of a particle is invariant, as massless particles move at the speed of light. However, for massive particles, if the reference frame moves at speeds exceeding that of the particle, the handedness will be observed to *flip* to the opposite handedness.

Chirality is a property closely related to particle handedness but is defined using inherent quantum properties of the particle, making it invariant to the reference frame. For massless particles the handedness and the chirality is the same. However, for massive particles handedness and chirality must be distinguished, as the handedness of a massive particle can change depending on the reference frame.

The weak force is different from the other forces as it has a preference for particle handedness. It was first discovered during a famous experiment in 1956 by physicist Chien-Shiung Wu, who studied the decay of cobalt-60 atoms[5]. The experiment involved cooling cobalt-60 atoms to near absolute zero and aligning their spin using a strong magnetic field. As the cobalt-60 atoms decay, the direction of the emitted electron was measured, and the results showed that electrons were emitted in the same directing for all of decays.

As the spin of the system must be conserved, the spin of the electron and $\bar{\nu}_e$ from the decay must have the same spin. Since the momentum of the system must be conserved as well, the direction of the two particles must be opposite of each other. This resulted in only left-handed neutrinos being produced in the decay, showing the strong preference of handedness in weak interactions. Since neutrinos only interact via the weak force, no right-handed neutrinos or left-handed anti-neutrinos have ever been observed. However, this does not conclude whether right-handed neutrinos or left-handed anti-neutrinos exist, but rather that we are not able to measure them, as they do not interact.

1.6 Neutrino Oscillation

Neutrino oscillation is the phenomena in which a neutrino produced with one flavor can later be observed with a different flavor. As neutrinos propagate through space, they oscillate between different flavors. The oscillation probability of the neutrino depends on several factors, most notably the initial flavor state, the energy of the neutrino, and how far it has propagated. That neutrinos oscillate came as a surprise when it was first discovered, since it requires neutrinos having a mass, while the Standard Model of particle physics was formulated assuming neutrinos having zero mass [6].

1.6.1 Neutrino Masses

The three know flavors (ν_e , ν_μ , and ν_τ) are related to the three mass states (ν_1 , ν_2 , and ν_3) by the Pontecorvo-Marki-Nakagawa-Sakata (PMNS) matrix

$$\begin{pmatrix} \nu_e \\ \nu_\mu \\ \nu_\tau \end{pmatrix} = \begin{bmatrix} U_{e1} & U_{e2} & U_{e3} \\ U_{\mu1} & U_{\mu2} & U_{\mu3} \\ U_{\tau1} & U_{\tau2} & U_{\tau3} \end{bmatrix} \begin{pmatrix} \nu_1 \\ \nu_2 \\ \nu_3 \end{pmatrix} \quad (1.5)$$

where each element of the matrix represents the mixing of flavor state and a mass state, e.g., the fraction of the flavor state ν_e in ν_2 is defined by the matrix element $|U_{e2}|^2$. If there were no mixing of the flavor states and mass states, i.e., all off-diagonal in Equation (1.5) equal to 0, there would be no neutrino oscillation.

The two mass states, ν_1 and ν_2 are very close in mass, while ν_3 is either a lot heavier or a lot lighter than the two other. The normal mass hierarchy is defined as $\nu_1, \nu_2 \ll \nu_3$, while the inverted mass hierarchy is defined as $\nu_1, \nu_2 \gg \nu_3$. In Figure 1.3 the normal and inverted mass hierarchy is illustrated along with the fraction of each mass state in different flavors.

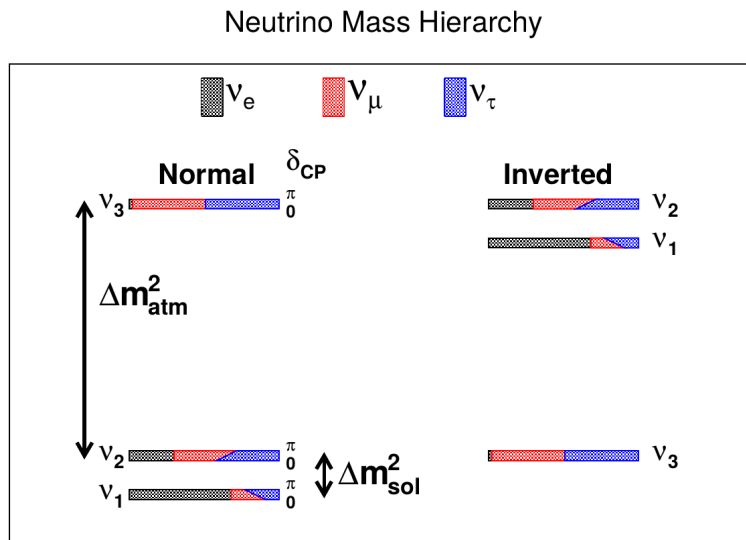


FIGURE 1.3: The neutrino mass hierarchy. The color indicates the fraction of a mass state present in a neutrino flavor [7].

1.6.2 Three Flavor Oscillation Model

Neutrinos are created in a pure flavor eigenstate that can be written in terms of the mass eigenstates

$$|\nu_\alpha\rangle = \sum_j U_{\alpha j}^* |\nu_j\rangle \quad (1.6)$$

where α notes the flavor eigenstate and j notes the mass eigenstate. However, since neutrinos oscillate, they do not remain in their pure flavor eigenstate. Equation (1.6) describes a neutrino at a particular moment in time, but for a neutrino propagating through space, the time evolution of the state is described as

$$|\nu, t\rangle = \sum_j U_{\alpha j}^* e^{-iE_j t} |\nu_j\rangle \quad (1.7)$$

where E_j is the total energy of the j th mass eigenstate defined as $E_j = \sqrt{p^2 + m_j^2}$. The probability of a neutrino interacting as one of the three flavors thus depends on the initial flavor eigenstate and the time experienced by the neutrino. The probability of a neutrino starting in the flavor eigenstate α and interacting as the flavor β is described as

$$P(\nu_\alpha \rightarrow \nu_\beta) = |\langle \nu_\beta, 0 | \nu_\alpha, t \rangle|^2 = \left| \sum_j U_{\beta j} U_{\alpha j}^* e^{-iE_j t} |\nu_j\rangle \right|^2 \quad (1.8)$$

The expression in Equation (1.8) can be expanded by explicitly including the complex conjugate

$$P(\nu_\alpha \rightarrow \nu_\beta) = \sum_i U_{\beta i}^* U_{\alpha i} \sum_j U_{\alpha j}^* U_{\beta j} e^{-i(E_i - E_j)t} \quad (1.9)$$

The neutrino masses can be assumed very small, motivated by cosmological fits to the sum of the three neutrino masses giving an upper limit of about 0.2 eV[8]. For this reason, neutrinos can be assumed highly relativistic, allowing the approximations $E \gg m_j$ and $t \approx L$, where L is the distance traveled by the neutrino. In addition, the exponential term $e^{-i(E_i - E_j)t}$ in Equation (1.9) can be rewritten using Euler's formula

$$e^{-i(E_i - E_j)t} = 1 - 2 \sin^2 \left(\frac{\Delta m_{ji}^2 L}{4E} \right) + i \sin \left(\frac{\Delta m_{ji}^2 L}{2E} \right) \quad (1.10)$$

where $\Delta m_{ji}^2 = m_j^2 - m_i^2$. The PMNS term in Equation (1.9) can be expanded as

$$\left| \sum_j U_{\beta j} U_{\alpha j}^* \right|^2 = \delta_{\alpha\beta} + 2 \sum_{i < j} \sum_i U_{\beta i}^* U_{\alpha i} U_{\beta j} U_{\alpha j}^* \quad (1.11)$$

where $\delta_{\alpha\beta}$ is the Kronecker delta function. Using Equations (1.10) and (1.11) the oscillation probability can be formulated as

$$\begin{aligned} P(\nu_\alpha \rightarrow \nu_\beta) &= \delta_{\alpha\beta} - 4 \sum_{i < j} \text{Re}(U_{\beta i}^* U_{\alpha i} U_{\beta j} U_{\alpha j}^*) \sin^2 \left(\frac{\Delta m_{ji}^2 L}{4E} \right) \\ &\quad + 2 \sum_{i < j} \text{Im}(U_{\beta i}^* U_{\alpha i} U_{\beta j} U_{\alpha j}^*) \sin \left(\frac{\Delta m_{ji}^2 L}{2E} \right) \end{aligned} \quad (1.12)$$

The imaginary part in Equation (1.12) does not contribute to the oscillation probability. By using simplifications based on the detection energy threshold and energy resolution of neutrino telescopes, as well as assuming mixing between 3 flavors and 3 mass states only, the oscillation probability of an atmospheric ν_μ can be expressed as

$$P(\nu_\mu \rightarrow \nu_\mu) = 1 - 4 \sin^2 \theta_{23} \cos^2 \theta_{13} (1 - \sin^2 \theta_{23} \cos^2 \theta_{13}) \sin^2 \left(\frac{\Delta m_{32}^2 L}{4E} \right) \quad (1.13)$$

$$P(\nu_\mu \rightarrow \nu_e) = 4 \sin^2 \theta_{23} \cos^2 \theta_{13} \sin^2 \theta_{13} \sin^2 \left(\frac{\Delta m_{32}^2 L}{4E} \right) \quad (1.14)$$

$$P(\nu_\mu \rightarrow \nu_\tau) = 4 \sin^2 \theta_{23} \cos^2 \theta_{13} \cos^2 \theta_{23} \cos^2 \theta_{13} \sin^2 \left(\frac{\Delta m_{32}^2 L}{4E} \right) \quad (1.15)$$

where θ is the mixing angle. Figure 1.4 shows the oscillation probability for a muon in a three flavor model, as a function of energy. The probability is shown for three different zenith angles. For atmospheric neutrinos, the zenith angle relates to the baseline distance traveled by the neutrino.

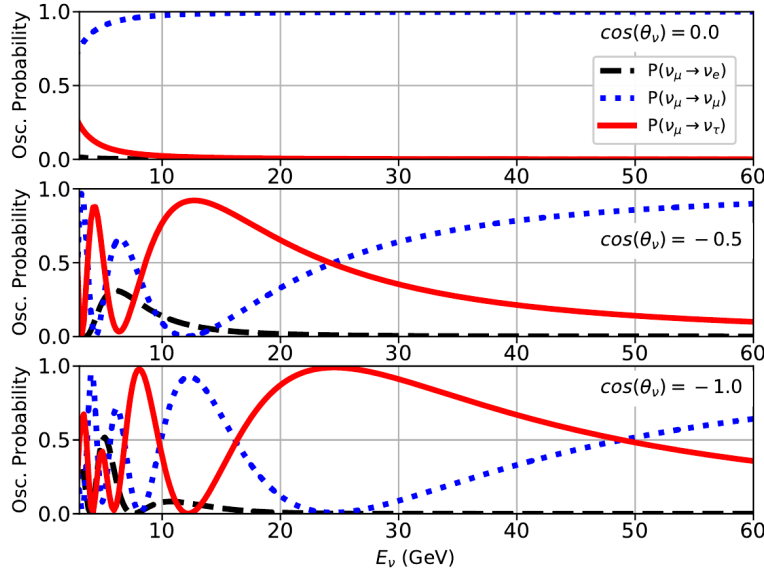


FIGURE 1.4: Oscillation probability of a neutrino with initial flavor ν_μ using a three flavor model, calculated[9] using oscillation input values from [10]. The oscillation probability is shown for three different zenith angles ($\cos(\theta_\nu)$) that relate to the baselines of the neutrino. Here, $\cos(\theta_\nu) = 0$ is horizontal, $\cos(\theta_\nu) = -0.5$ corresponds to 45° , and $\cos(\theta_\nu) = -1$ is directly upwards-going. Figure courtesy of D. Jason Koskinen

The magnitude of $P(\nu_\mu \rightarrow \nu_\mu)$ and $P(\nu_\mu \rightarrow \nu_\tau)$ is mainly driven by θ_{23} , as they both have a very similar dependence on θ_{13} that is relatively small ($\theta_{13} \approx 8.5^\circ$) compared to $\theta_{23} \approx 45^\circ$. Using the approximation $\cos(\theta_{13}) = 1$, $P(\nu_\mu \rightarrow \nu_\mu)$ and $P(\nu_\mu \rightarrow \nu_\tau)$ can effectively be expressed in terms of a single mixing angle θ_{23} , though the underlying matrix elements are still different. This is an important concept, as the $\nu_\mu \rightarrow \nu_\mu$ and $\nu_\mu \rightarrow \nu_\tau$ channels both probe the mixing angle θ_{23} .

From this it becomes feasible to probe the τ -sector in the PMNS matrix, which is very essential since: the oscillation of $\nu_e \rightarrow \nu_\tau$ from atmospheric neutrinos is too small, and measuring $\nu_\tau \rightarrow \nu_{e,\mu,\tau}$ requires a high flux of ν_τ , which is not present naturally on Earth and is hard to produce through experiments. For neutrino experiments that rely

on atmospheric neutrinos, such as IceCube, the oscillation parameters of interest are in general θ_{23} , Δm_{31}^2 , or ν_τ -appearance normalization N_{ν_τ} .

The normalization term, N_{ν_τ} , scales the number of predicted ν_τ in the different observation channels. In IceCube most ν_τ are observed as cascades from either ν_τ NC interactions or ν_τ CC interactions where the τ decay to hadrons (hadronic cascade) or an electron (electromagnetic cascade). However, 17% of the τ from ν_τ CC interactions decay to a μ [11], and is observed as a track. The N_{ν_τ} scaling factor is found by matching the expected contributions from ν_τ in each channel to the observation. A normalization of $N_{\nu_\tau} = 1$ would correspond no discrepancies between theoretical predictions and the observations.

1.6.3 The PMNS Matrix

Under the assumption of unitarity and using a three flavor model, the PMNS matrix from Equation (1.5) can be expressed as

$$\begin{aligned} \begin{pmatrix} \nu_e \\ \nu_\mu \\ \nu_\tau \end{pmatrix} &= \begin{bmatrix} 1 & 0 & 0 \\ 0 & c_{23} & s_{23} \\ 0 & -s_{23} & c_{23} \end{bmatrix} \cdot \begin{bmatrix} c_{13} & 0 & s_{13}e^{-i\delta_{CP}} \\ 0 & 1 & 0 \\ -s_{13}e^{i\delta_{CP}} & 0 & c_{13} \end{bmatrix} \cdot \begin{bmatrix} c_{12} & s_{12} & 0 \\ -s_{12} & c_{12} & 0 \\ 0 & 0 & 1 \end{bmatrix} \begin{pmatrix} \nu_1 \\ \nu_2 \\ \nu_3 \end{pmatrix} \\ &= \begin{bmatrix} c_{13}c_{12} & c_{13}s_{12} & s_{13}e^{-i\delta_{CP}} \\ -c_{23}s_{12} - s_{13}s_{23}c_{12}e^{i\delta_{CP}} & c_{23}c_{12} - s_{13}s_{23}s_{12}e^{i\delta_{CP}} & c_{13}s_{23} \\ s_{23}s_{12} - s_{13}c_{23}c_{12}e^{i\delta_{CP}} & -s_{23}c_{12} - s_{13}c_{23}s_{12}e^{i\delta_{CP}} & c_{13}s_{23} \end{bmatrix} \begin{pmatrix} \nu_1 \\ \nu_2 \\ \nu_3 \end{pmatrix} \end{aligned} \quad (1.16)$$

where $c_{ij} = \cos \theta_{ij}$, $s_{ij} = \sin \theta_{ij}$ and δ_{CP} is the charge-parity phase. The so-called *Majorana phases*, α , and β can be added under the assumption that the neutrino is a Majorana particle, but they are decoupled from neutrino oscillation and so they are neglected here [7].

Each of the three sub-matrices in the first part of Equation (1.16) represents different neutrinos sources (left-to-right: *atmospheric*, *reactor*, *solar*) and are used to measure different portions of the mixing matrix.

2 Detecting Neutrinos

Neutrinos cannot be directly observed as they are neutral particles. They do not leave any trace of their presence unless they interact. What is observed in detectors such as IceCube is the light from charged particles created from neutrino collisions in the ice. As charged particles propagate through the ice photons are emitted through the process of *Cherenkov radiation*, and this is the main source of photon production in IceCube.

2.1 Cherenkov Radiation

When a charged particle moves through a dielectric medium faster than the phase velocity of light in the medium, photons are emitted through Cherenkov radiation. The photons are not emitted by the charged particle itself, but are instead a consequence of the medium being dielectric. As the charged particle propagates, the surrounding atoms in the medium are polarized by the particles electric field, and as a result the electrons are displaced from the nucleus causing a tiny dipole moment. When the particle has passed, the polarized atoms fall back to their original lower energy state, in turn emitting photons in isotropic directions.

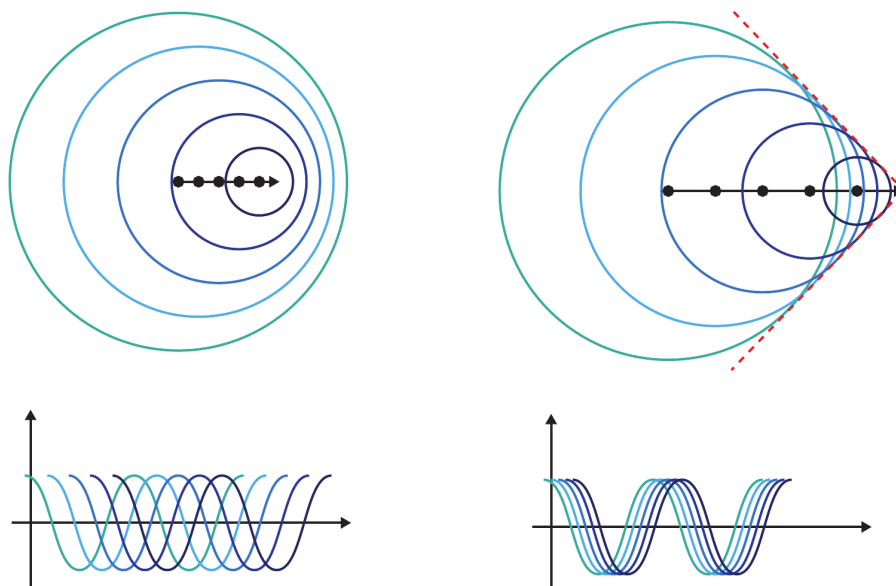


FIGURE 2.1: Illustration of the process of Cherenkov radiation from a charged particle moving in a dielectric medium. (left) Charged particles moving slower than the phase velocity of light, produce photons with small shifts in the phase causing destructive interference. (right) Charged particles moving faster than the phase velocity of light produces photons for which constructive interference creates a wavefront that is observable. Illustration taken from [12]

When the particle is moving slower than the phase velocity of light in the medium, the Cherenkov photons will have a small shift in their phase causing destructive interference, and effectively canceling the effect. This is illustrated in Figure 2.1 (left). When the particle is moving faster than the phase velocity of light, constructive interference of the photons produces a wavefront, as illustrated in Figure 2.1 (right). The wavefront is analogous to the *shock wave* produced by objects moving at supersonic speeds in air. The wavefront produced by the charged particle moves away from the trajectory of the particle at an angle θ_C (the Cherenkov angle), forming a cone of light. The Cherenkov angle θ_C depends on the velocity of the particle, as well as the index of refraction in the medium. The angle can be calculated from the relation

$$\cos(\theta_C) = \frac{c_{vac}}{n_{medium}v}. \quad (2.1)$$

2.2 Neutrino-Nucleon Scattering

Neutrino-nucleon scattering generally involves one of three scenarios: Quasi-elastic scattering (QE), resonance production (RES) or deep-inelastic scattering (DIS). The cross section for each scattering interaction is shown as a function of energy in Figure 2.2a and 2.2b for the neutrino and anti-neutrino respectively, with quasi-elastic scattering indicated by the dashed line, resonance production by the dash-dotted line, and deep inelastic scattering by the dotted line.

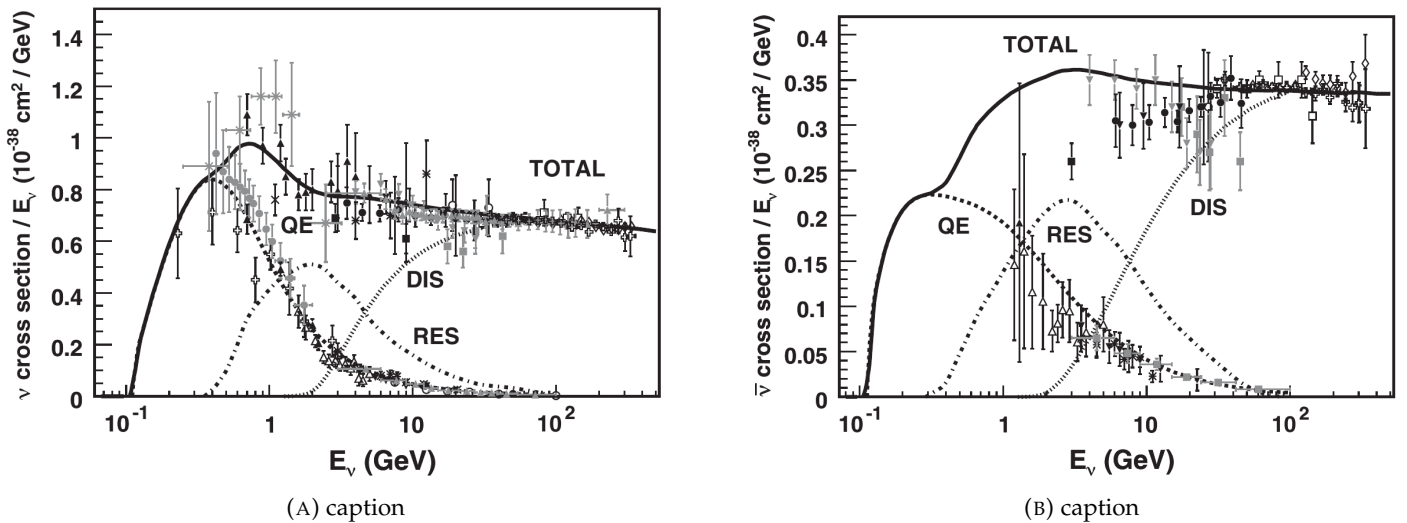


FIGURE 2.2: (a) Neutrino cross section as a function of energy, shown for different nucleon scattering processes. (b) Anti-neutrino cross section as a function of energy, shown for different nucleon scattering processes[13].

2.2.1 Elastic and Quasi-Elastic Scattering

Neutrinos undergoing elastic scattering, scatter off the entire nucleon. Quasi-elastic scattering refers to elastic scattering via CC interactions, while *elastic scattering* refers to the same process but via NC interactions[13]. As indicated by Figure 2.2, QE scattering is dominant at energies below 1 GeV. Examples of QE scattering for a ν_μ and $\bar{\nu}_\mu$ is shown in Equations (2.2) and (2.3) respectively.

$$\nu_\mu + n \rightarrow \mu^- + p \quad (2.2)$$

$$\bar{\nu}_\mu + p \rightarrow \mu^+ + n \quad (2.3)$$

Elastic scattering off nucleons via NC interactions can be generalized for all neutrino flavors, as the outcome of the interaction is identical. Examples of NC elastic scattering interactions are shown in Equations 2.4 and 2.5.

$$\nu_l + n \rightarrow \nu_l + n, \quad \nu_l + p \rightarrow \nu_l + p \quad (2.4)$$

$$\bar{\nu}_l + n \rightarrow \bar{\nu}_l + n, \quad \bar{\nu}_l + p \rightarrow \bar{\nu}_l + p \quad (2.5)$$

where p is a proton and n is a neutron.

2.2.2 Resonance Production

At energies above 1 GeV RES starts becoming dominant. Resonance production (RES) occurs when a neutrino scatters off a nucleon and induces an excited state, in turn producing a baryonic resonance (Δ , N^*). The baryonic resonant decays to a variety of possible mesonic final states, most commonly a nucleon and single pion

$$\nu_\mu N \rightarrow \mu^- N^* \quad N^* \rightarrow \pi N' \quad (2.6)$$

where N / N' is a proton or neutron. Figure 2.3 shows the Feynman diagram of RES via a CC interaction for which a proton is excited to resonant state producing a Δ^{++} that decays to a π^+ and a proton.

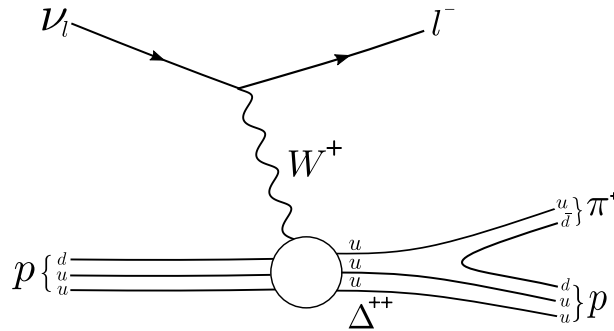


FIGURE 2.3: Resonant production from a neutrino-nucleon charged current interaction. The induced resonance creates a Δ^{++} that decays to a π^+ and a proton.

RES starts at neutrino energies slightly higher than QE scattering (0.2-0.3 GeV), and becomes the dominant interaction at around 2 GeV, but quickly drops off at higher energies where DIS is dominant. RES in neutrino scattering off a free nucleon includes seven possible resonant single pion channels (including seven from anti-neutrinos) and are shown in Equations (2.7-2.13). Three of them are from CC interactions,

$$\nu_\mu + p \rightarrow \mu^- + p + \pi^+, \quad \bar{\nu}_\mu + p \rightarrow \mu^+ + p + \pi^-, \quad (2.7)$$

$$\nu_\mu + n \rightarrow \mu^- + p + \pi^0, \quad \bar{\nu}_\mu + p \rightarrow \mu^+ + n + \pi^0, \quad (2.8)$$

$$\nu_\mu + n \rightarrow \mu^+ + n + \pi^-, \quad \bar{\nu}_\mu + p \rightarrow \mu^+ + n + \pi^-, \quad (2.9)$$

with the remaining four being from neutral current interactions,

$$\nu_\mu + p \rightarrow \nu_\mu + p + \pi^0, \quad \bar{\nu}_\mu + p \rightarrow \bar{\nu}_\mu + p + \pi^0 \quad (2.10)$$

$$\nu_\mu + n \rightarrow \nu_\mu + n + \pi^0, \quad \bar{\nu}_\mu + n \rightarrow \bar{\nu}_\mu + n + \pi^0 \quad (2.11)$$

$$\nu_\mu + p \rightarrow \nu_\mu + n + \pi^+, \quad \bar{\nu}_\mu + p \rightarrow \bar{\nu}_\mu + n + \pi^+ \quad (2.12)$$

$$\nu_\mu + n \rightarrow \nu_\mu + p + \pi^-, \quad \bar{\nu}_\mu + n \rightarrow \bar{\nu}_\mu + p + \pi^- \quad (2.13)$$

2.2.3 Deep Inelastic Scattering

Deep Inelastic Scattering (DIS) occurs at neutrino energies above ~ 1 GeV, and becomes the dominant neutrino-nucleon interaction above ~ 10 GeV. When a neutrino undergoes DIS, it scatters off a quark in the nucleon producing a shower of hadronic particles in the process[13].

DIS interactions occurs in both CC and NC interactions, with the difference being the lepton produced in (CC) and the neutrino left intact in (NC) carrying away some of the energy. Feynman diagrams of CC and NC DIS interactions are shown in Figures 2.4a and 2.4b respectively.

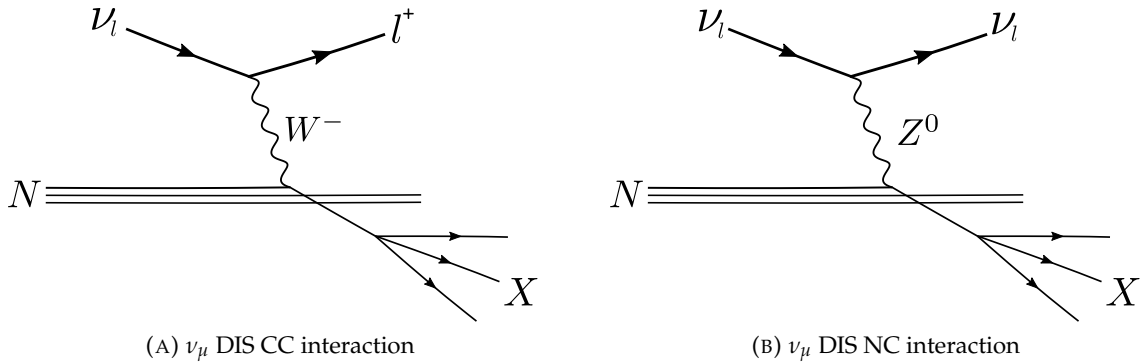


FIGURE 2.4: Feynman diagrams showing (a) DIS CC interaction with a neutrino and quark and (b) DIS NC with a neutrino and quark.

2.3 Electromagnetic and Hadronic Showers

In neutrino-nucleon interactions producing particle showers, there is generally distinguished between two types of particle showers: Electromagnetic showers and hadronic showers. Electromagnetic showers are produced in ν_e CC interactions by the outgoing electron, as well as in τ decays, from bremsstrahlung along the path of a muon, and in pair production interactions [14].

Electromagnetic showers have nearly identical light deposition patterns that are independent on the energy (below PeV scale). The length of the shower increases logarithmically with energy. Electrons produced in CC ν_e interactions quickly begin emitting

photons through bremsstrahlung. The photons produced undergo pair production, resulting in a continuous cycle as a shower of electrons and photons quickly forms.

Hadronic showers are produced in flavor independent NC interactions, in all DIS interactions, in τ decays, and from muon photonuclear interactions. The light signature from hadronic showers is very similar to that of an electromagnetic shower, but with a suppressed light yield due to the production of neutrinos carrying away some of the energy, in addition to a lower amount of free energy being available as a consequence of the heavy rest masses of hadrons. The light yield produced from hadronic showers at around 100 GeV is on average only 74% (with variations of 17%) the amount of light obtained from an electromagnetic shower at same energy [14].

The energy deposition from electromagnetic showers created by CC ν_e interactions is nearly identical to the energy of the ν_e . On the other hand, NC interactions producing hadronic showers leave big uncertainties in the deposited energy from the neutrino staying intact carrying away the remaining energy. The relationship between the energy of the neutrino and the energy from charged particles in the shower is shown in Figure 2.5 for CC interactions to the right and NC interactions to the left.

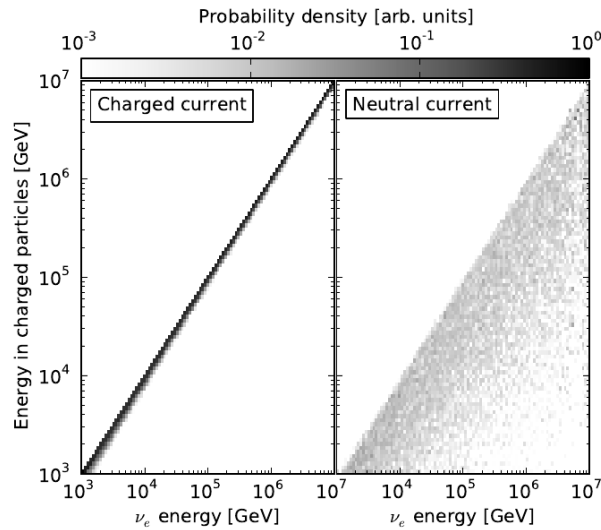


FIGURE 2.5: (left) Energy deposition from the magnetic shower produced by ν_e CC interactions. (right) Energy deposition from the hadronic shower produced by ν_e NC interactions. The big uncertainties in energy stem from energy being carried away by the neutrino(s)[14].

2.4 Track-like Events

Track-like events occur from ν_μ CC interactions and get its characteristic track-like light signature from the muon being produced in the interaction. ν_μ CC interactions are the only type leaving a track-like signature, since the other leptons, ν_e and ν_τ , quickly become particle showers shortly after they are produced. Muons, on the other hand, can travel several hundred meters in the detector.

Low energy muons ($E_\mu \lesssim 1$ TeV) produced from neutrino interactions in the ice of Ice-Cube travel about 5 m per GeV of energy while producing photons through Cherenkov radiation [15]. If the muon is produced with enough energy, it leaves a track-like signature in the detector that extends much further than the size of the cascade. However, at low energies (<10 GeV) it can become very difficult to distinguish cascade and track-like

events, as the track-length of the muon approaches lengths equal to the cascade size. A track-like event and a cascade event is shown in Figures 2.6a and 2.6b respectively.

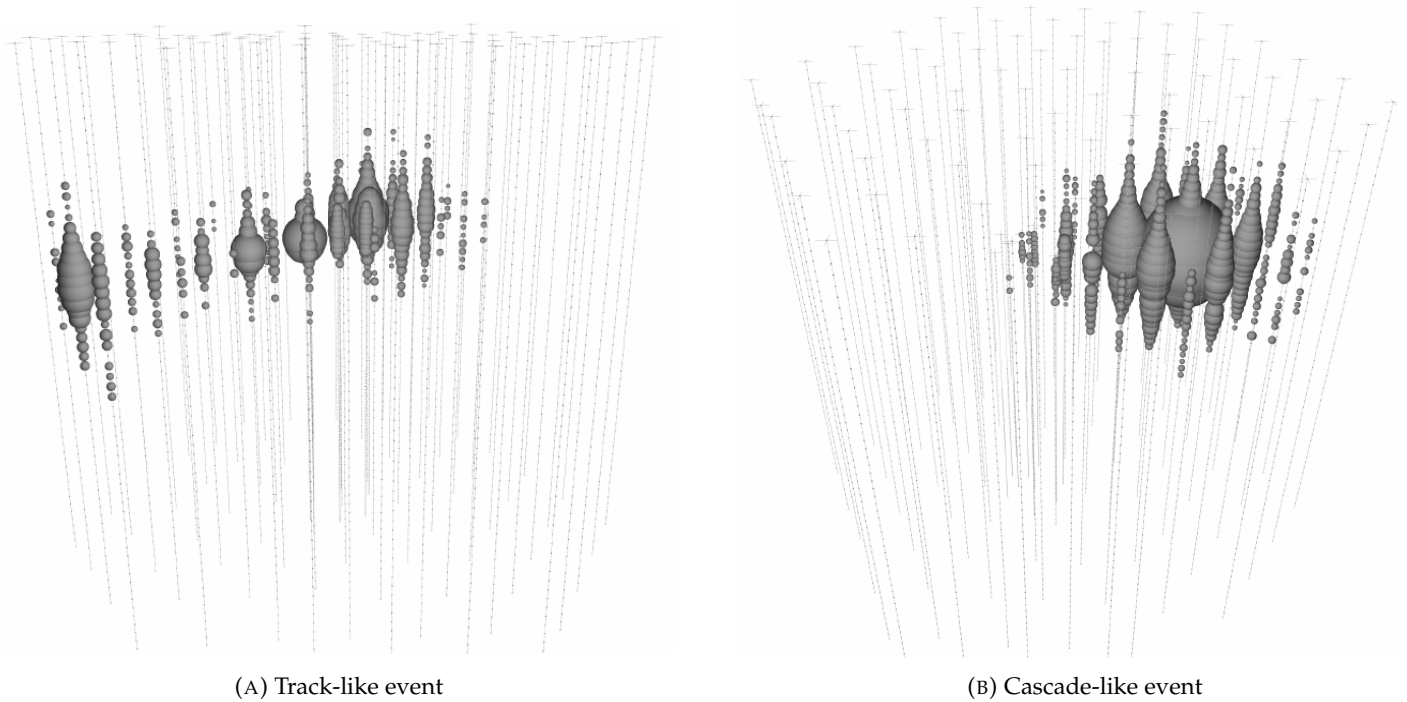


FIGURE 2.6: (a) A track-like event in the detector, from a muon depositing 74 TeV worth of energy with the remaining energy being carried away. (b) A cascade that deposited 1070 TeV in the detector. For cascades fully contained in the detector, the energy can be determined directly.

2.5 Atmospheric Neutrinos

When cosmic rays interact in Earth's atmosphere they produce a shower of particles. Many of the particles from the shower are unstable, and as they decay neutrinos are produced. These neutrinos are referred to as *atmospheric neutrinos*.

Cosmic rays are composed of charged particles or atomic nuclei that have been accelerated towards Earth through different astrophysical phenomena. Cosmic rays can be enormously energetic, reaching energies in the EeV scale (10^{18} eV). The most energetic cosmic ray ever observed (as of 2019) was the *Oh-My-God* particle, with an estimated energy of $(3.2 \pm 0.9) \cdot 10^{20}$ eV, or 50 J. This is energy equivalent to a baseball traveling at 94 km/h, all being contained in a single particle. The full energy spectrum of cosmic rays is shown in Figure 2.7.

Cosmic rays in the GeV/nucleon region are mainly composed of protons, while about 5% are Helium nuclei and an even smaller fraction being heavier nuclei. Cosmic rays also include electrons and photons, but they do not produce neutrinos as they interact in the atmosphere[6].

Cosmic rays that intersect Earth, interact with the nuclei in the upper atmosphere and typically produce a lot of π mesons, with the addition of a few K mesons. Mesons are unstable and decay into other particles. For example π^+ decays to

$$\pi^+ \rightarrow \nu_\mu + \mu^+. \quad (2.14)$$

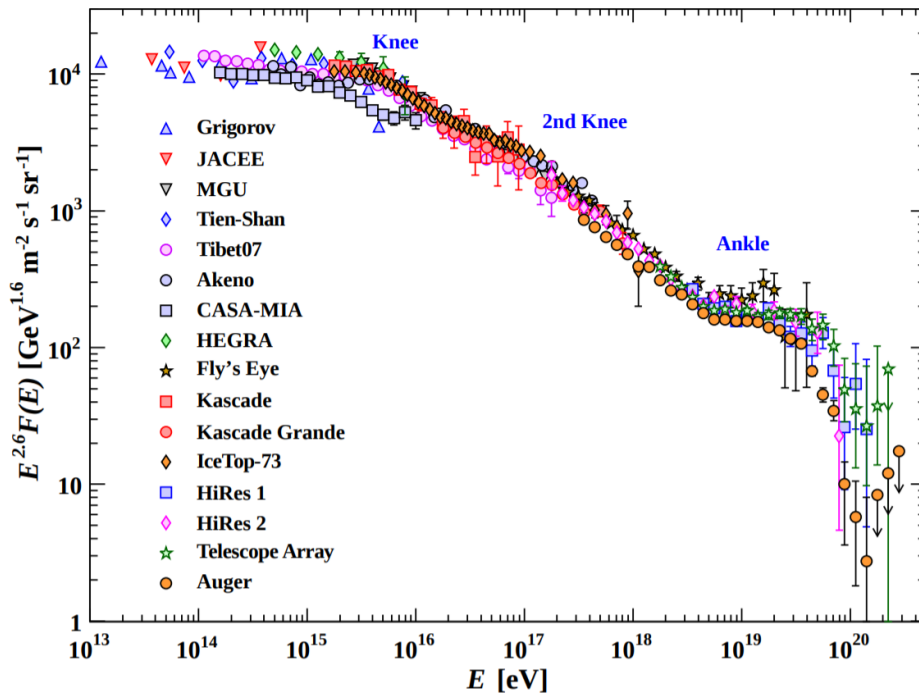


FIGURE 2.7: All-particle cosmic ray flux as a function of energy, measured by various air shower experiments[11].

The μ^+ is unstable and as it decays additional neutrinos are produced

$$\mu^+ \rightarrow \bar{\nu}_\mu + \nu_e + e^+. \quad (2.15)$$

Similar decay processes occur for π^- and K mesons as well. When highly energetic cosmic rays interact in the atmosphere they become a shower of less energetic particles through these decay processes, as illustrated in Figure 2.8.

Earth is constantly bombarded by cosmic rays from all directions. As a result, atmospheric neutrinos are constantly produced, and because of the neutrinos small cross section, they easily pass through the entirety of Earth. Atmospheric neutrinos are a source for neutrino oscillation experiments, as they allow for baselines distances of up to the diameter of Earth (12,700 km).

2.6 Oscillation Analysis

As discussed in section 1.6 oscillation parameters such as θ_{23} can be studied from $\nu_\mu \rightarrow \nu_\mu$ and $\nu_\mu \rightarrow \nu_\tau$. These studies are often referred to as ν_μ disappearance and the ν_τ appearance. ν_μ disappearance refers to the fraction of missing ν_μ events, based on what is expected from the atmospheric neutrino flux. The deficit of ν_μ would be the consequence some having oscillated to ν_τ and ν_e . ν_τ are rarely created in cosmic ray interactions in the atmosphere or other processes on Earth. However, as a consequence of neutrino oscillation, ν_τ are produced in measurable numbers, which is what ν_τ appearance refers to.

The neutrino flux is complex and difficult to calculate precisely, giving rise to uncertainties in the oscillation physics analysis. Using the processes described in Equations

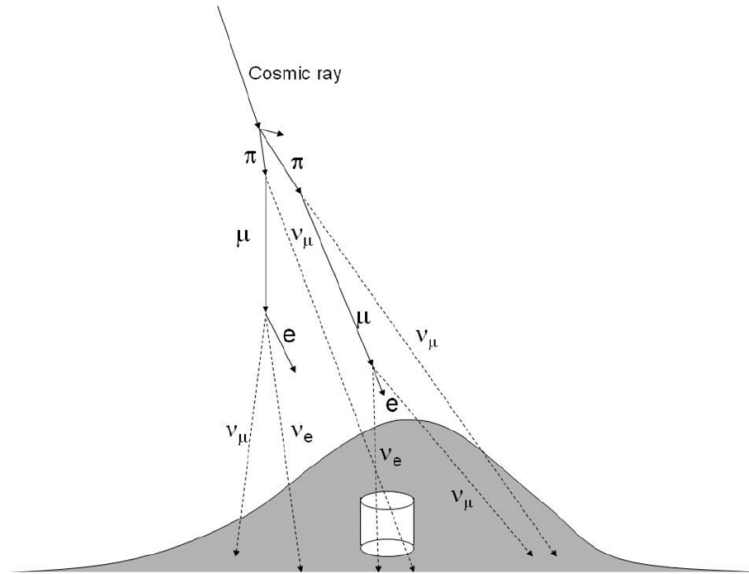


FIGURE 2.8: Highly energetic cosmic rays interact with nuclei in the upper atmosphere, in turn creating a shower of particles through production and decay mechanism. The neutrinos produced in these decays are referred to as atmospheric neutrinos [6].

(2.14) and (2.15), the flux can be estimated fairly well at certain energies. From Equation (2.14) 2 (ν_μ plus $\bar{\nu}_\mu$) and 1 (ν_e or $\bar{\nu}_e$) are produced for every π^\pm decay. This the ratio between $\nu_\mu / \bar{\nu}_\mu$ and $\nu_e / \bar{\nu}_e$ becomes approximately 2, assuming the neutrinos mainly comes from charged pions. This approximation is not far off the truth if staying below energies of a couple of GeV where muons decay before reaching the surface. Figure 2.9 shows the $(\nu_\mu + \bar{\nu}_\mu)/(\nu_e + \bar{\nu}_e)$ ratio as a function of neutrino energy, calculated by three independent groups [6].

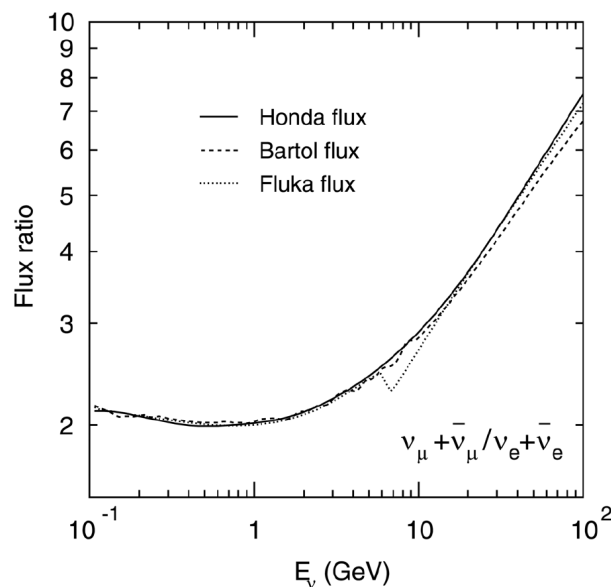


FIGURE 2.9: The atmospheric neutrino flux ratio $(\nu_\mu + \bar{\nu}_\mu)/(\nu_e + \bar{\nu}_e)$, calculated by the three independent groups Honda, Bartol and Fluka [6].

From the atmospheric neutrino flux, the expected number of neutrinos that would

appear in IceCube can be calculated. The distributions of reconstructed energy and $\cos \theta$ (baseline) from observations are compared to simulation based on the flux and the oscillation parameters. The oscillation parameters are estimated by modifying them in the simulated template so they match the observation.

The azimuth angle ϕ and zenith angle θ are commonly used in astrophysics when describing directions in relation to Earth and the sky. Azimuth describes the longitudinal angle around Earth, while zenith describes the latitudinal angle as illustrated in Figure 2.10a.

The neutrino oscillation probability is very dependent on the baseline distance and becomes an important factor in oscillation analysis. When observing atmospheric neutrinos interactions, the angle of the intersecting neutrino can be used to determine baseline distance. Since the path of a neutrino is virtually unaffected by matter, precisely knowing its angle of incidence allows for the baseline to be calculated, as it can be traced through the Earth to the point where it was produced. Figure 2.10b illustrates the relationship between the ingoing and outgoing angles θ . In IceCube atmospheric neutrinos from all directions are observed, which allows for a range of baselines to be included in the analysis.

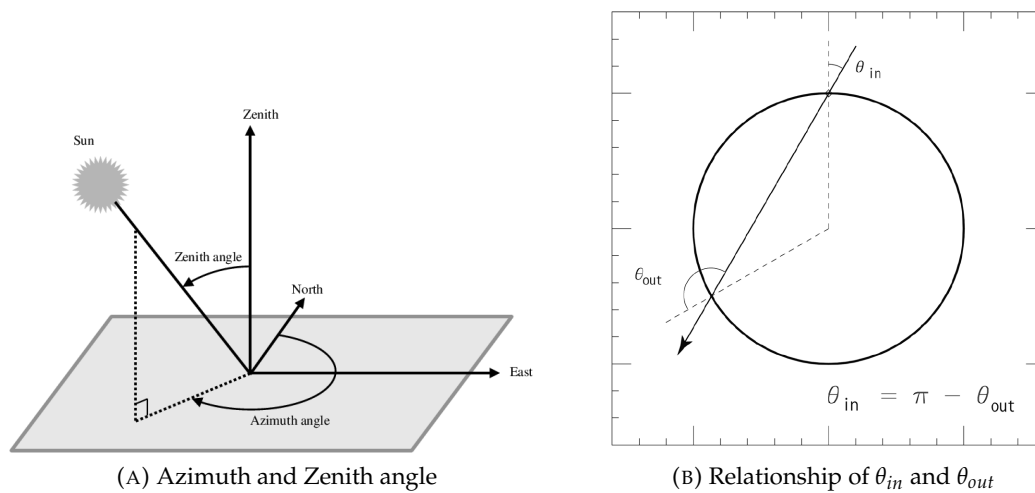


FIGURE 2.10: (A) The azimuth and zenith angle are commonly used in astrophysics when describing directions in relation to Earth[16]. (B) The relationship of θ_{in} and θ_{out} for a neutrino traversing Earth[6].

3 The IceCube Detector

The IceCube Neutrino Observatory holds the largest neutrino detector in the world. It is situated at the geographical South Pole and was built for studying very high energy neutrinos originating from some of the most energetic events in our universe, e.g. exploding stars, gamma-ray bursts, blazars, and cataclysmic events involving black holes and neutron stars [17].

The detector consists of a huge array of highly sensitive light sensors, that have been deployed in the very clear glacial ice beneath the surface of the South Pole, spanning roughly 1 km^3 in total. Information about any neutrinos is gathered from the Cherenkov light induced by charged particles created from neutrino collisions within the ice.

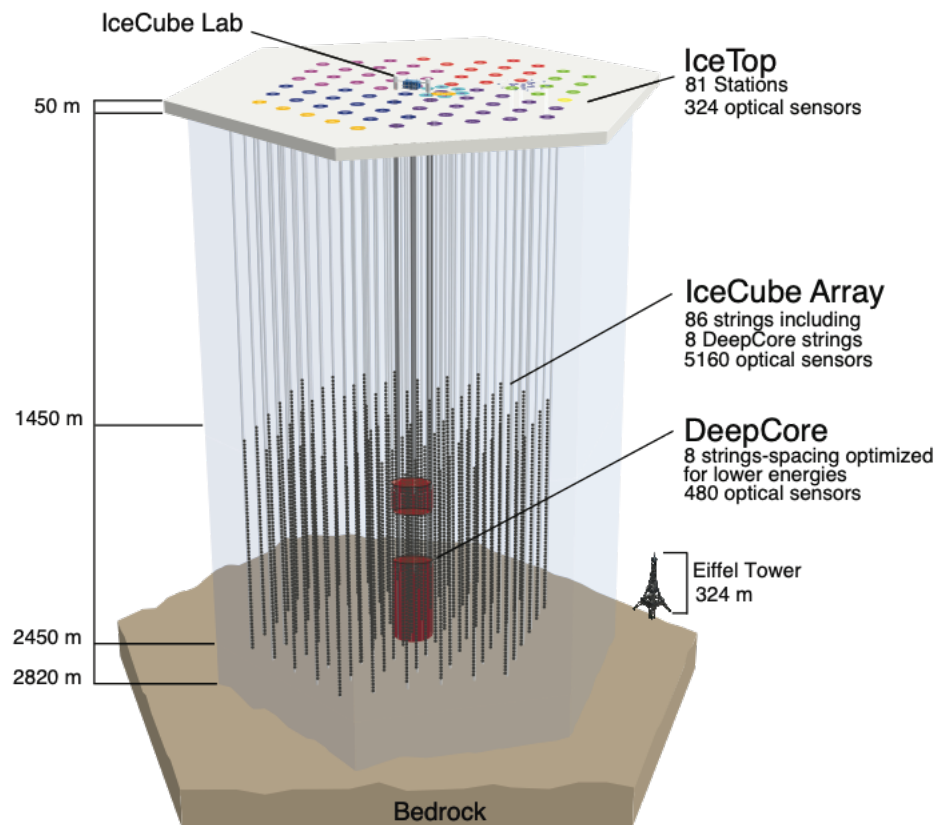


FIGURE 3.1: Schematic of the full IceCube detector, including the cosmic ray air shower array IceTop at the surface, and the in-ice sub-array DeepCore marked in red.

The detector is equipped with a cosmic ray air shower array *IceTop*, that is located at the surface. IceTop consists of 81 stations with a total of 162 ice-filled tanks instrumented by light sensors similar to those in the in-ice array. IceTop is sensitive to very high energy cosmic rays at energies of PeV to EeV, with an energy resolution of 25% at 2 PeV improving to 12% above 10 PeV. It also serves as a partial veto for downwards-going neutrinos

observed in IceCube. However, as IceTop is not an integral part of the instrumentation used for oscillation physics, and will not be referenced any further in this thesis.

The in-ice detector contains a sub-array *DeepCore*, that has been optimized for the detection of low energy neutrinos. In DeepCore the instrumentation is more densely packed than in the rest of the detector and the majority of the instrumentation is situated in the deepest region of the ice (DeepCore is described with more detail in Section 3.3). A schematic of the full detector is shown in Figure 3.1.

The detector was deployed using a hot-water drill, lowering multiple long cables (strings) into the depths of the glacial ice, each equipped with 60 Digital Optical Modules (DOMs). The DOMs are situated at depths between 1500 m and 2500 m, where the ice is very clear and the surroundings dark. The full in-ice detector consists of 86 strings (eight of them DeepCore strings), arranged in a hexagonal shape. Non-DeepCore strings are horizontally spaced by 125 m with a vertical DOM-to-DOM spacing of 17 m.

The eight DeepCore strings are accompanied by instrumentation from the bottom-third of seven IceCube strings. The average horizontal distance between 13 of the 15 DeepCore strings is 72 m which corresponds to about 1.5 times the average scattering length in that part of the ice[15]. Six of the strings have an average horizontal distance of only 42 m, roughly three times smaller than the 125 m for standard IceCube strings. The vertical DOM spacing is 7 m, making DeepCore strings twice as dense as standard IceCube strings, in the regions that are instrumented.

One terabyte of unfiltered data is collected by IceCube daily. The IceCube Lab (ICL), at the surface of the South Pole, houses the computers handling the initial data processing as well as the data transmission. Before transmission, the unfiltered data is run through the online Processing and Filtering (PnF) system that handles all the triggered events. The treatment includes the application of calibration constants, event characterization and selection, extraction of data quality monitoring information, and the generation of real-time alerts for events of astrophysical interest. The treatment also includes the creation of data files and meta information for long-term archiving. The data volume is reduced to a level that can be accommodated by the satellite bandwidth, resulting in about 100 GB of data being sent daily[17].

3.1 Digital Optical Module

A Digital Optical Module (DOM) is the fundamental data acquisition unit in IceCube. The DOM consists of a spherical glass housing equipped with a downward-facing 10'' photomultiplier tube (PMT) with a circuit board (mainboard) sitting on top. All communication, control, calibration, low-voltage power conversion, and data acquisition is integrated on the mainboard, the cable provides power and transmits the digital signal to the ICL. A schematic of an IceCube DOM with a photograph as comparison is shown in Figure 3.2.

3.1.1 Glass housing, gel and magnetic shielding

The housing is made of a glass pressure sphere with an outer diameter of 13'' and a thickness of 0.5'', and protects the electronics and PMT from the immense pressures caused by the surrounding ice. It has been designed to handle long-term applied pressure of 250 bar (equivalent to 2.6 km water depth), as well the temporary pressure of 690 bar that can occur during the refreezing phase post deployment[17].

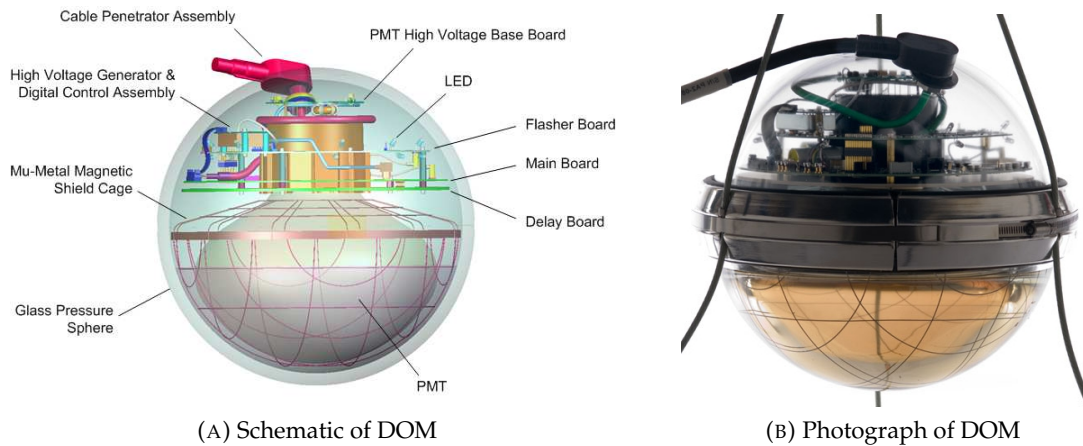


FIGURE 3.2: (Left) A schematic of a Digital Optical Module (DOM) [18]. (Right) A photograph of an assembled DOM [19]. The DOMs are connected to a cable supplying the power and enabling communication with IceCube Laboratory at the surface.

The pressure sphere was made using borosilicate glass with low amounts of radioactive trace elements, in order to reduce the dark noise contribution (dark noise is described in section 3.1.4). The PMTs used in standard IceCube DOMs are the 10" Hamamatsu R7081-02, specified by Hamamatsu for wavelengths in the 300-650 nm range, with peak quantum efficiency at around 25% for wavelengths of 390 nm.

The downwards-facing PMT is secured in high-strength silicone gel, providing a good optical coupling, as well as being a mechanical support for the PMT. The gel thickness between the PMT and glass sphere is approximately 1 cm. The gel is optically very clear with a transmission of 97% for wavelengths of 400 nm to 65% for wavelengths of 300 nm.

The PMT is surrounded by a mu-metal magnetic shielding cage that helps reduce the effects from the ambient South Pole magnetic field. Without such shielding, the PMT would exhibit a 5-10% lower collection efficiency, poorer single photoelectronic resolution, as well as 20% gain variation, depending on azimuthal orientation[17].

3.1.2 Photomultiplier Tubes

Photomultiplier tubes (PMTs) are photon detectors that function in the ultraviolet to near-infrared ranges of light. They serve as a tool for converting photons to an electrical signal that can be read by a computer. The PMT amplifies the weak signal from a single photon using electron multipliers, increasing the signal strength by up to factors of 10^7 [17].

On the face of the PMT sits a photocathode that when hit by a photon emits an electron, as a consequence of the photoelectric effect [20]. After emission, a focusing electrode applying an electric field guides the electron towards the electron multiplier, which consists of a set of electrodes (dynodes). When the first dynode is struck by the electron a number of electrons are emitted from the dynode through the process of secondary emission. The newly emitted electrons are driven towards the next dynode releasing additional electrons when hit, creating a bigger and bigger cascade of electrons for every dynode stage. The number of electrons increases exponentially for each stage, yielding a measurable electrical signal by the end, corresponding to a photon having hit the PMT. A schematic of a PMT is shown in Figure 3.3.

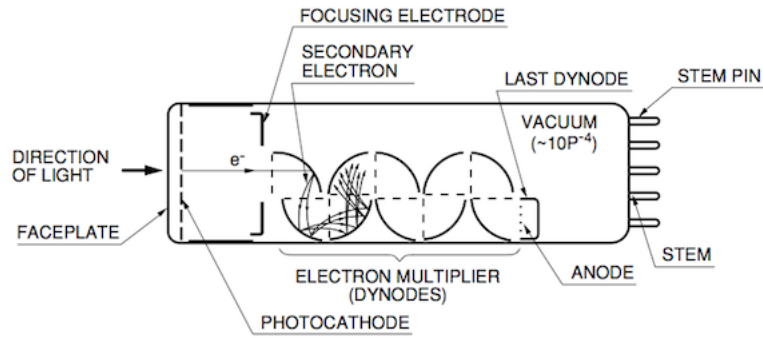


FIGURE 3.3: Schematic of a photomultiplier tube. The incoming photon hits a photocathode emitting an electron as a consequence of the photoelectric effect. The electron is then guided towards a series of dynodes that initiates a cascade of electrons, amplifying the original signal. The illustration is taken from [21].

The PMT used in standard IceCube DOMs has 10 linear dynode stages and achieves a nominal gain of 10^7 . A single photon pulse yields a signal strength of about 8 mV, which is well above the digitizer precision and electronic noise, both of which are around ~ 0.1 mV [22].

3.1.3 Local Coincidence

The cable holding the DOMs is not only connected the ICL, but includes specific wiring to its two neighboring DOMs. One wire pair which carries the power and bidirectional communication is ultimately connected to the computers at the ICL and additionally each DOM has two wire pairs connecting it to the DOM directly above and below (this illustrated in Figure 3.4 (Right)). These DOM-to-DOM wire pairs are dedicated for observing local coincidences (LC) between neighboring DOMs and allow for quick recognition of coincidence hits within a common time window (set to $\pm 1 \mu\text{s}$) [17].

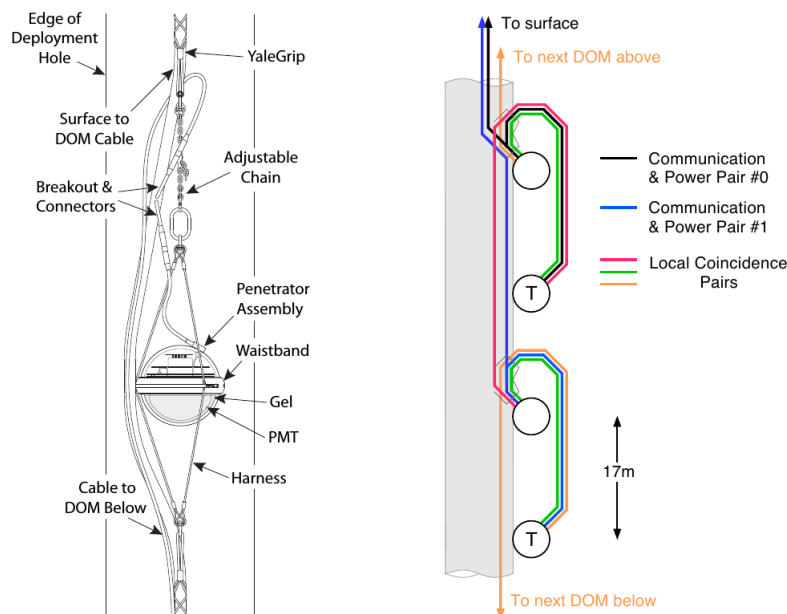


FIGURE 3.4: (Left) Illustration of a DOM being deployed. (Right) Schematic of the connections between a set of four DOMs. The DOM-to-DOM wiring allow for recognition of local coincidence (LC) hits [17].

The majority of background hits on in-ice DOMs are caused by dark noise. The first step in the data cleaning process uses LC to identify DOMs that should have their digital signal transmitted to the ICL. If hits meet the LC criteria they are flagged as Hard Local Coincidence hits (HLC) and the full digitized waveforms are included. Isolated non-LC hits are flagged as Soft Local Coincidence hits (SLC) and are compressed more aggressively, only saving timestamp and minimal amplitude / charge information.

3.1.4 Dark Noise

Dark noise is the hits that were not caused by incident photons from charged particles in the ice, and provides a significant contribution to the background hits in the in-ice detector [17]. Dark noise stems from multiple effects leading to the emission of an electron from the PMTs cathode in the absence of an external photon source and is caused by thermionic emission, field emission within the PMT, Cherenkov light from radioactive decays and scintillation / luminescence in the glass of the PMT and pressure sphere.

Dark noise in IceCube can be characterized by a combination of uncorrelated noise pulses with a rate between 230-250 Hz and a correlated component with a rate between 280-340 Hz (The average in-ice hit rate for a standard IceCube DOM is 560 Hz[17]). Experiments using a bare PMT at low temperatures suggest that the main contributor of noise originates from the glass pressure sphere.

Detector noise becomes an increasingly big problem at low energies (<10 GeV). Events at these energies only leave a few dozen hits in the detector, from which noise becomes a big contribution. Cleaning algorithms are commonly used to process hits from an event before it is reconstructed. This step is important, since the addition of noise hits contribute to uncertainties in the reconstruction, as the noise hits add inaccurate information about the signature of the event. However, not all noise hits can be removed since they can be hard to distinguish from signal.

3.2 Ice Properties

The glacial ice making up IceCube is very clear, but not entirely homogeneous. Mineral dust correlated with climatological history results in changing scattering and absorption properties at varying depths in the ice [15].

The dust concentration is highest in a band from 2000 m to 2100 m depth, and is referred to as the *dust layer*. The placement of DeepCore modules was motivated by these observations, leading to the majority of the optical modules being placed beneath the dust layer. Ice at depths below 2100 m is estimated to be 40%-50% clearer, on average, than the ice between 1500 m and 2000 m. The ice is clearest at around 2400 m depth, with an average scattering length close to 50 m and absorption length close to 190 m. These values are based on light with wavelengths around 400 nm, which is a wavelength close to the peak of the DOM sensitivity, as well as being the most transparent in ice.

Most of the photon propagation happens in the glacial ice not affected by the drill holes from string deployment, and this part of the ice is referred to as *bulk ice*. The structure and optical properties of the bulk ice has been measured using *dust-loggers*[23] that were lowered into the ice via the drill holes. A horizontal laser beam on the dust-logger was used to illuminate the bulk ice, from which a small fraction of light was redirected

back into the drill hole where it was measured by a downwards-facing PMT. In addition, measurements using flashing LEDs situated on the DOMs have been used to derive models of the bulk ice [24].

3.2.1 Hole Ice

When a string has been deployed using a hot-water drill, the water surrounding the string is allowed to refreeze, and the column of refrozen ice is named *hole ice*. The refreezing process has been studied using a dedicated camera at the bottom of string 80, and it was observed that the drill hole was completely refrozen after 15 days[24][17]. The optical properties of the hole ice are currently less understood than those of the bulk ice, causing big uncertainties in neutrino oscillation measurements.

It was observed that hole ice consists of three distinct regions (illustrated in Figure 3.5). The outermost region consists of bulk ice. The outer region of the drill holes consists of the refrozen ice, and contains equal or better optical properties compared to the bulk ice. The central region of the hole ice (marked by the blue circle in Figure 3.5), shows significantly worse optical properties in comparison to the bulk ice. The observations from this region are consistent with cylindrical freezing, where impurities and bubbles in the ice are pushed along the freezing boundaries towards the center where they merge. This central region of the hole ice is referred to as the *bubble column*.

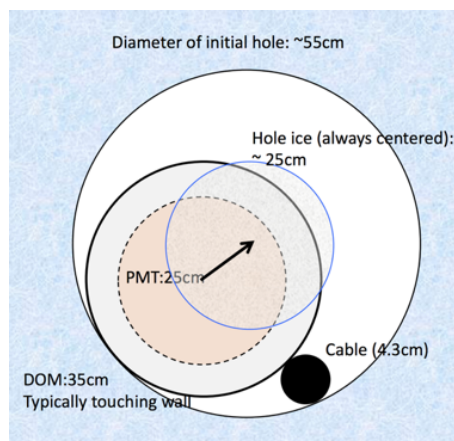


FIGURE 3.5: Illustration of different regions in the hole ice, caused by the refreezing of water post deployment. The blue shaded region show the bulk ice (unaffected glacial ice). The central region, indicated by the blue circle, marks the ice where significantly worse optical properties has been observed.

In simulation, the optical properties of the hole ice are treated using a *hole-ice parameterization*. The bubble column is modeled by a column of ice approximately 30 cm in radius surrounding the IceCube string. The hole-ice parameterization accounts for the increased scattering by modifying the effective angular sensitivity curve of the DOMs[25].

3.3 DeepCore

DeepCore is a sub-array within IceCube that is optimized for low energy neutrinos (~ 10 GeV). DeepCore consists of eight specialized strings equipped with high quantum efficiency PMTs (HQE DOMs), improving the quantum efficiency by 35% in comparison to standard modules. The horizontal spacing between strings and the vertical spacing between DOMs is much smaller in DeepCore than in rest of the detector. This enables low energy

events to produce hits on multiple DOMs and strings, otherwise not be possible due to the low number of photons produced in such events.

Each DeepCore string holds a total of 60 DOMs, with 50 out of 60 placed beneath the dust layer in depths between 2100 m and 2450 m. This is the deepest region in the detector, where the ice is clearest and has the best optical properties. This arrangement is separate from standard IceCube strings where all 60 DOMs sit equally spaced in depths between 1450 m and 2450 m, as illustrated in Figure 3.6.

The 10 remaining DOMs are situated above the dust layer, between 1750 m and 1860 m, and are being used as an added veto for atmospheric muons from directly above. In Figure 3.6, the green region shows the DOMs beneath the dust layer, while the red region shows the ones above. The dust concentration is shown to the left as a function of depth, clearly indicating the dust layer.

Even though the IceCube Neutrino Observatory was originally built for observing very high energy neutrinos ($E > 1$ TeV), the addition of DeepCore has opened a new window for physics analyses based on low energy neutrinos. These analyses include the search for weakly interacting massive particles (WIMPs) and the study of neutrino oscillation parameters. DeepCore lowers the neutrino detection energy threshold by more than an order of magnitude, giving a lower bound at around 10 GeV.

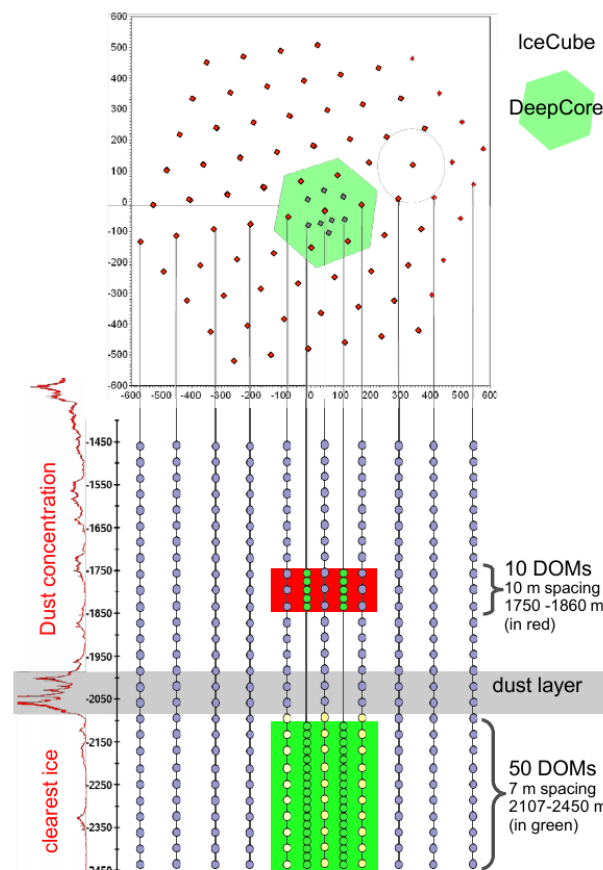


FIGURE 3.6: Illustration of the placement of DeepCore modules in IceCube. The green region indicates the modules placed beneath the dust layer, in the clearest section of ice. The red region indicates the modules placed above the dust layer, acting as an added veto for atmospheric muons. The concentration of dust is shown on a graph to the left [26].

In addition to the improved sensitivity in energy, DeepCore allows for a good ability to veto background events from atmospheric cosmic ray muons, by using the surrounding IceCube detector as an active veto to identify the background muons. This veto is very effective since downwards-going muons are very likely to hit an IceCube DOM before reaching DeepCore. This is essential since muons have a trigger rate in the detector approximately 10^6 times higher than that of atmospheric neutrinos[15]. Figure 3.7 shows the event rates of atmospheric muons (pink line) as a function of different levels in the event selection. The figure shows the efficiency of the muon veto, reducing the atmospheric muon rates by many orders of magnitude [27].

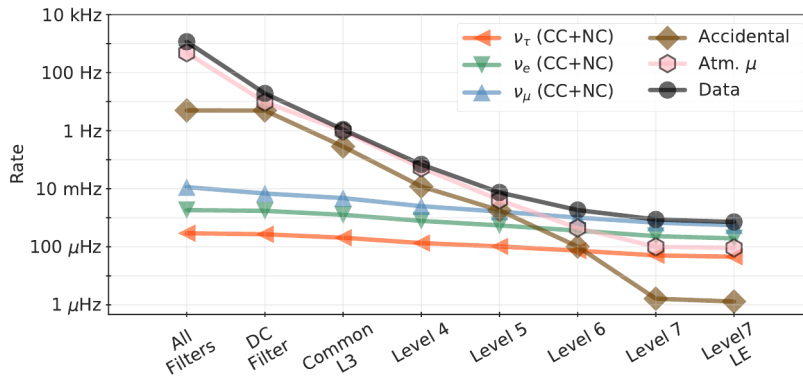


FIGURE 3.7: The event rates in DeepCore as a function the event selection level. Because of DeepCore’s good ability to veto background muons, the rate of atmospheric muons (pink line) in the event sample can be reduced by many orders of magnitude[27].

3.4 IceCube Upgrade

The IceCube Upgrade (ICU) is an extension to the IceCube detector which is not yet deployed. The extension involves the addition of seven new strings, adding more than 700 DOMs to the detector, as well as introducing two new module types, the D-Egg and mDOM. On June 25, 2019, the National Science Foundation (NSF) approved the funding of 23M USD (total cost being 34M USD) for the extension and it is scheduled to be deployed during 2022-2023 [28].

The seven new strings will be placed within the volume of DeepCore and the proposed string positions can be seen in Figure 3.8. The horizontal spacing between strings will be in the order of 20 m, and the vertical spacing between DOMs is reduced to 2.4 m, being almost three times as dense as DeepCore strings. In addition, the new optical modules will be two to three times more sensitive than those currently used in the detector [29].

The majority of DOMs are placed at depths similar to that of DeepCore, which is the region with the best optical properties. The ICU will lower the neutrino detection energy threshold to just a few GeV, as well as greatly improving the event reconstruction. The extension is predicted to yield great improvements for IceCube neutrino oscillation analysis, which is very reliant on the performance of low energy neutrino reconstruction methods. The ICU strings will be equipped with new calibration devices, in addition to the new and more sensitive DOMs.

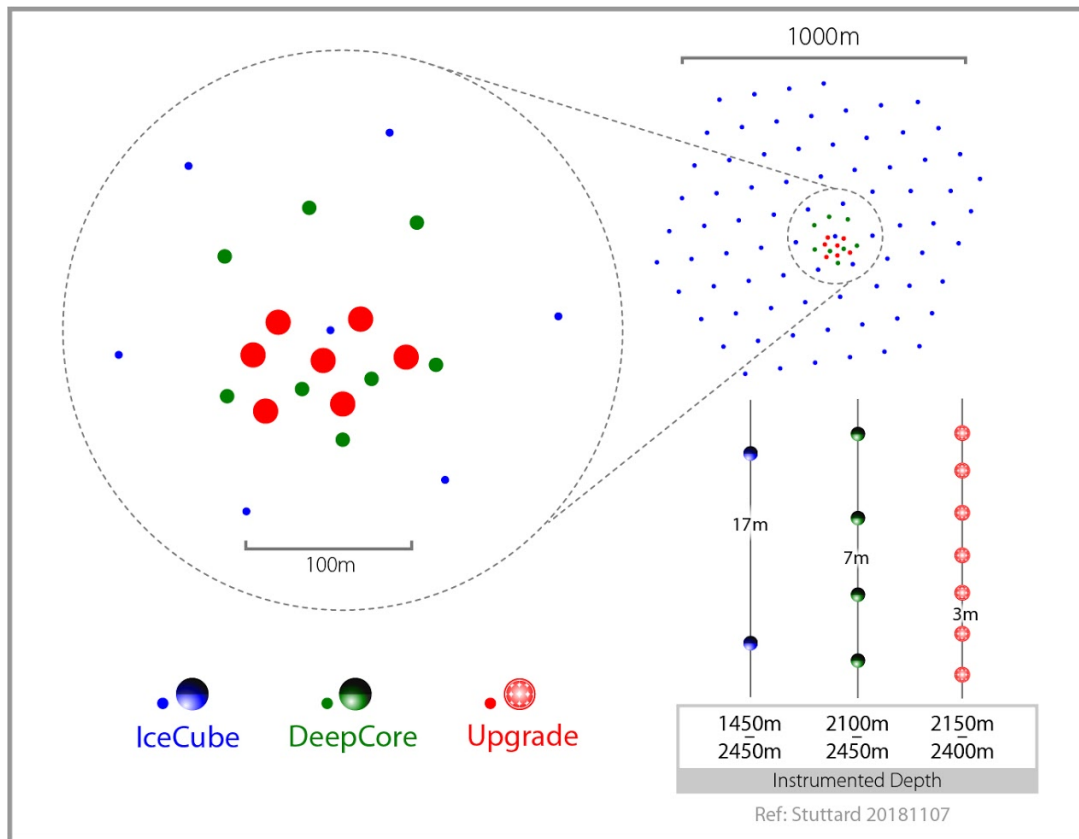


FIGURE 3.8: Proposed placement of the seven new strings that are schedule to be deployed in 2022-2023 as part of the IceCube Upgrade. The strings are placed within the volume of DeepCore and have denser instrumentation. It also introduces two new module types, the D-Egg and mDOM. Illustration courtesy of the IceCube Collaboration.

3.4.1 The D-Egg and mDOM

Standard IceCube DOMs are equipped with just a single downwards-facing PMT, which has the limitation of only being able to detect light coming from below. The two new modules being added with the IceCube Upgrade extension have been designed to avoid this limitation, in addition to other improvements.

The D-Egg consists of two 8" Hamamatsu R5912-100 HQE PMTs, with one facing directly upwards, and the other downwards (the D-Egg is shown in Figure 3.9a). The D-Eggs PMTs are enclosed in an elongated UV-transparent pressure-resistant housing with a diameter of 305 mm. While the PMTs themselves are slightly smaller than the 10" found in standard IceCube DOMs, the total detection area almost doubles, and the addition of an upwards-facing PMT will improve the directional sensitivity of the ICU[D-Egg].

The mDOM is equipped with a total of 24 nearly isotropically oriented 3" PMTs, housed in a 14" borosilicate glass pressure vessel [30]. The shape of the vessel deviates slightly from a sphere, as the design is driven by the limited diameter of the borehole and the size of the PMTs. Curing two-component silicone gel is poured between the PMTs and the pressure vessel, providing an optical coupling in addition to structural stability. Around the entrance of the PMTs are mounted light concentrators, increasing the effective area of the PMT.

The design of the mDOM (Figure 3.9b) comes with several advantages compared to the current IceCube DOMs. The area of 24 3" PMTs results in more than a doubling in

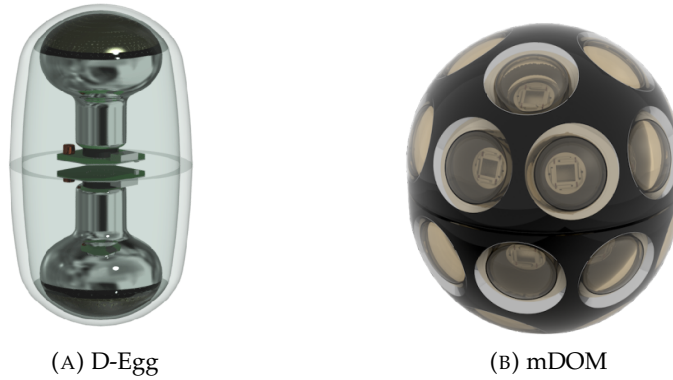


FIGURE 3.9: (a) The D-Egg is equipped with two 8'' PMTs, one facing directly upwards and the other downwards. (b) The mDOM is equipped with 24 3'' PMTs each with different orientations. The mDOM and D-Egg will be part of the IceCube Upgrade extension being deployed in 2022-2023.

combined detection area for the mDOM, compared to the standard DOMs. One of the advantages of multiple PMT orientations is the improved angular sensitivity. mDOMs hit by multiple photons in separate PMTs provide information about the timing and direction of the photons, which is very useful in event reconstruction.

One of the problems currently faced in the ICU is the limitations of the current reconstruction methods. In IceCube, the final reconstruction is based on tables containing parameterizations of light yield for different configurations in the detector, used for finding the hypothesis that best matches the observation.

The tables are about 1 GB in size, all of which must be kept in memory for efficiency. This becomes a significant problem when they are used in distributed computing, where several 100s or 1000s of computers run in parallel, each of which requires the needed memory. In addition, the tables are already limited by approximations in order to reduce their dimensionality. Providing the additional information from the multiple PMT orientations in the new modules might prove infeasible as the dimensionality of the tables will grow, which is problematic as they are already limited by size. Direct reconstruction, is a new reconstruction method that is based on direct simulation. Instead of using pre-constructed tables, direct reconstruction directly computes the expected light yield used when finding the best matching hypothesis in reconstruction. By using direct simulation, the full information from multi-oriented PMTs can be exploited.

In this thesis, the direct reconstruction algorithm is investigated using simulated data in DeepCore and the ICU. Its performance will be tested and compared to that of table reconstruction.

4 Simulation

Simulation is used in many fields of physics as a way to test our understanding of what we observe. Simulation has proved especially useful in particle physics, which involves many interactions where the outcome is based on probabilities. Monte Carlo (MC) simulation refers to algorithms where a chain of probabilistic events are numerically evaluated using a random number generator (RNG), in order to simulate one of many possible scenarios.

When a particle is observed in a detector, the information available for analysis depends on the instrumentation. In experiments where light is the source of information (e.g. Cherenkov detectors), photomultiplier tubes (PMTs) can be used to detect photons from particle interactions by converting them to an electrical signal (PMTs are described in Section 3.1.2).

Simulation is widely used by IceCube in making predictions, testing theories, and as an essential component in the reconstruction process. It is crucial that the simulation precisely reflects the complex nature of neutrinos and other particles involved in interactions in the detector, as it provides an understanding of the data being observed.

Oscillation analysis in DeepCore and the ICU is based entirely on atmospheric neutrinos. The simulation is divided into separate stages involving the full chain of events of going from cosmic rays producing showers in the atmosphere to simulating the photons produced in neutrino interactions in the ice of IceCube. This section provides an overview of the separate simulation stages used for generating DeepCore data samples, creating atmospheric muons for event-selection, and its use in reconstruction.

4.1 CORSIKA

In the first stage of the simulation chain, background muons from cosmic ray interactions in the atmosphere are simulated using the *CORSIKA* generator from Karlsruhe Institute of technology [31]. *CORSIKA* (COsmic Ray SIMulation for KAscade), is a generator that provides detailed simulations of the extensive air showers initiated by cosmic rays in our atmosphere. In *CORSIKA* a range of particles, such as protons, light nuclei up to iron, and photons can be used as the primary particle of the cosmic ray. The density variations of the atmosphere at different altitudes are modeled by five atmospheric layers, with the seasonal differences in density taken into account.

The primary particle starts at the upper border of the atmospheric model, where they are tracked through the atmosphere until they interact with a nucleus in the air. The height of the interaction and the targeted nucleus is selected at random but can be defined explicitly by the user as well. Secondary particles created in the interactions are propagated towards the surface, and effects from energy losses, scattering, and deflection in Earth's magnetic field are taken into account. Particles created in decay processes and interactions from secondary particles are propagated as well, in turn forming the air shower.

Many of the particles produced in cosmic ray interactions decay before reaching the surface or are stopped by the shielding from the Antarctica glacier before reaching the in-ice detector. Still, the trigger rate of background events in the IceCube detector is 10^6

times higher than for neutrinos. In order to produce muons with enough energy to reach the in-ice detector, cosmic rays must have energies of approximately 600 GeV. As IceCube is mostly interested in the muons reaching the in-ice detector, CORSIKA is only used to simulate cosmic rays above the 600 GeV cutoff.

The CORSIKA code has been adapted by the IceCube collaboration to identify the muon and neutrino components of the air shower. IceCube uses CORSIKA by selecting the muons propagated to the surface that have a geometric angle, resulting in them traveling through the in-ice detector. The selected muons are then further simulated in the ice of IceCube using separate software where energy losses from ionization and stochastic effects in the ice are taken into account.

CORSIKA could be used in the same way for simulating neutrinos, but in practice, it becomes extremely inefficient because of the low cross section of neutrinos compared to muons. It would only be relevant in analyses looking at muons and neutrinos coming from the same shower.

4.2 *MuonGun*

CORSIKA is very computationally expensive to use and does not allow for a lot of ways to directly control the spectrum of events. For analyses where the targeted muon simulation falls within a smaller phase space (being it energy, angle or position in the detector), it is useful to have a separate simulation tailored for a specific analysis[26].

For this IceCube has developed a tool that bypasses the full simulation in CORSIKA. The tool is named *MuonGun* and has the benefit of removing the computationally expensive simulation of the full shower, in addition to giving more control for the user, at the cost of losing information about the initial shower. However, it allows for a flexible and efficient way to produce high statistics samples of background atmospheric muon events that are needed in analyses and event selections.

Because the abstraction of *MuonGun* disassociates itself from the cosmic ray and the air shower produced, an effective parameterization is used to weight the muon, accounting for the cosmic ray spectrum dependence. The parameterization is constructed through a separate simulation using the full shower from CORSIKA and a substantial number of samples, creating a clean parameterization in energy and zenith angle of the muons. Even though simulating the full shower is computationally expensive, this only has to be done once.

4.3 Simulating Neutrino Interactions

For neutrino simulation with energies ranging from about 1 GeV to 1 TeV, IceCube uses the GENIE generator[32]. The GENIE code is widely used within the oscillation community, and includes various information about interactions, and cross sections involved in neutrino physics for energies of a few MeV and upwards.

The events generated by GENIE are produced from a power law energy spectrum with a given spectral index. The events are then forced to interact with electrons or nuclei within some specified volume in the detector. The interaction type is simulated using the cross section for the given neutrino flavor and energy. The cross section model includes neutrino interactions by elastic scattering, quasi-elastic scattering, resonance production, and deep inelastic scattering. Deep inelastic scattering is the dominant neutrino interaction for DeepCore energies (>10 GeV).

The particles produced by the neutrino interactions in GENIE are propagated out of the nucleus. In addition, GENIE includes final state interactions, allowing the hadrons to re-interact before leaving the nucleus. Hadrons produced from GENIE simulation with energies of less than 30 GeV are propagated individually using GEANT4. For hadrons with energies above 30 GeV, the lower variability between events permit the use of a parameterized light output.

GEANT4 is a toolkit developed by CERN[33] used for simulating particle propagation through matter. It offers a comprehensive range of interactions, including electromagnetic, hadronic and optical processes. GEANT4 is used by IceCube to simulate the photon production from particles due to energy losses in the medium. Energy losses from different mechanisms are shown in Figure 4.1 as a function of energy, for a muon propagating in ice.

GEANT4 is also responsible for propagating muon and tau leptons, as well as electrons and photons below 100 MeV. For energies above 30 GeV the variations between events are small enough to permit the use of a parameterized light output for the hadrons.

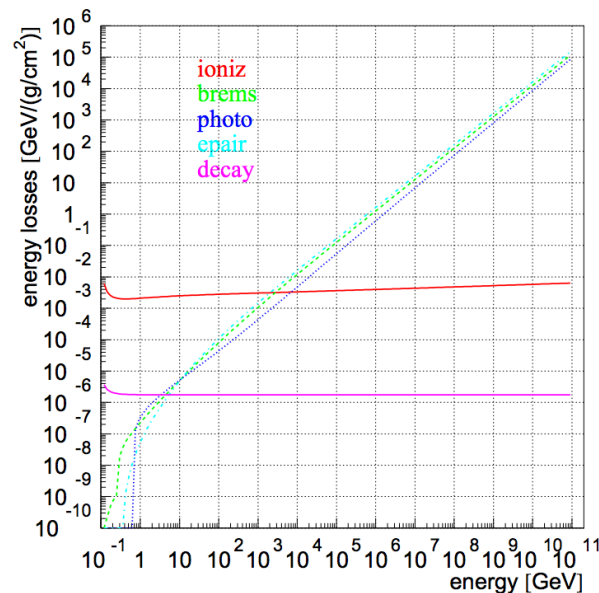


FIGURE 4.1: Relative energy loss from different mechanisms that affect muons as they propagate in ice, shown as a function of the muon energy[34].

4.4 Simulating Light Propagation

The charged particles produced in neutrino interactions produce light as they propagate in the ice via different energy loss mechanisms, notably Cherenkov emission.

Neutrino interactions involve the production of leptons and hadrons. With energies below 30 GeV these particles are propagated separately, in order to simulate the continuous and stochastic light emission due to energy losses. The simulated energy losses produce photons that require additional simulation, in order to include the optical properties of the ice, which affect the path of the photons.

The leptons and hadrons not being propagated by GEANT4 are propagated using *PROPOSAL*. *PROPOSAL* contains parameterization of ionization, electron pair production, bremsstrahlung, photonuclear interactions, and decay processes in ice. When the

particles are propagated through the ice, these processes are being simulated, giving photon emissions along the way.

4.4.1 CLSim

The photons produced by PROPOSAL and GEANT4 are propagated using *CLSim*, a photon propagation software package developed by IceCube [35]. IceCube uses other photon propagation software as well, but CLSim is the framework used in this thesis and will be the only one described in further detail.

CLSim is named after the programming framework *OpenCL* from which it is based. OpenCL is a framework that allows for kernels to be executed on a Graphical Processing Unit (GPU), ideal for highly parallelized programming[36]. Alternative frameworks exist for this purpose, but OpenCL distinguishes itself by being non-proprietary as well as allowing for the code to be executed on a central processing unit (CPU) without the need for modifications.

A typical muon event at the energies observed in IceCube, creates in excess of 10^7 Cherenkov photons. Each photon must be simulated individually, which becomes a very computationally expensive task. Running photon propagation code on GPUs allows for massive parallel programming, which has shown a significant acceleration of factors up to 150 or more (compared to a single CPU core)[35].

The number of parallel threads a processing unit can execute simultaneously depends on the number of cores available in the unit. The number of cores in desktop CPUs usually ranges from about 2-8, while GPUs can have several thousand. Parallelized programming on GPUs usually requires two conditions to be met: The code (kernel) being executed on the individual cores (or threads) must be the same, as well as the processes being independent of each other. Both of these conditions are met in photon propagation simulation, as the photons are described by the same behavior (uses the same code), and can be assumed uncorrelated with each other.

CLSim uses ray tracing algorithms to simulate the path of the photon through the ice, including optical properties such as scattering and absorption. The optical properties are based on an ice model that accounts for the anisotropy in the glacial ice of IceCube. Photons are simulated until they are absorbed in the ice or intersect a DOM. DOMs in CLSim are represented by *virtual spheres* with a user defined radius. The centers of the virtual spheres depend on the DOM positions fed by a GCD (Geometry Calibration and DetectorStatus) file; thus separate GCD files are used for DeepCore and the ICU simulation.

4.5 PMT Response

CLSim does not handle the PMT response simulation. It returns only the photons that intersected a virtual sphere, including the corresponding string and DOM number of the sphere it hit. Photons are treated individually when calculating the detection probability. The detection probability depends on several factors such as intersection point on the DOM, wavelength dependencies, and the direction of incidence. Separate algorithms have been designed for each DOM-type, in order to calculate the final detection probability.

CLSim is currently limited to a single radius and shape for all virtual spheres. Since the individual DOM-types (pDOM, D-Egg and mDOM) differ both in size and shape the photon positions must be corrected to accommodate this difference, in relation to the virtual sphere. The probability of a photon releasing a photo-electron (PE) from the photocathode in a PMT depends on several factors such as transmission probability through glass/gel, quantum efficiency, and the position and orientation of the PMT w.r.t. the photon.

4.5.1 pDOM and D-Egg

The pDOM is an updated version of the original IceCube DOMs that will be used in the ICU along the new DOM-types. The main difference comes from the design of the mainboard, but in simulation, the PMT response is calculated in the same way.

For pDOMs the photon acceptance probability is mainly based on two factors: the wavelength and angle of the photon. The angular dependence is based on the zenith angle θ of the photon w.r.t. the PMT orientation. It does not depend on the azimuth angle, as the pDOM has an approximately symmetric photon acceptance in azimuth. The angular photon acceptance curve for $\cos(\theta)$ going from -1 to 1 is shown in Figure 4.2a.

With a downwards-facing PMT, $\cos(\theta) = 1$ corresponds to a photon moving directly upwards (anti-parallel to PMT), $\cos(\theta) = 0$ is a photon moving horizontally (perpendicular to PMT), and $\cos(\theta) = -1$ is a photon moving downwards (parallel to PMT). The highest photon acceptance occurs at $\cos(\theta) = 1$, which is to be expected as it corresponds to a photon hitting the pDOM directly from below, normal to the PMT orientation.

For pDOMs the wavelength dependence describes the probability of the photon penetrating both glass and gel, in turn releasing a photo-electron from the PMT-cathode. The wavelength acceptance for photons between 290 nm and 700 nm is shown in Figure 4.2b, with a peak acceptance at wavelengths of around 420 nm with an acceptance of 10%.

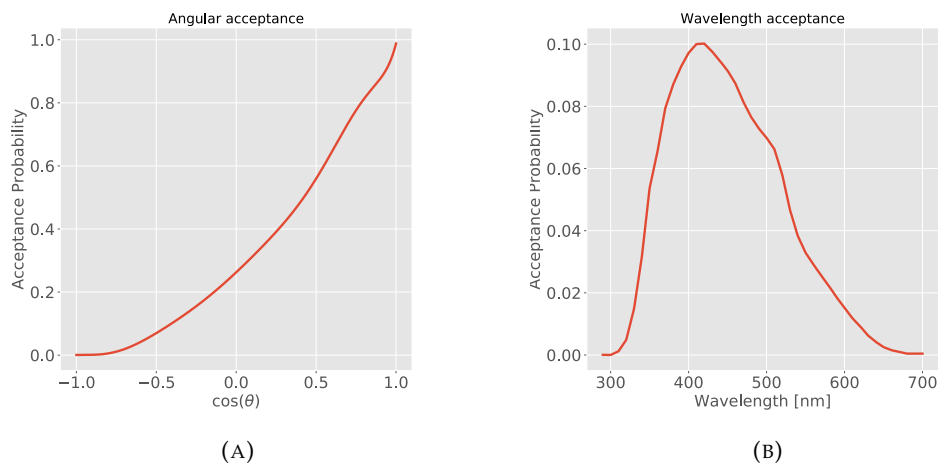


FIGURE 4.2: (A) Angular acceptance for the pDOM as a function of the zenith angle θ w.r.t. the DOM. (A) Wavelength acceptance curve as a function of the photon wavelength.

It should be noted that the wavelength acceptance shown in the figure is not determined by quantum efficiency (QE) alone, but includes the transmission through glass and gel. However, the QE is about 25% in a pDOM, suggesting that more than half of the photons are lost from propagating through the glass and gel. This seems unlikely, as the

glass and gel used in IceCube DOMs are chosen specifically for its good optical transmission properties. The reason for this low wavelength acceptance is still not known.

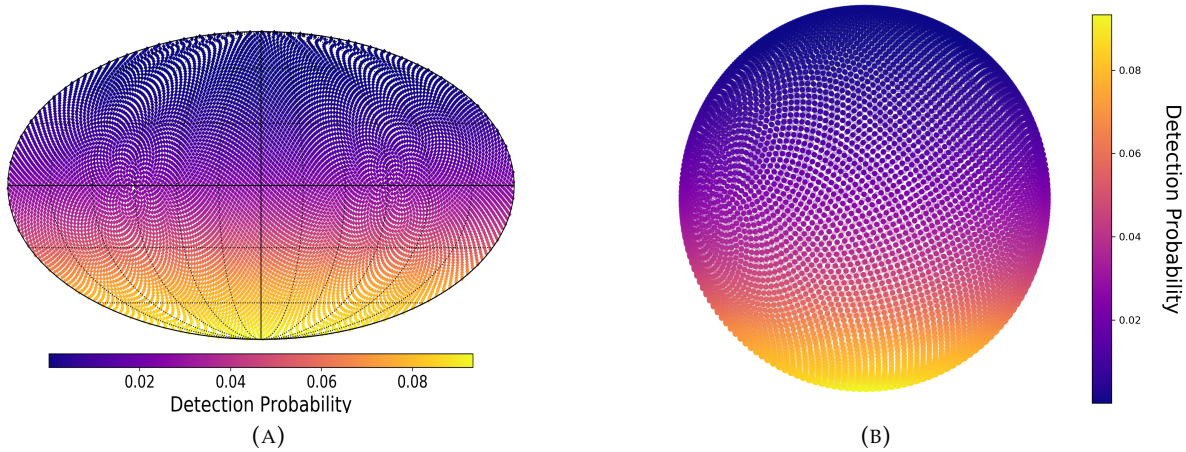


FIGURE 4.3: Total detection probability of photons coming from isotropic directions on a pDOM, (A) skymap-projection (B) 3D-view

The pDOMs PMT response algorithm was tested using a simulation of isotropically distributed photons on a virtual sphere. All photons have a wavelength of $\lambda = 394 \text{ nm}$ (close to the peak acceptance), and a direction oriented towards the center of the sphere. The detection probability was calculated for each photon and the results are shown in Figure 4.3a (skymap-projection), and Figure 4.3b (3D-view). Since the wavelength is constant, the change in detection probability is determined by the angular acceptance. The figures show a peak detection probability of less than 10%, and is dominated by the low wavelength acceptance as seen in Figure 4.2b ($P(\lambda = 394 \text{ nm}) \approx 10\%$).

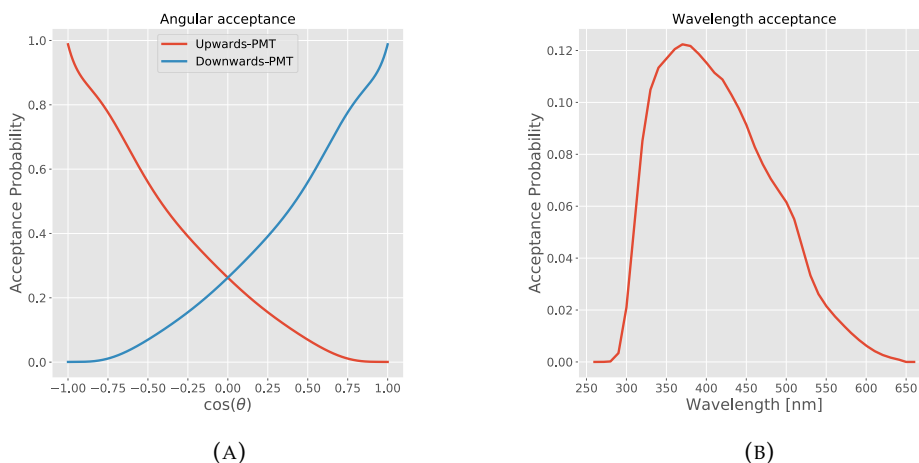


FIGURE 4.4: (A) Angular acceptance for the D-Egg as a function of the zenith angle θ w.r.t. each PMT: (red) upwards-facing PMT (blue) downwards-facing PMT. (B) Wavelength acceptance curve as a function of the photon wavelength.

D-Eggs are effectively two pDOMs put together, with one facing up and the other down, and the PMT response is calculated accordingly. The angular acceptance of the

two PMTs is the same, but mirrored as shown in Figure 4.4a, where (red) is the upwards-PMT and (blue) the downwards-PMT. The wavelength acceptance is shown in Figure 4.4b. Results from the PMT response simulation test can be seen in figure 4.5. The peak acceptance is only slightly above 11%, and as with the pDOM, this value seems low.

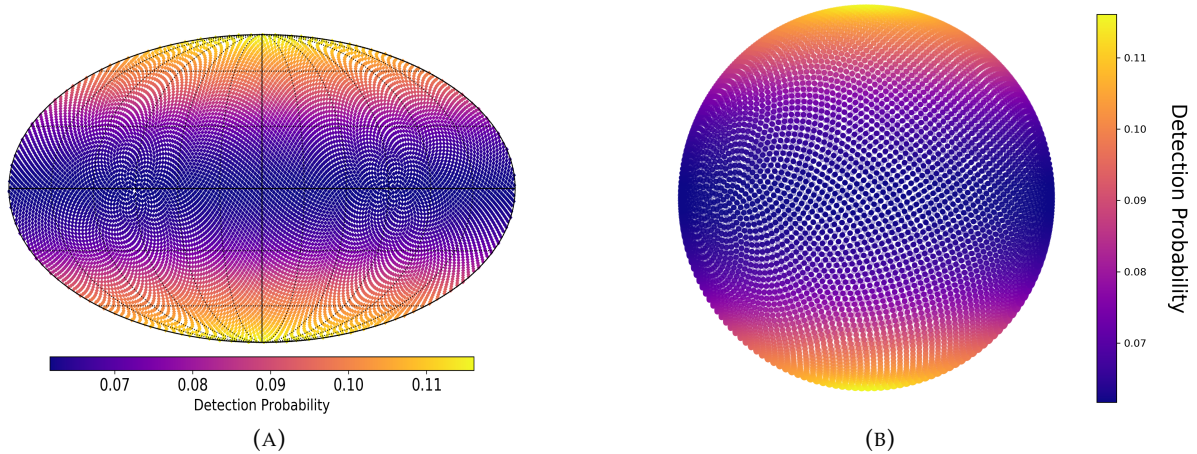


FIGURE 4.5: Total detection probability of photons coming from isotropic directions on a D-Egg, (A) skymap-projection (B) 3D-view

4.5.2 mDOM

The mDOMs are slightly more complicated and are treated in more detail when calculating the PMT response. The detection probability relies on four different factors: The angle and wavelength of the photon, as well as the transmission probability through the glass and the gel, depending on the photons path-length through both materials. For the pDOM and D-Egg the glass and gel transmission probability is included in the wavelength dependence term shown in Figures 4.2b and 4.4b.

The transmission probability for the mDOMs PMT response is divided into: PMT quantum efficiency (QE), glass transmission, and gel transmission. The glass and gel transmission probability depends on both the wavelength and the path-length of the photons through the material. The path-length is calculated using the photons (corrected) position and direction w.r.t. the mDOM. For the calculations, the PMTs in the mDOM are treated as discs, and only considers photons intersecting a PMT-disc from the front. The transmission probability is defined as

$$P_{Glass,Gel}(\lambda) = \exp(-x_{glass} / \Lambda_{glass}(\lambda) - x_{gel} / \Lambda_{gel}(\lambda)) \quad (4.1)$$

where x is the path-length in the material and $\Lambda(\lambda)$ is the absorption length in the material as a function the wavelength λ . Figure 4.6a shows the absorption length through glass and gel as a function of the wavelength, while Figure 4.6b shows the acceptance probability calculated from Equation (4.1) using $x_{glass} = x_{gel} = 2$ cm.

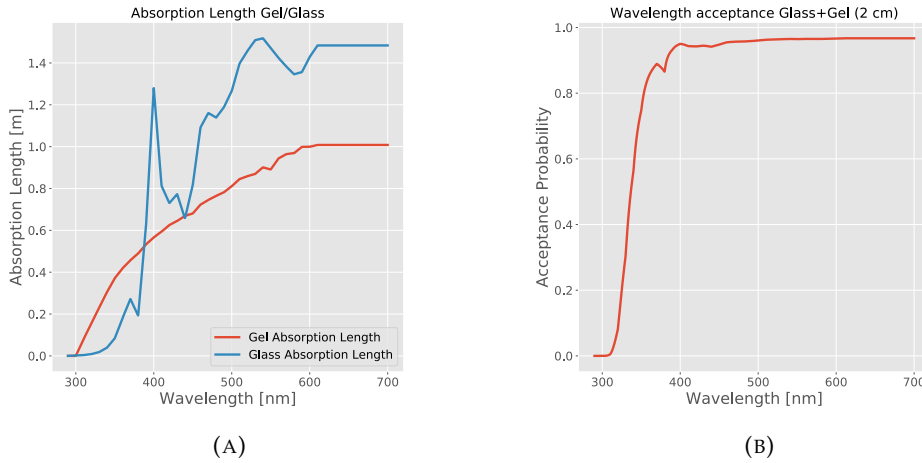


FIGURE 4.6: (A) Absorption length as a function of wavelength for (red) gel and (blue) glass. (B) Combined transmission probability as a function of wavelength calculated using Equation (4.1) with $x_{glass} = x_{gel} = 2$ cm.

The mDOMs angular acceptance is shown in Figure 4.7a for $\cos(\theta)$ between -1 to 1. The angular acceptance cuts off at $\cos(\theta) < 0$, which is due to the PMT-circle approximation where photons coming from behind the PMT are not considered. The wavelength acceptance is shown in Figure 4.7b for photon wavelengths between 290 and 700 nm. When comparing the acceptance probability scale to Figures 4.2b and 4.4b it is noticeably higher at the peak. This is because, in contrast to pDOM and D-Eggs, photons acceptance have a hard cutoff in the angular acceptance, whereas the pDOM and D-Eggs always have a finite probability.

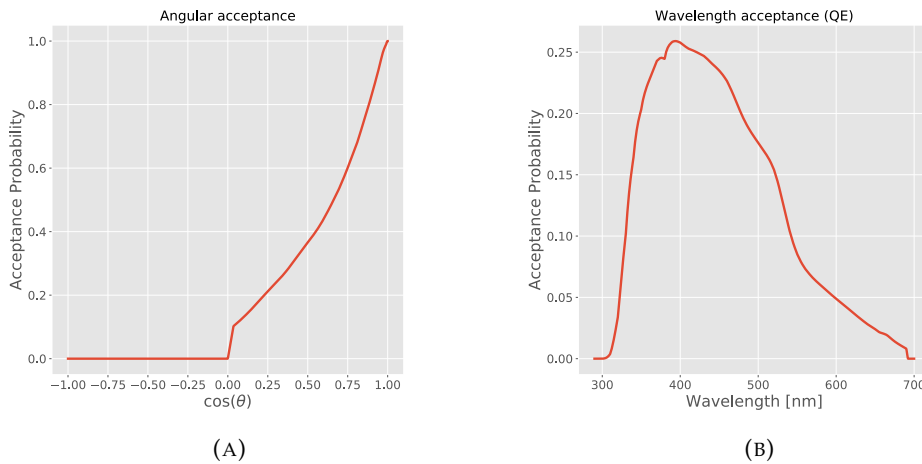


FIGURE 4.7: (A) Angular acceptance as a function of the zenith angle θ w.r.t. the DOM. (B) Wavelength acceptance curve as a function of the photon wavelength.

The PMT response test on the mDOM is shown in Figure 4.8, where photons with 0% detection probability are shown by translucent gray dots. The acceptance probabilities in the figure are significantly higher than those in Figures 4.2 and 4.5. It is important to notice that the detection probability shown in Figure 4.8 does not reflect the average

detection probability, that in reality is lower from the contribution of photons with 0% detection probability, which is different for the other modules.

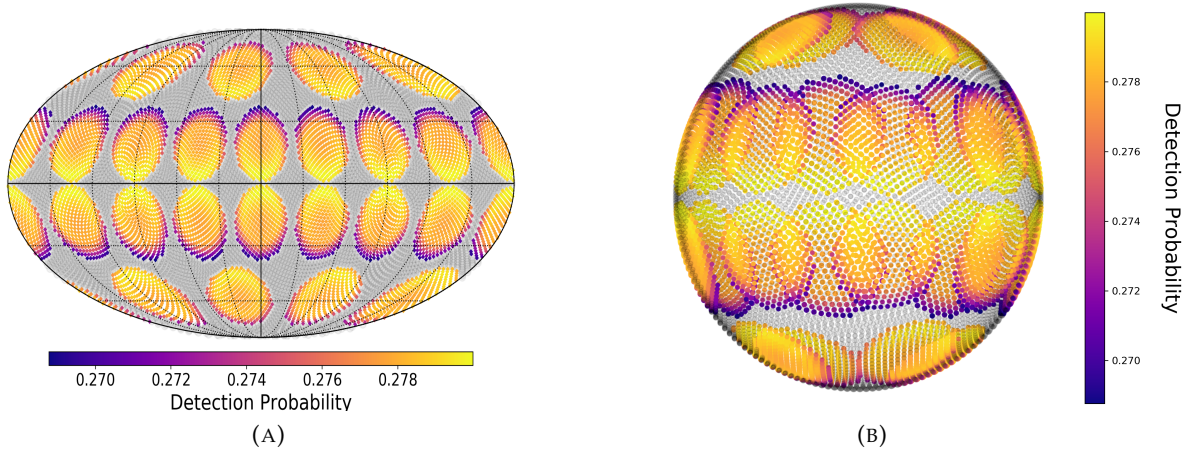


FIGURE 4.8: Total detection probability of photons coming from isotropic directions on an mDOM. (A) skymap-projection (B) 3D-view

4.5.3 Single Photo-Electron Template

The signal being measured when a photo-electron (PE) is emitted from the photocathode in a PMT varies between individual hits. IceCube simulation uses a **Single PhotoElectron** template (SPE template) to model the response measured in the PMT to a number of PEs. The SPE template consists of two components: A Gaussian and an exponential. The full model (black solid), as well as the Gaussian (red dash-dotted) and exponential (blue dash-dotted) is shown in Figure 4.9.

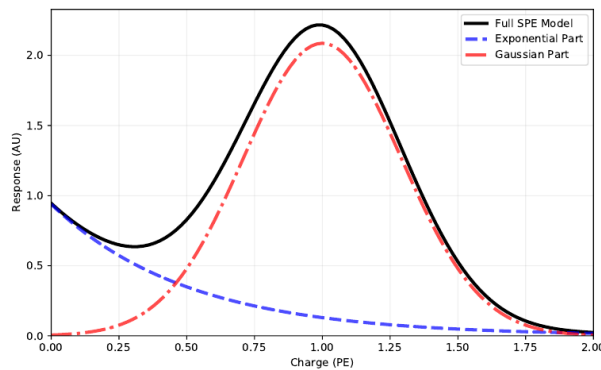


FIGURE 4.9: Single photoelectron template, used to model the response from a DOMs PMT in number of PEs [26].

The Gaussian component is related to the stochasticity of the dynode amplification. The exponential component consists of a combination of noise and cases where the initial photo-electron misses the first dynode plate, in turn losing a big fraction of the final signal. The template is calculated using laboratory measurements on 118 DOMs, done prior to deployment [37].

Photon hits from simulation with a non-zero detection probability are evaluated using a random number generator (RNG) to draw from a uniform distribution between 0 and

1. If the detection probability is greater than the random value, it is treated as the photon having emitted a PE. The final PMT response is then calculated by drawing from the distribution (black line) shown in 4.9.

4.6 Simulating noise

Hits that are not triggered by charged particles in the ice (dark noise), must be included in the simulation to properly reflect what is observed in IceCube (dark noise is described in section 3.1.4).

Noise hits are modeled using *Vuvuzela*[26][17], which is a noise simulation module used by IceCube. The noise consists of a Poissonian and non-Poissonian. The Poissonian component resulting from thermal noise and radioactive decay processes is being simulated using rates fit to each of the DOMs in the detector. The thermal noise is a large component of noise in IceCube DOMs, with a rate of about 200 Hz, while the noise from traces of radioactive elements in the DOM glass has typical rates between 50-100 Hz. The non-Poissonian component from the model adds additional noise with a rate of 400 Hz[26].

Noise hits are included in the simulated data samples used for reconstruction, and are being treated as *real* hits, as they would in observations at IceCube. Algorithms are often applied to the series of pulses in the data sample, removing most of the noise hits.

5 Neutrino Reconstruction

In particle physics, reconstruction refers to the process of inferring knowledge of what was observed in a detector, based on the signals measured. In IceCube, all information is obtained from photons emitted by particles from neutrino interactions. Since neutrinos are neutral, they do not leave any trace in the IceCube detector until they scatter on a nucleus or quark in the ice, producing a shower of particles.

The number of photons produced in an interaction depends on the energy of the neutrino involved. The IceCube detector is huge, as it is designed to contain the enormous cascade of photons and long muon tracks produced by very high energy neutrinos ($E > 1$ PeV), in turn making the instrumentation in the detector sparse, with more than 100 m between individual strings. In low energy events ($E < 100$ GeV), the sparsity of the instrumentation becomes a big problem, as the low number of photons produced in the neutrino interactions leaves only a few hits in the detector.

Low energy neutrinos are very important for oscillation analyses in IceCube, since the neutrino oscillation probability becomes negligible at energies above ~ 100 GeV for baselines in the order of Earth's diameter (as seen in Figure 5.1). This was one of the motivations behind DeepCore, as the dense instrumentation allows for the detection of neutrinos with energies $\simeq 10$ GeV.

Figure 5.1 shows the survival probability of a ν_μ as a function of neutrino energy and $\text{Cos}(\text{Zenith})$ (baseline). As is evident from the figure, the neutrino oscillation probability is very reliant on the energy E and zenith angle θ of the neutrino, in turn making them the two most significant reconstruction parameters oscillation physics.

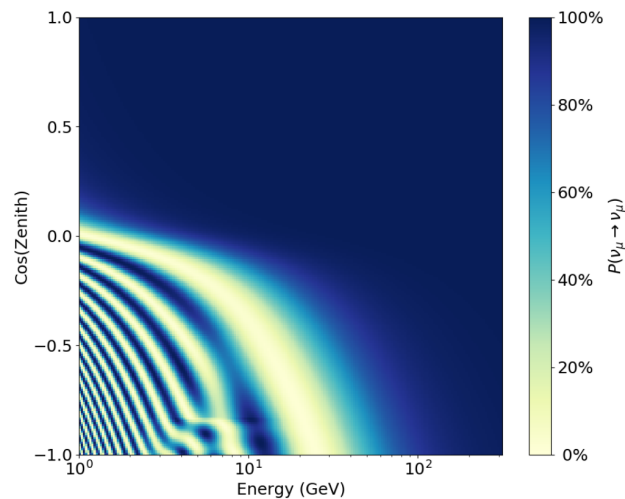


FIGURE 5.1: Survival probability of a ν_μ as a function of energy and $\text{Cos}(\text{Zenith})$ (baseline)[26].

Reconstruction becomes increasingly difficult at lower neutrino energies, as the light distribution becomes less reliant and uncertainties from noise hits can become dominant. In this thesis, the reconstruction of low energy neutrinos in DeepCore and the ICU is investigated using a new method that relies on direct simulation (*direct reconstruction*).

In addition, the performance of direct reconstruction is compared to the current final reconstruction method based on spline-tables.

5.1 Impact of Uncertainties in Reconstruction

Uncertainties in the reconstructed E and θ often become the biggest contribution to uncertainties in oscillation analyses. Figure 5.2 shows the survival probability of a ν_μ as a function of energy, calculated at a baseline corresponding Earth's diameter (12,700 km). The blue curve shows the true underlying survival probability as a function of energy, while the red dots show the estimated $P(\nu_\mu \rightarrow \nu_\mu)$ at different energies that are impacted by uncertainties in the reconstructed E . From the figure it becomes apparent that uncertainties in the energy can significantly impact the oscillation parameter fits, as the oscillation probability at specific energies becomes very uncertain. Improving the performance of the reconstruction directly impacts the quality of the fit. This is especially true at lower energies where the probability rapidly changes with energy.

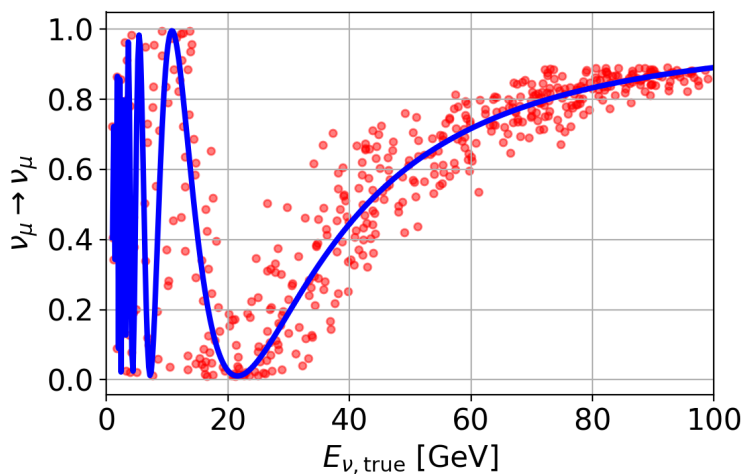


FIGURE 5.2: Uncertainties in the energy reconstruction are symbolized by the red dots, while the blue curve shows the true underlying oscillation probability. If the energy reconstruction was near perfect, the red dots would follow the blue line, strongly constraining the allowed fit parameters. As uncertainties in the energy reconstruction are present, especially at lower energies, the fit parameters are less restricted, causing uncertainties in the best fit values as a consequence.

The impact of an increased performance E reconstruction becomes especially apparent at low energies where the oscillation probability rapidly changes with energy. At the lowest neutrino energies up to a few GeV the oscillation probability changes so rapidly that it acts as a lower limit for neutrino oscillation experiments, the oscillation probability in this region can be assumed 0.5.

Currently, IceCube is only sensitive to the first peak/dip (around 15-20 GeV), because of the uncertainties in the energy reconstruction at lower energies. With an increased performance in the reconstruction at low energies, IceCube would be able to probe both the first and oscillation peaks. This would greatly impact the quality of the oscillation parameter fits, as the second peak would restrict the allowed parameter space considerably.

In IceCube, neutrino oscillation is mainly studied by looking at ν_μ disappearance and ν_τ appearance. As the name suggests, ν_μ disappearance is the deficit of observed ν_μ in

comparison to what is expected from the atmospheric neutrino flux. The ν_μ disappearance is due to the ν_μ having oscillated to other neutrino flavors, as it propagated through Earth. On the other hand, ν_τ appearance is determined by the number of observed ν_τ in the detector. Atmospheric ν_τ are very rare, making the observed ν_τ in IceCube the result of the others neutrino flavors (mainly ν_μ) having oscillated to ν_τ , hence ν_τ *appearance*. One of the strengths of the IceCube detector is its ability to observe neutrino with varying baselines. Since the atmospheric neutrino flux on Earth is isotropic, the neutrinos observed in IceCube have short as well as very long baselines.

5.2 Reconstruction Parameters

Neutrino events in IceCube can be described using 8 parameters

- Interaction vertex position: x, y, z
- Time of the interaction: **time**
- Direction in zenith: θ
- Direction in azimuth ϕ
- Energy: **E**
- Muon track length: **L**

The interaction vertex describes the position of the neutrino interaction in the spatial coordinates x, y, z . IceCube uses a coordinate system relative to the detector, with the origin situated about 2000 m below the surface of the ice, and the z-axis pointing upward normal to Earth's surface. **Time** describes the time of the interaction in nano-seconds relative to t_0 , with t_0 defined by the time window that starts about $1\mu\text{s}$ before the event was triggered. The direction of the neutrino is described using two angles: azimuth (ϕ) and zenith (θ) (as described in section 2.6). **E** describes the energy of the cascade created from the interaction and **L** describes the track length of the muon produced in ν_μ CC interactions. The track length is used to identify ν_μ CC events, as it is unique for this interaction, as e and τ leptons decay too quickly to leave a track (except occasionally when a μ is produced from the τ decay). The reconstructed track-length **L** is important in neutrino oscillation physics since it is directly relates to the energy of the muon.

As events become lower in energy, the muon track-length approaches distances close to the size of cascades, and the two event topologies become difficult to distinguish. Muons travel roughly 5 m per GeV of energy at the energies in DeepCore. With a standard IceCube string-spacing (125 m), a muon needs an energy of at least 100 GeV to pass four strings. In contrast, DeepCore, with its lower string spacing, allows the detection of muon tracks at much lower energies (~ 10 GeV).

Knowing the event-topology prior to reconstruction often becomes difficult at low energies. The common approach in dealing with this problem involves doing two separate reconstructions, one using a single cascade hypothesis, and the other a track + cascade hypothesis. The hypothesis that best matches the observation decides the outcome of the final reconstruction.

As this thesis focuses on cascade reconstruction alone, the track-length **L** will be disregarded and not referenced further, leaving the reconstruction parameters defined as: $x, y, z, \text{time}, \phi, \theta, E$.

5.3 The Likelihood Model

The strategy employed in low energy reconstruction relies on utilizing simulation as a way to predict the hits in space and time for a given hypothesis. The hypothesis is modified as part of an iterative process to find the one that best matches the observation. To measure how well a hypothesis matches an observation, a likelihood function that relies on the relationship between the predicted and observed hits is evaluated at every iteration in the reconstruction process, guiding the algorithm towards the most probable hypothesis.

The light profile from electromagnetic and hadronic cascades have light emission that scales linearly with the energy. This allows for the showers to be used as a fundamental energy unit that scales a template simulation to match the energy from the observed data. The energy from a cascade can be estimated by comparing the number of photons in a bin (DOM) k , to the expectation Λ from a template event with a reference energy (usually 1 GeV) [14]. The template functions are typically created using tabulated Monte Carlo simulation (*spline-tables*), but can also be derived from analytical approximations and direct Monte Carlo simulation (as for *direct reconstruction*).

The number of detected photons in a bin is expected to follow a Poisson distribution with a mean value $\lambda = \Lambda E$. The Poisson likelihood function \mathcal{L} is formulated as

$$\mathcal{L} = \frac{\lambda^k}{k!} \cdot e^{-\lambda} \quad (5.1)$$

which expressed in terms of $\lambda = \Lambda E$ gives

$$\mathcal{L} = \frac{(\Lambda E)^k}{k!} \cdot e^{-\Lambda E}. \quad (5.2)$$

Using the natural logarithm of the likelihood $\ln \mathcal{L}$ and adding the contribution from each DOM-bin, Equation 5.2 becomes

$$\ln \mathcal{L} = \sum_{i=1}^{N_{DOMs}} k_i \ln(\Lambda_i E) - \Lambda_i E - \ln(k_i!) \quad (5.3)$$

This expression can be maximized by setting $\frac{\partial \sum \ln \mathcal{L}}{\partial E} = 0$ and expressing it in terms of E

$$\begin{aligned} 0 &= \sum_{i=1}^{N_{DOMs}} \frac{k_i \Lambda_i}{\Lambda_i E} - \Lambda_i \\ &= \sum_{i=1}^{N_{DOMs}} \frac{k_i}{E} - \Lambda_i \\ E &= \sum_{i=1}^{N_{DOMs}} \frac{k_i}{\Lambda_i} \end{aligned} \quad (5.4)$$

Contribution from noise hits can be included by changing $\lambda = \Lambda E \rightarrow \lambda = \Lambda E + \rho$, with ρ being expected number of noise hits. The log-likelihood expression including noise becomes

$$\ln \mathcal{L} = \sum_{i=1}^{N_{DOMs}} k_i \ln(\Lambda_i E + \rho) - (\Lambda_i E + \rho) - \ln(k_i!). \quad (5.5)$$

Equation (5.5), as opposed to Equation (5.3), does not have a closed-form solution in terms of E . However, the solution can still be obtained numerically using gradient-descent minimization algorithms[14].

It is possible to include timing information from the photons as well, which in general improves the performance of the reconstruction. Timing is added by separating DOM hits in bins based on the arrival times of the photons. From this, Λ_i becomes the expected number of hits in a bin within some time window. In reconstruction, the time window in the i 'th bin is usually defined using the observed hits k_i .

In reality, the expected light yield Λ does not depend on the energy alone. The expected light yield in a DOM depends on the DOM-position ($x_{DOM}, y_{DOM}, z_{DOM}$), the position of the interaction vertex (x_v, y_v, z_v), the direction of neutrino (θ, ϕ) as well as the **time** of the interaction. The photon distribution also relies on the optical properties of the ice, as the interaction vertex usually sits a few scattering lengths away from the observer, as well as the complex wavelength dependency of photons. This, in turn, makes an analytical form of Λ impossible. In simulation, Λ becomes a function of the 7 reconstruction parameters used to describe the neutrino interaction. Using $\Theta = [x, y, z, time, \phi, \theta, E]$, the likelihood function in reconstruction becomes

$$\ln \mathcal{L}(\Theta) = \sum_{i=1}^{N_{DOMs}} k_i \ln(\Lambda_i(\Theta) + \rho) - (\Lambda_i(\Theta) + \rho) - \ln(k_i!). \quad (5.6)$$

In situations where speed is more essential than accuracy, analytical approximations to Λ exist. However, in reconstruction, Λ is primarily obtained using Monte Carlo simulation, although analytical approximations can be used as an initial guess (seed) for the minimizer algorithm.

Two separate reconstruction methods based on Monte Carlo are used in this thesis. The first reconstruction method relies on tabulated Monte Carlo simulation of light distribution in the detector smoothed with a multi-dimensional spline surface, in order to compute Λ . Reconstruction using spline-tables is currently the favored final reconstruction method in IceCube, and was applied in the most recent generation of oscillation analysis[26]. The other reconstruction method uses direct simulation as a way to compute Λ during the minimization process, and is the reconstruction method investigated in this thesis.

5.4 Table Reconstruction

The splines-tables are constructed through Monte Carlo simulation based on different source configurations in the detector. The simulation results provide a Cumulative Density Function (CDF) of the light yield, that is smoothed using a multi-dimensional spline surface fit, that provides a high-quality parameterization of the expected light yield Λ , for a given source configuration.

By using symmetries in the IceCube detector, the dimensionality of the tables can be reduced. Particularly the azimuthal and lateral translational symmetry of light propagation allow for a parameterization of Λ that depends on just 6 parameters: Depth, zenith angle from source, displacements vector to the receiver and the time difference in light detection between production and observation. Table lookups are independent of the energy, as Λ always corresponds to a 1 GeV hypothesis. In reconstruction, Λ is scaled by the energy of the hypothesis being evaluating the log-likelihood (LLH).

Figure 5.3a shows the raw CDF as a function of source depth and zenith angle. Figure 5.3b shows a slice from 5.3a at a source depth of 4.44 m, showing the discrete values of the CDF and the spline-fit. The spline-tables are about 1 GB in size that must be kept in memory for efficiency, with a lookup time in the order of $1\mu\text{s}$.

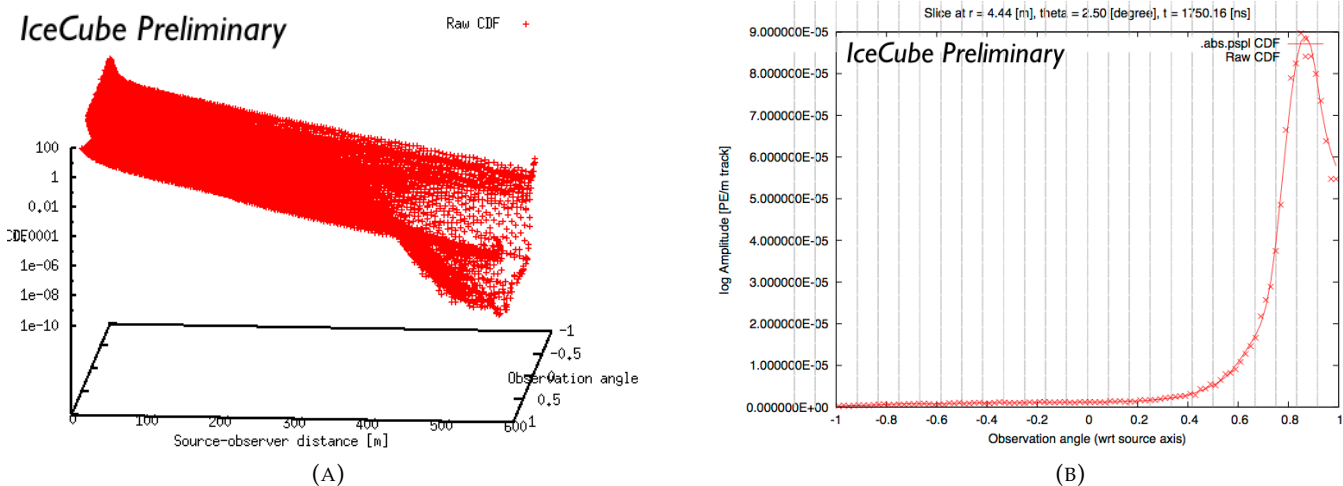


FIGURE 5.3: (A) A 2-dimensional slice from the cascade spline-tables. Each point shows the CDF of the light yield for a specific source depth and zenith angle. (B) Discrete values and spline fit for a specific source depth in (A). [38].

5.5 Direct Reconstruction

Direct reconstruction uses cascade simulations to directly compute the expected light yield Λ for a given hypothesis. The direct simulation uses a cascade parametrization modeled as a point-like emission, producing photons that are propagated afterward using CLSim (CLSim is described in section 4.4.1). Direct reconstruction relies on evaluating the log-likelihood (LLH) gradient directly, using the 7 reconstruction parameter. The reconstruction process uses a minimization algorithm to perform gradient descent, similar to the table reconstruction. Figure 5.4 shows an illustration of the process involved when computing Λ through direct simulation.

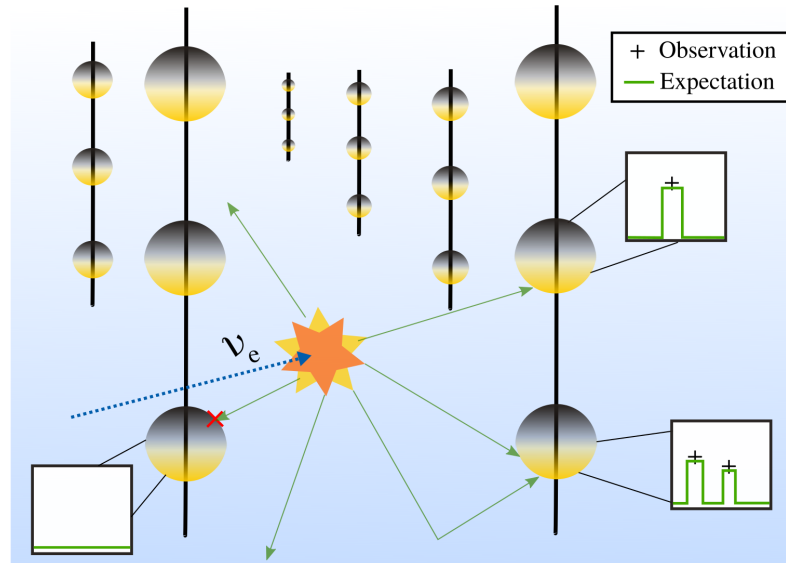


FIGURE 5.4: Illustration of direct simulation computing the expected light yield Λ , using a cascade hypothesis in the ice of IceCube. Photons produced in the cascade are propagated in the ice, and as they hit a DOM they are binned in time (shown in the histogram), from which the hypothesis can be evaluated based on the hits from the observation.

In direct simulation, the cascade hypothesis is simulated multiple times, as simulating the cascade hypothesis only once does not necessarily yield a representative light distribution. Effects such as scattering in the ice during photon propagation result in a different Λ from one simulation to another, and by simulating the cascade hypothesis multiple times, statistical uncertainties from the simulation are smoothed. The number of simulation trials is referred to as the *oversampling* factor (illustrated in Figure 5.5).

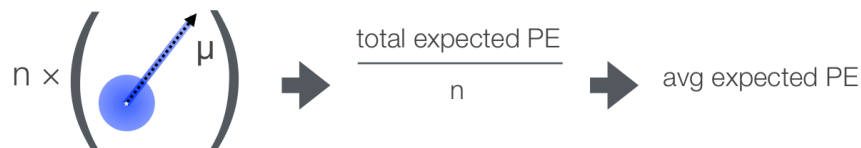


FIGURE 5.5: In direct reconstruction, a neutrino cascade hypothesis must be evaluated through several trials to smooth out statistical uncertainties. The number of simulation trials for a single evaluation is referred to as *oversampling* [39].

In direct reconstruction, the oversampling factor is usually in the order of 10^3 , though it depends on the accuracy desired Λ as well as the event itself. The oversampling factor is a trade-off between computation time and accuracy, and choosing an optimal oversampling factor is not always trivial, as it can depend on the minimizer's sensitivity to fluctuations in the LLH, as well as the average number of iterations needed for the reconstruction to complete.

In direct reconstruction, the main computational expense comes from the photon propagation. For this thesis, CLSim is used for the photon propagation in the direct simulation. Since CLSim is optimized for photon propagation on GPUs, direct reconstruction is best run on a computer with GPUs available, since running photon propagation on a CPU is many times slower (factor 10-100).

5.6 Spline-tables versus Direct Simulation

The two reconstruction methods each come with advantages and disadvantages. The main benefit of the tables is that lookups are very fast, allowing for fast reconstructions. The tables have shown to perform well in comparison to other reconstruction methods, which is the reason why it is currently used for the final reconstruction in IceCube analyses.

Constructing a set of spline-tables requires huge amounts of simulation time, as all possible source configurations must be covered. The process of creating and verifying a set of tables usually costs about 6 months of a PhD students time. This would not be an issue if the tables never had to be replaced. However, as the simulation keeps improving and better models of the complex glacial ice are derived, a new set of tables must be constructed to include this new information.

With tables already being 1 GB in size they are starting to reach their limit, as this becomes significant when running the reconstruction using distributed computing on several 100-1000 computers. For this reason, expanding the dimensionality of the tables becomes an issue. Currently, the tables are constructed under the assumption that DOMs are of the same type, and with the introduction of DOMs with multiple-oriented PMTs, tables would need to expand the dimensionality to include this information, as symmetries previously used breaks down. Currently, tables have been constructed for the ICU, but are based on a homogeneous ice model and cannot be used for real data collected by the ICU.

The benefit of direct reconstruction lies with its flexibility and the more accurately computed light yield, as it is based on direct simulation and not a parameterization like the tables. In addition, direct reconstruction it not restricted to a homogeneous ice model when used for reconstruction in the ICU. The new DOMs with multi-oriented PMTs can have their full potential utilized, without the loss of accuracy due to approximations, such as simple ice models.

Direct reconstruction is faced with two issues that currently make it less desired than table-reconstruction. The evaluation time of a hypothesis is much longer in direct reconstruction, since the hypothesis must directly simulated, and often requires a high oversampling factor (>1000) for a good performance.

In addition, the current performance of direct reconstruction is not entirely on par with the table reconstruction, even at high oversampling. This is unexpected, as the Λ computed in direct simulation should be at least as, or more, accurate than the one gotten from table lookups. Though if the issue in performance can be solved, direct reconstruction becomes a good candidate for replacing table reconstruction in the ICU, which is urgently needed. The investigation of direct reconstruction is covered in section 6, using simulation from DeepCore and the ICU, while comparing the performance with table-based reconstruction.

5.7 Millipede

Millipede is a reconstruction framework developed by IceCube, and is used by table reconstruction as well as direct reconstruction. Millipede is used to set up the full reconstruction process, allowing for different minimizer algorithms to be used in the reconstruction. Millipede also handles the construction of the time bins, that is calculated based on the hits in the event being reconstructed.

5.7.1 Time binning

The hits in the detector that represents an event consist of a set of *pulses*, that can vary in amplitude and width. Each pulse is mapped using an *OMKey* that contains the string, module, and PMT number. Millipede uses the pulses of an event to construct the time bins, based on settings configurable by the user. Multiple pulses can be merged in single bins if they are close in time. When setting the input variable *PhotonsPerBin* to -1, time binning is not used, and all pulses sharing an *OMKey* are merged into a single bin, spanning the full time window of the event.

For PMTs without any pulses, a single bin is created that spans the full time window. If a single pulse was observed, three bins are created. The first bin covers the beginning of the time window to the pulse. The middle bin contains the observed pulse, and has a bin width corresponding to the pulse width, and the last bin covers the remaining time window. The width of pulses is of order $O(1-30 \text{ ns})$, while the full time window covers a whole μs . As a result, the initial and final time bins are much larger in comparison to the bins containing pulses.

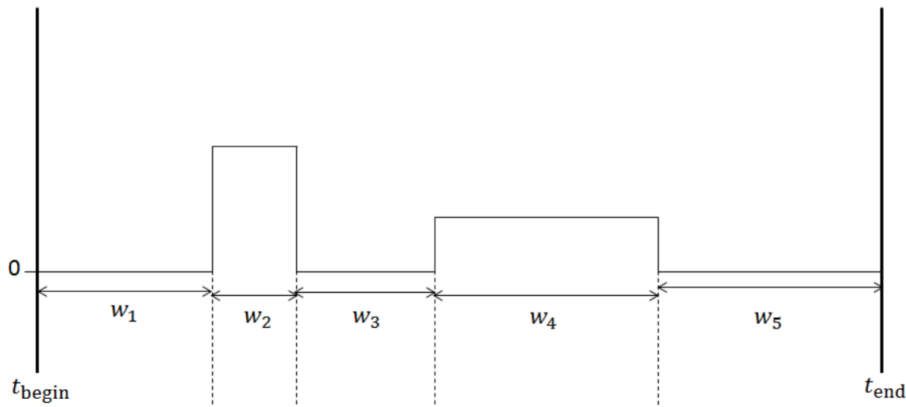


FIGURE 5.6: Simple example of a possible time binning created by millipede based on two pulses. The two pulses are binned in w_2 and w_4 with widths in the order of $O(1-30 \text{ ns})$. The widths of w_1 and w_5 are typically much larger than the pulse bins, as they cover the remaining time window that covers a whole μs . Illustration from [40].

5.7.2 Likelihood Functions

The default likelihood function used in millipede is a Poisson log-likelihood (LLH) very similar to Equation (5.5), defined as

$$\ln \mathcal{L} = \sum_{i=1}^{N_{bins}} k_i \ln(\Lambda_i) - \Lambda_i - \ln \Gamma(k_i + 1). \quad (5.7)$$

Table reconstruction uses the LLH function in Equation (5.7). Direct reconstruction uses a different LLH function called the *DIMA-LLH*, named after the founder. The DIMA-LLH accounts for model errors and weighted simulation[**DIMA-LLH**]. The version of the DIMA-LLH used for direct reconstruction is slight different, as it only uses the weighted simulation terms

$$\ln \mathcal{L}_{DIMA} = \sum_{i=1}^{N_{bins}} n_s \cdot s_i \cdot \ln\left(\frac{\mu_i}{s}\right) + d_i \cdot \ln\left(\frac{\mu_i}{d_i}\right), \quad (5.8)$$

where μ is defined as

$$\mu_i = (n_s \cdot s_i + d_i) / (n_s + 1). \quad (5.9)$$

Here, d_i and s_i is the observed and expected charge in the i 'th bin respectively and n_s is the number of simulated trials (oversampling). Direct reconstruction can use the Poisson-LLH in Equation 5.7 for reconstruction as well. The effects from switching between the two LLH functions in direct reconstruction is still not understood in detail, and require more careful investigation, though in general DIMA-LLH has been observed to perform slightly better.

5.7.3 Energy Reconstruction

In millipede, energy reconstruction can be handled in two separate ways. The first one is by allowing the minimizer to adjust E , along with the other 6 reconstruction parameters. Alternative, millipede has an analytical energy fitting method based on Preconditioned Conjugate Gradient (PCG) Poisson fit[41].

The PCG energy fit in millipede was originally designed for table reconstruction but can be used in direct reconstruction as well. Since tables do not include a dimension for the energy, table lookups of Λ correspond to a 1 GeV cascade hypothesis. For this reason, millipede's PCG fit is specifically designed for a 1 GeV Λ , which is not what is computed in direct simulation, as it depends on the energy of the cascade hypothesis. By downscaling the Λ computed in direct simulation by the energy of cascade simulated, direct reconstruction can use the PCG energy fit. The PCG fit returns a scaling factor for Λ that is applied before the likelihood evaluation.

Using the PCG energy fit in direct reconstruction has shown equal performance to using the minimizer, and it is still undecided which method is the preferred.

5.7.4 The Simplex Algorithm

Millipede allows for a variety of minimization algorithms to be used in the reconstruction. The Simplex algorithm is the only one used for reconstruction in this thesis, and will be the only one described in detail. Millipede's simplex minimizer is based on the Nelder-Mead[42] variant (not be confused with Dantzig's simplex algorithm).

The simplex algorithm is a numerical minimization method used in optimization for multidimensional problems without the use of derivatives. The algorithm searches for the lowest point of the objective function, defined by the log-likelihood (LLH) in reconstruction.

The algorithm uses a *simplex*, a special type of polytope with $n+1$ vertices in an n -dimensional problems. The $n+1$ points in the simplex, as used as test points, that determines how the algorithm moves. Based on the LLH evaluated at each test point, a set of different progression techniques are applied, that move or replace test points in the simplex. The algorithm always maintains a total of $n+1$ test points. In millipede, the initial simplex of test points is based on the seed hypothesis and the defined step size.

Two criteria determine whether the minimization process terminates. The first criteria is based on the differences between the LLH in the simplex, stopping if it drops below a certain tolerance. The other criteria is based on the size simplex, stopping if the size drops below the tolerance.

6 Reconstruction Studies

In this section, the performance of direct reconstruction is compared to table reconstruction. The current limitations and possible improvements for direct reconstruction are investigated and discussed. The event reconstruction is limited to cascade events only (ν_e CC), as cascade+track reconstruction adds additional layers of complexity, which might overshadow more fundamental issues in the reconstruction method. In addition, direct reconstruction of cascades should show better, or equal, performance to table reconstruction before the more complex cascade+track reconstruction process is studied.

Reconstructions in this thesis use data samples that are based on Monte Carlo simulation and include only ν_e CC events (no NC). The performance of direct reconstruction is investigated using simulated data samples from DeepCore, as well as the ICU. The reconstruction has been optimized for low energy events, and the data samples contain energies ranging from 10 GeV to 100 GeV. The focus on low energy reconstruction is motivated by the impact of low energy neutrinos in oscillation analyses, as the atmospheric neutrino oscillations significantly reduce at energies above 100 GeV.

6.1 Investigating the Oversampling Factor

In direct reconstruction, the oversampling factor determines the number of times a cascade hypothesis is re-simulated, before the log-likelihood (LLH) function is evaluated. By simulating multiple times, the statistical uncertainties in the computed distribution of light is reduced. However, the oversampling factor becomes a trade-off between an accurate representation of the expected light yield Λ and the execution time of an evaluation.

6.1.1 Uncertainties in Likelihood Evaluations

During the direct reconstruction process, the hypotheses proposed by the minimizer is evaluated through direct simulation of a cascade event represented by the 7 parameters of the hypothesis (x , y , z , **time**, ϕ , θ , E). The validity of the hypothesis is evaluated by the log-likelihood (LLH) function, that depends on the expected light yield from the hypothesis Λ and the detector hits from the event being reconstructed. As uncertainties in Λ are present, because of the probabilistic nature of Monte Carlo simulation, the LLH is impacted as well. The uncertainty in LLH might cause problems in the minimization process, as even a good hypothesis can result in a bad LLH evaluation. The uncertainties can be mitigated by increasing the oversampling factor, yielding a more reliable Λ from the simulation, at the cost of longer evaluation times.

The impact of oversampling on the uncertainty in likelihood evaluations has been investigated using a cascade event (ν_e CC) with an energy of 36 GeV. The choice of the event was motivated by having an interaction vertex close to a string; increasing the available information. The event being tested is shown in Figure 6.1 and represents a *well behaved* event. Here, well behaved describes an event with a well-defined distribution of light, only few *unlucky* photon scatters in the ice, and where the noise cleaning has successfully removed the worst noise pulses. The size of the colored spheres in the figure

indicates the amount of charge observed in the DOM, while the color shows the time of the pulses, going from red to blue for early and late pulses respectively. The purple sphere indicates the interaction vertex of the event and the dotted line shows the neutrino direction, which in this case is upwards going ($\cos \theta$ close to -1).

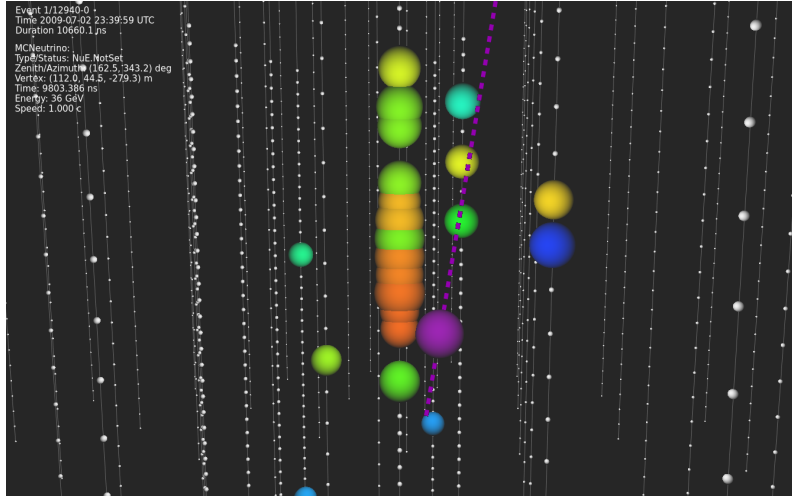


FIGURE 6.1: Cascade event from a 36 GeV ν_e CC interaction shown in IceCube’s event viewer. The size of the spheres indicate the amount of observed charge in a DOM, and the purple sphere shows the position of the interaction vertex of the event.

The true parameters of the event is used as the cascade hypothesis in the simulation. To clarify what is meant by *true parameters*: *true* refers to the fact that the event is based on simulation and the true information is available in the files (in contrast to real data), while *parameters* refer to the 7 reconstruction parameters used to defined a cascade event in simulation. For convenience the true parameters (\mathbf{x}_{true} , \mathbf{y}_{true} , \mathbf{z}_{true} , \mathbf{time}_{true} , ϕ_{true} , θ_{true} , E_{true}) as obtained from the event file, will be defined as Θ_{true} .

The uncertainty of the likelihood was investigated at five different oversampling factors, increasing an order of magnitude by each value. For a specific oversampling factor, 20 independent simulations were run, in turn calculating 20 independent LLH values for the same hypothesis (only LLH evaluations are run, not full fits). The uncertainty of the LLH is defined from the width of the 90% confidence bound of the 20 LLH values.

The results are presented in Figure 6.2 and show the uncertainty of the LLH reducing as the oversampling factor increases. This is expected since the statistical fluctuations from the Monte Carlo simulation should smooth as the number of cascade re-simulations increase.

The uncertainty in LLH is reduced by a factor ~ 6 when going from an oversampling factor of 10^2 to 10^6 . Having a more stable LLH might increase the performance of the direct reconstruction. However, the execution time grows almost linearly with oversampling, thus going from an oversampling factor of 10^2 to 10^6 , increases the evaluation time by a factor of 10^4 .

As part of this work, it has not been concluded whether the performance of direct reconstruction continuously grows with oversampling. It was observed that the performance didn’t significantly increase beyond oversampling factors of 10^4 in DeepCore reconstruction. The impact of an increased oversampling factor might vary depending on the minimizer algorithm, as some algorithms are more prone to an unstable likelihood space than others. Oversampling factors above 10^5 were never tested for full reconstructions, as the reconstruction time becomes too long for a representative sample to be produced. The results in Figure 6.2 are dependent on the chosen event and the hypothesis

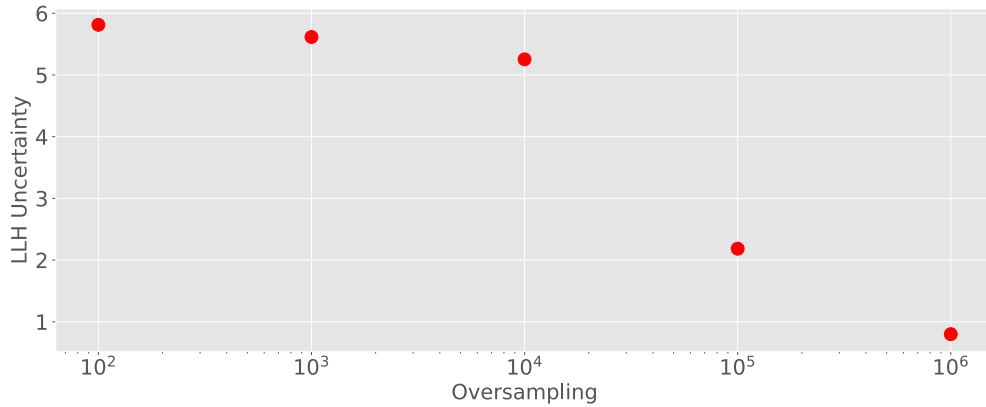


FIGURE 6.2: Uncertainty in the log-likelihood (LLH) tested at varying oversampling using direct simulation. The LLH uncertainty is calculated using the width of the 90% confidence bound from 20 LLH values calculated computed from independent simulation trials.

being evaluated, but the reduction in uncertainty for increasing oversampling is expected to follow the same behavior for other events.

6.1.2 Oversampling and energy fitting

During the investigation of the direct reconstruction algorithm, it was observed that the reconstructed energy E consistently increased with higher oversampling. This behavior was very unexpected, as an increase in oversampling simply increases the statistics. The trend was observed across multiple events, and was not due to unlucky reconstructions, as the reconstructions were repeated for the same events. The relationship between fitted energy and the oversampling factor was tested using three separate events with energies of 25 GeV, 26 GeV, and 36 GeV. The events were chosen based on inspection in the event viewer, determining that they were well behaved.

In the tests **only** the energy was fitted, using a cascade hypothesis in the direct simulation based on Θ_{true} . The energies were fitted using millipedes PCG fit (described in section 5.7.3). 10 independent energy fits were run for each oversampling factor to ensure the consistency of the fit. The energy fits were tested for oversampling factors between 10^2 and $8 \cdot 10^4$ and the results are shown in Figure 6.3(A, C, E) for each of the three events. The true energy of the event is shown by the horizontal black line, while the green line shows the energy fit from a table-based energy fit using the same hypothesis. The tests show a clear trend in the fitted energy as the oversampling factor increases, and is observed across all three events. The increase in fitted energy slows down as the oversampling factor becomes large ($>40,000$).

It was investigated whether the trend was due to a difference in the total light yield computed in the direct simulation as oversampling increased, but no such trend was found. Since the only component being fed to the PCG fit is the expected light Λ , in each time bin, it suggests that the trend in fitted energy stems from statistical effects in the sometimes narrow time bins used by millipede.

The statistical effect on the energy fit, from millipedes time bins, was tested using the setting *PhotonsPerBin* (PPB) that when set to -1 removes time binning in millipede, giving only a single bin for Λ in each PMT bin. Tests equal to those shown in Figure 6.3(A, C, E) were run using PPB = -1, and the results are shown in Figure 6.3(B, D, F). From the

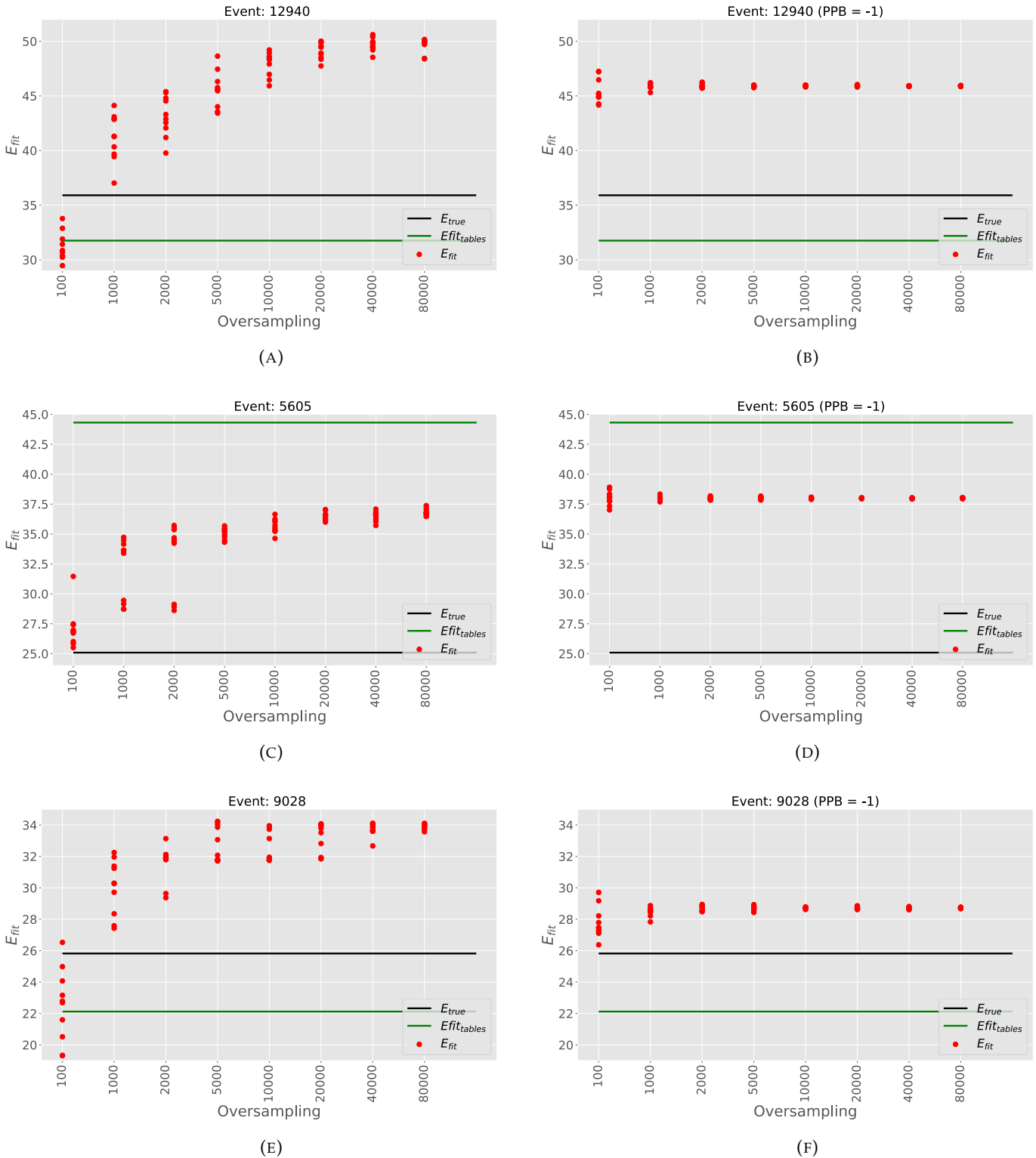


FIGURE 6.3: Three separate events fitted in energy using direct simulation and millipede's PCG energy fit. The cascade hypothesis used in the simulation is based on Θ_{true} of the events. The energy fits were tested at oversampling factors between 10^2 and $8 \cdot 10^4$. (A, C, E) show energy fits with time bins enabled in millipede. (B, D, F) show energy fits without time bins (PhotonsPerBin = -1).

figure it is evident that when using a single time bin the trend completely disappears, strongly suggesting that time binning in millipede is the root cause of the odd energy fitting behavior at varying oversampling.

When comparing the fitted energies in Figure 6.3 with and without time bins, two things become apparent. The fitted energies in the three events are being significantly overestimated, suggesting that there is a general bias in energy when using direct simulation. In addition, the energy fits for increasing oversampling, using time binning, does not converge towards the case with no time binning.

It becomes hard to interpret which method provides the best results, as they are both off the mark. In general, the most accurate energy fits occur at the lowest and second lowest oversampling factors. However, using a lower oversampling factor (fewer simulations) increase the uncertainties in Λ (as shown in Figure 6.2), which is not a favorable trait, even though it might produce more *accurate* energy fits.

The results suggest that there are some unresolved issues at the core of the simulation and evaluation process. The full explanation of the statistical effect has not been derived in this thesis, and requires a more detailed investigation of the statistical behavior of the time bins used in millipede when running direct simulation.

6.2 Likelihood Scans

The LLH landscape of an event can be investigated by evaluating discrete points in LLH space. In addition, the scans can provide insight into the LLH landscape of two dimensions as a function of each other.

As seen in the previous section, odd behavior was found when fitting the energy of an event using different oversampling factors. The effects from an increasing oversampling factor have been investigated using 2-dimensional LLH scans in energy E and zenith angle θ .

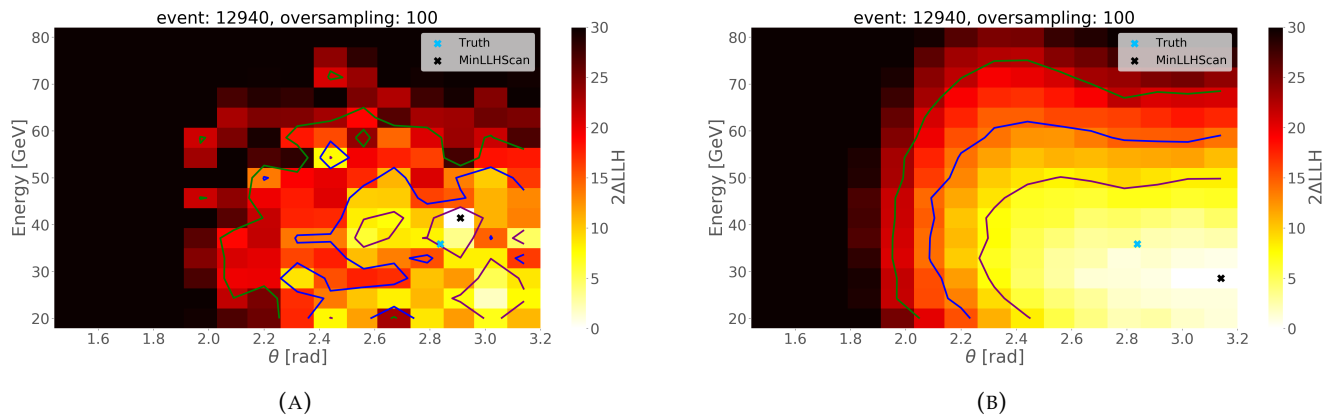


FIGURE 6.4: LLH scans in zenith angle θ and energy E , showcasing the need for making multiple scans to compensate for the uncertainties in LLH at low oversampling. (A) A single scan using an oversampling of 100. (B) The average grid value of 100 scans using an oversampling of 100.

As shown in Figure 6.2, the uncertainty in LLH depends on the oversampling factor. As a consequence, doing a single scan using a low oversampling factor, e.g. 100, will not yield a very meaningful representation LLH landscape, as it is dominated by fluctuations in LLH evaluations. This is illustrated in Figure 6.4a where a single scan was performed

in θ and E in the ranges $\theta = [\frac{\pi}{2}, \pi]$ rad and $E = [20, 80]$ GeV. Instead, by doing 100 scans using the same grid points and computing the average grid value, a more complete picture of the LLH landscape can be provided for low oversampling. This is illustrated in Figure 6.4b.

By using the average value of the grid points from multiple scans as in Figure 6.4b, similar tests as in Figure 6.3 can be performed. In Figures 6.4a and 6.4b the cascade hypothesis used in simulation is defined by Θ_{true} , with the exception of the two dimensions being scanned. The color in the scan shows the $2\Delta LLH$ defined as $2(LLH - LLH_{best})$, with LLH_{best} defined as the lowest $-LLH$ in the scan. LLH_{best} is marked by the black cross, while true event parameters are marked by the purple cross. The 1, 2 and 3 σ contours of the LLH landscape are shown as the purple, blue and green lines respectively, calculated using 7 degrees of freedom corresponding to the number of reconstruction parameters.

As was observed in Figure 6.3 the steepest change in the fitted energy occurred between 100 and 1000 oversampling. For this reason, the oversampling factors chosen for the LLH scans were 100, 500, 1000, and as an edge case 100,000 oversampling was chosen for the last scan.

In Figures 6.5a-6.5d LLH scans in θ and E are shown for oversampling factors of 100 (A), 500 (B), 1000 (C), and 100000 (D). The figures indicate a trending transformation of the LLH landscape in θ and E as the oversampling increases.

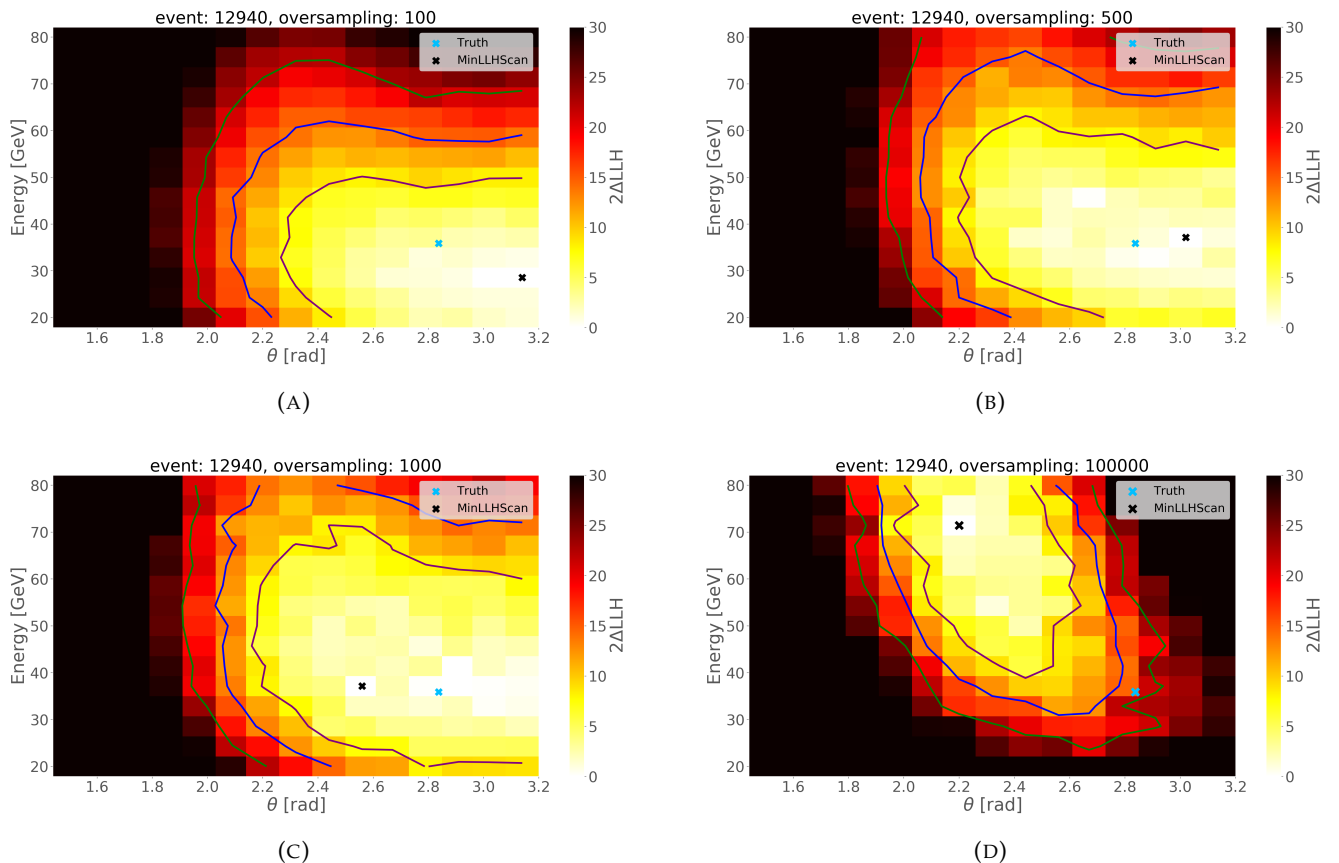


FIGURE 6.5: LLH scans in zenith angle θ and energy E for oversampling factors of (A) 100 (B) 500 (C) 1000 (D) 100000.

The minimum of the LLH landscape in the E -dimension increases with the oversampling, as expected from the observations in the previous section. A trend is seen in θ as well following a decreasing behavior as the oversampling increases. However, the

trend in θ cannot be generalizable as it is very dependent on the event, though it is still indicated that the LLH landscape of θ changes with oversampling factor.

From the behavior observed in the LLH scans it becomes hard to interpret results from direct simulation, as it is biased by the oversampling. Intuitively, a high oversampling should give better results as more statistics are produced, but from the scans shown in Figure 6.5, the directly opposite effect is observed. The worst overall best fit scan point was found in the scan using the highest oversampling.

No exact explanation was found describing the nature of the oversampling behavior, though clues from Figure 6.3 indicated that millipedes time bins might be part of the problem. However, time bins are important for the performance of the reconstruction; thus removing them is not a viable solution to the problem. Even though the results from the direct reconstruction become hard to interpret with what has observed in mind, the focus of this work is turned towards increasing the performance of the reconstruction algorithm in its current state.

6.3 Minimizer Movement

As a part of this work, millipede was updated to allow for the hypothesis being evaluated by the minimizer to be stored for later inspection. By looking at how the hypothesis is being changed by the minimizer, the movement of the algorithm can be visualized through the parameter(s) of the LLH space. Studying the movement of the minimizer can provide insight into whether the multi-dimensional LLH space is being properly explored, and can help debug issues related the minimizer algorithm. Looking at the behavior of the minimizer can also help with adjustment of settings such as step size and tolerance. In Figure 6.6 the minimizer movement from a direct reconstruction is shown for the θ and E dimensions. The movement of all parameters can be found in Appendix A.

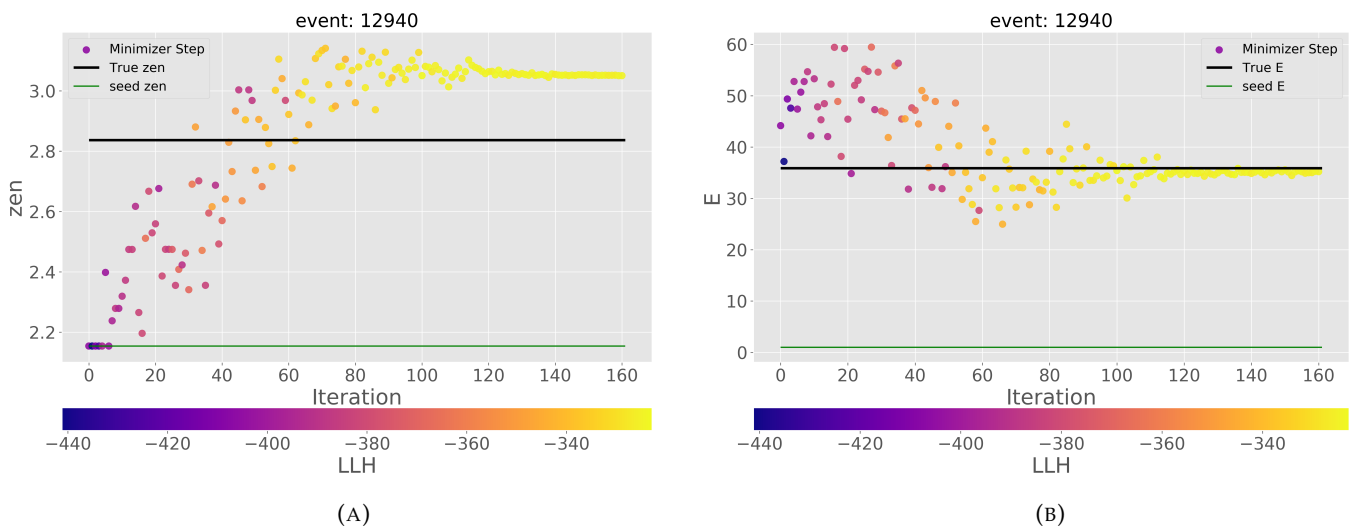


FIGURE 6.6: Minimizer movements from an event reconstruction in the parameters (A) zenith angle θ (B) energy E

The horizontal black line shows the true value of the event, while the green line shows the initial seed used in the reconstruction. The seed used in this reconstruction is based on an analytical fit for the primary vertex, and does not provide information about the energy of the event, which is why the energy starts a 1 GeV. The reconstruction uses

the PCG energy fit, and is why the reconstruction quickly moves away from the seed in Figure 6.6b. This is a consequence of the PCG fit being independent of the energy used in the simulation, as the computed Λ is downscaled to represent a 1 GeV cascade when using PCG (for details about PCG see section 5.7.3). The color scale of the dots indicate the LLH at each iteration and shows whether the minimizer is moving towards a better minimum in the LLH space.

The reason the algorithm is not moving in θ during the first few iterations is that the minimizer is setting up the initial simplex (see section 5.7.4 for info about the minimizer). From Figure 6.6 it is confirmed that the minimizer algorithm is moving towards a better minimum than what was provided by the seed.

The step size of the minimizer reduces as it approaches the minimum, which can be seen in the last iterations. The minimum found by the minimizer is not always the global minimum, as high dimensional LLH spaces are prone to having several local minima. However, the minimum found by the reconstruction in Figure 6.6 is clearly a better estimation of Θ_{true} than what was provided by the seed. It should be noted that the global minimum of the LLH rarely sits exactly at Θ_{true} , as scattering in the ice, limited statistics, and noise hits distort the LLH space.

6.4 Final Reconstruction DeepCore

This section covers the results from direct reconstruction of cascades in DeepCore, using a data sample based on DeepCore Monte Carlo simulation with energies from 10 to 100 GeV (the majority being below 20 GeV). The data sample used in the final reconstruction in DeepCore contains 865 ν_e events. The results are shown in Figures 6.7a and 6.7b for the reconstructed θ and E respectively, showing table reconstruction to the left and direct reconstruction to the right. The resolution of the reconstruction is provided by the width 1σ band in the y-axis, and is often used as the benchmark for the performance.

Figure 6.7a shows $\theta_{reco} - \theta_{true}$ as a function of E_{true} . The performance of the reconstruction is very similar between the two methods, and are both centered around 0. Direct reconstruction gets slightly better resolutions above energies of around 50 GeV.

Figure 6.7a shows the relative difference between E_{reco} and E_{true} . The table reconstruction shows a better performance in the E than direct reconstruction for all energies. A negative bias (underestimating E) is observed in the table reconstruction present at all energies. Direct reconstruction show a positive bias (overestimating E) across all energies.

The overestimation of E in direct reconstruction follows the trend that was observed previously, where a high oversampling, in general, resulted in a fitted energy above the true value and from this the bias in E can be argued. However, the worse resolution is perhaps a separate issue. From studying the LLH scans in Figure 6.5, it is hard to determine whether the contours in the E LLH-dimension broaden as oversampling increases. The effects from oversampling mostly resemble a shift in E rather than a flattening of the LLH landscape.

For the results shown in Figure 6.7, direct reconstruction was run with the setting *OneGeV*, which sets the energy of the cascade being simulated to 1 GeV at all times. The setting was initially created as a way to use the PCG fit that expects a 1 GeV cascade hypothesis (as described in section 5.7.3). Using *OneGeV* allows for a much bigger oversampling to be used, since a 1 GeV cascade produces a lot less photons, while the photon propagation is the bottleneck of the simulation time. For this reason, an oversampling of 200,000 was used. The motivation behind these settings was based on slight increases in

performance tested on a smaller subset of events in order to determine the final reconstruction settings.

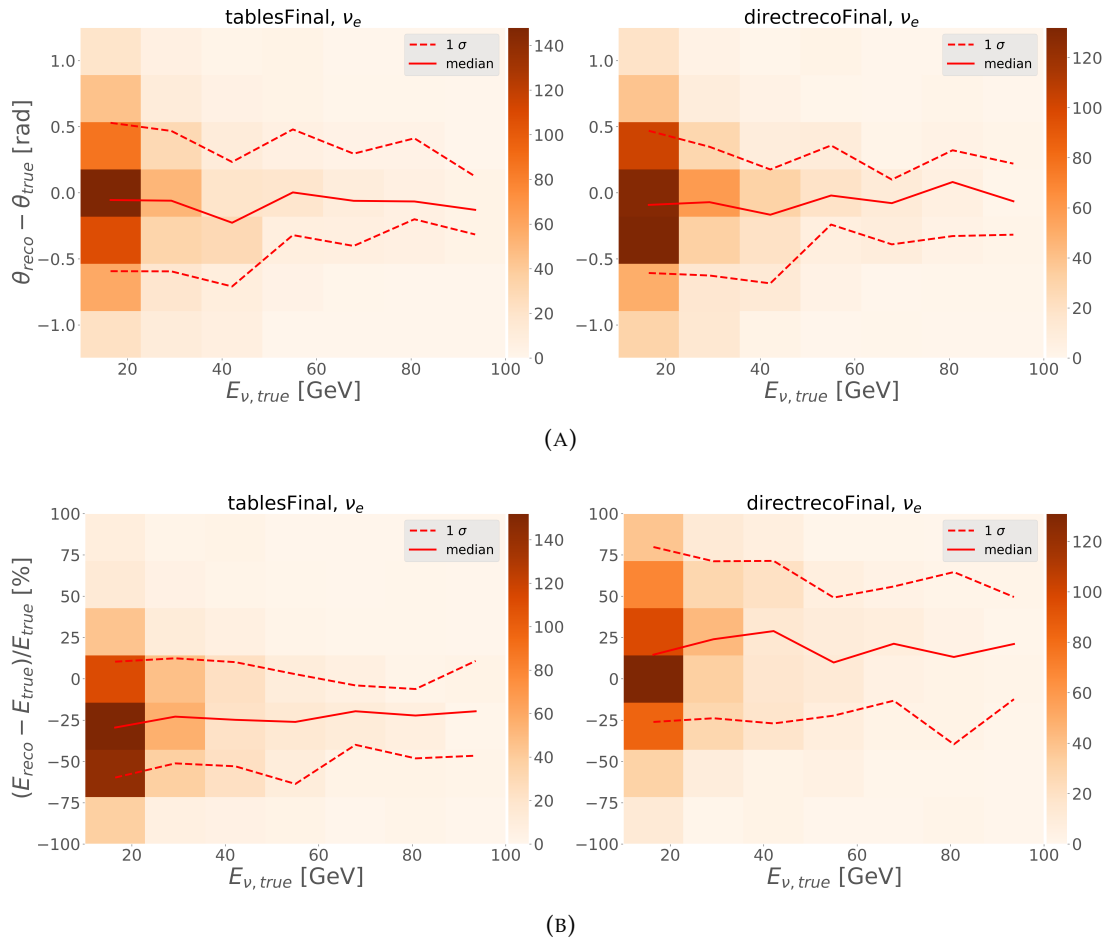


FIGURE 6.7: Final results from DeepCore reconstruction in (A) reconstructed zenith angle θ and (B) reconstructed energy E . Performance of (left) table reconstruction and (right) direct reconstruction is compared. The resolution of the reconstruction is provided by the width 1σ band in the y-axis. The color of the bins indicate the number of events. The majority of the events are at energies between 10 GeV and 20 GeV.

It is worth mentioning that direct reconstruction uses a different LLH function than table reconstruction. Direct reconstruction uses millipedes DIMA-LLH[43], while tables use the Poisson-LLH (the LLH functions are described in section 5.7.2). The DIMA-LLH accounts for statistical uncertainties from simulation by incorporating terms that depend on the number of simulated trials (oversampling). Direct reconstruction can also run using the Poisson-LLH, and was tested as well on the initial subset of events, but was not chosen as the performance slightly decreased. The impact of using either LLH function with direct reconstruction has not been studied in detail in this work, but might be worth investigating in the future, including other possible LLH functions.

6.5 Direct Reconstruction in the ICU

The direct reconstruction code was designed for DeepCore, and had to be modified in order to accommodate the new optical modules. The GCD file used for simulation maps

the instrumentation using two separate keys. The first key *ModuleKey* is defined by the string- and module-number and maps the position and radius of each DOM, which is used in CLSim to define the virtual spheres (as described in section 4.4.1). The second key *OMKey* is defined by the string-, module- and PMT-number and maps the position and orientation of each PMT, and is used by direct simulation to calculate the PMT response. The photons returned from CLSim contain the string and DOM number based on the virtual sphere they intersected, and which is used to create a *ModuleKey* from which the DOM-type can be mapped.

The data samples created for the ICU reconstruction are simulated with the *Deep-Homogeneous* ice model, where the scattering and absorption properties of the ice are identical at all depths. The Deep-Homogeneous ice model provides spatial symmetries in the detector that allow for tables to be constructed using the new multi-PMT modules. However, the ice in IceCube is not homogeneous, and the tables currently used for reconstruction in the ICU cannot be used for real data. Direct reconstruction is one of the potential reconstruction methods where realistic ice models can be used in combination with the new multi-PMT modules. Since the data samples are based on the Deep-Homogeneous ice model, the same ice model is currently used for the simulation in direct reconstruction.

6.6 Determining Reconstruction Settings

Initially, tests were run confirming that the energy fit and oversampling relationship was still present. However, even at the highest oversampling factors tested, the energy fits showed an underestimation of E (opposite of what was observed in DeepCore). Preliminary reconstruction results using a small sample of events showed a majority of the events reconstructing $0 E$. The effect was present using both energy fitting methods (minimizer and PCG).

Reconstructing $E = 0$ indicates that the noise hypothesis used in millipede is the preferred hypothesis. The noise hypothesis in millipede is applied to Λ before calculating the LLH, and is fed to the PCG fit as well. Millipede uses noise rates from the GCD file to create the noise hypothesis, though currently the noise rates for the new modules are manually defined prior to reconstruction.

The effect of the noise hypothesis on the energy reconstruction was tested using a *LowNoise* hypothesis that was implemented by manually reducing all noise rates (lowered 3 orders of magnitude). Reconstructions using the *LowNoise* hypothesis showed less $E = 0$ reconstructions, though a negative bias was still present. In addition, the energy of the cascades being simulated in direct reconstruction was fixed at 20 GeV, down-scaling the computed light yield by a factor 20 as well (representing a 1 GeV cascade) and before the LLH is evaluated, the light yield is rescaled by the energy determined from the minimizer or the PCG fit. This prevented additional events from reconstructing $E = 0$, as it ensured that low energy events produced enough photons to properly represent the light distribution.

The oversampling factor was tested for values between 10^2 and 10^4 , showing no significant improvements for oversampling factors above 5000, and was chosen as the oversampling for the initial reconstruction. The reconstruction sample contains 198 events with energies between 10 and 100 GeV. The energy distribution of the reconstruction data sample is shown in Figure 6.8, indicating that most events in the sample have energies around 10 GeV. The results from the reconstruction is shown in Figure 6.9a and 6.9a for θ

and E respectively. The results are shown as 1D histograms as the sample is too small for it to be binned in energy.

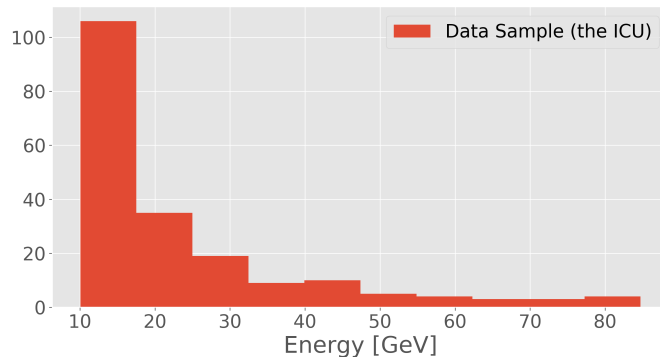


FIGURE 6.8: Distribution of energies in the data sampled used for direct reconstruction in the ICU.

The change in performance in the ICU can be estimated from the reconstruction in DeepCore shown in Figure 6.7. The performance in θ is roughly the same for the DeepCore and the ICU direct reconstruction, when comparing the first energy bin. However, the performance in E improved a lot in terms of the resolution (factor 2 if comparing the first energy bin). The bias in the reconstructed E is opposite in DeepCore and the ICU, and it is still uncertain why this is the case.

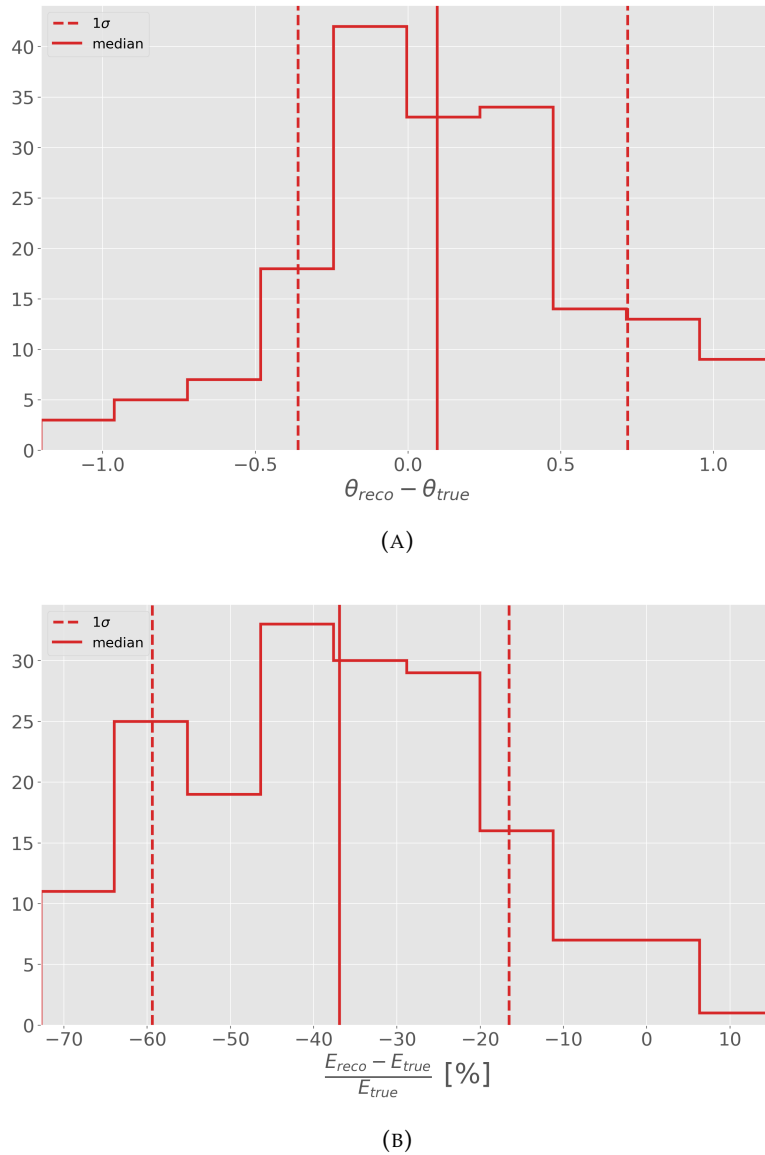


FIGURE 6.9: Results from the initial reconstruction in the ICU. (A) shows the performance in reconstructed θ , while (b) show the performance in reconstructed E .

6.7 Investigating Badly Reconstructed Events

The reconstructed θ did not show any improvements in going from DeepCore to the ICU reconstruction. The direct reconstruction was expected to perform a lot better in the ICU, as the denser spacing and new modules provide a lot more information for the reconstruction. As a result, the behavior of θ was investigated. Some of the events from the initial reconstruction sample showed very poorly reconstructed θ . It was observed that in the majority events with a poorly reconstructed θ the minimizer did not move away from the initial seed which was badly fitted as well. The events with the worst θ reconstruction were investigated to determine whether the issue was related to the LLH landscape or the minimization process.

The minimizer movement in θ -dimension for one of the poorly reconstructed events is shown in Figure 6.10a. The minimizer can be seen stepping in the direction of the true value of θ , but as indicated by the color scale these moves returned bad LLH evaluations,

and as a result, only a small region in θ -space was explored. From the figure it is hard to know whether the bad evaluations were due to the LLH space of θ not being good, or if it was caused by movement in one of the other six dimensions.

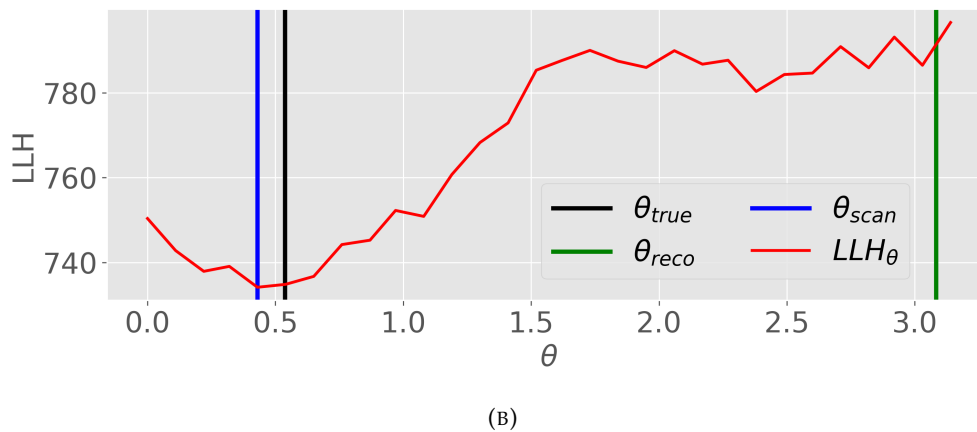
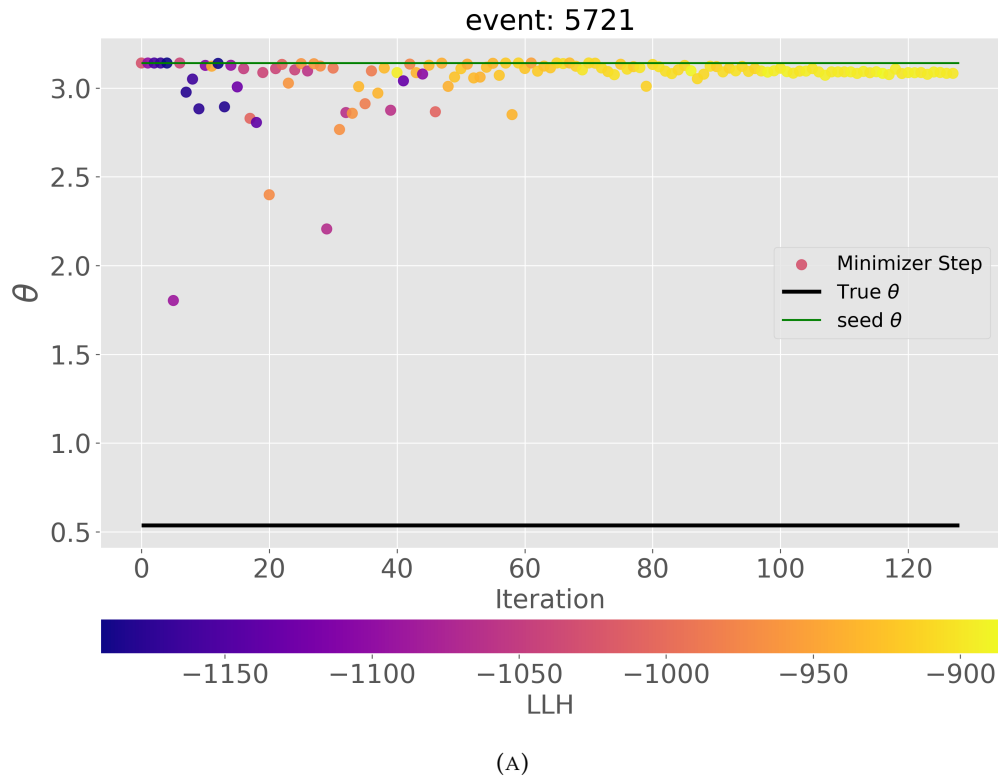


FIGURE 6.10: (A) Minimizer movement of an event with a poorly reconstructed θ . The minimizer does not move away from the bad initial seed shown by the green line. (B) 1D LLH scan in θ using the parameters from the final reconstruction of the event in (A). The scan indicates that at better LLH minimum in the θ dimension exists or which the minimizer was not able to find.

Figure 6.10 shows a 1-dimensional LLH scan in θ for the same event, with all parameters fixed at the final reconstruction of the event, except θ that is scanned. The black line shows the true value of θ , the green line shows the reconstructed θ and the blue line shows the best fit θ from the scan. θ was scanned at 30 points from 0 to π . At each θ the LLH was evaluated 5 times and the best LLH at each θ is shown by the red line. From the

red line it is clear that a better position in θ -space is available, that was not explored by the minimizer as it stopped. This indicates that a bad reconstruction in θ may be caused by the θ -space not being properly explored by the minimizer, rather than the LLH-space itself being inaccurate (though it is possible as well).

As improper exploration in θ -space might cause poorly reconstructed θ , scans were made in θ for all events in the reconstruction sample, based on the final reconstruction (as in Figure 6.10b). The best fit θ of the post-reconstruction scans are shown in Figure 6.9 along with the originally reconstructed θ . The post-reconstruction scan-fits improve the resolution of θ and further indicate that better places in the LLH space can be obtained than what was gotten from the reconstruction.

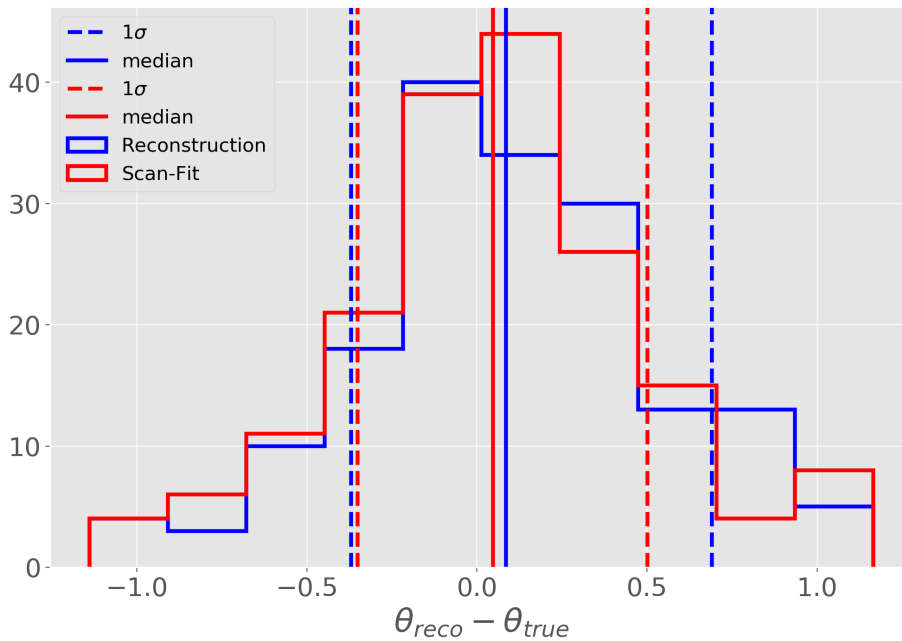


FIGURE 6.11: Comparison between (blue) θ from a full reconstruction and (red) post-reconstruction 1D-scan best fit of θ .

6.8 High Oversampling

As discussed in the previous section, issues in the minimization process are most likely the cause of badly reconstructed events, as some dimensions are not being properly explored. New reconstructions were run on some of the bad events using an oversampling factor of 20,000 in order to see whether reducing the uncertainty in the LLH evaluations could improve the minimization process. Events were reconstructed for each of the energy fitting methods to investigate the impact on the energy fit at higher oversampling. In the high oversampling reconstructions, some events showed a significant improvement in the reconstruction of θ , as the minimizer was able to move away from the bad initial seed.

Figure 6.12a and 6.12b show the minimizer movement from the initial reconstruction using 5000 oversampling. Figure 6.12c and 6.12d show the minimizer movement for the new reconstruction using oversampling of 20,000 and no PCG energy fit.

The results from the reconstructions using 20,000 oversampling indicate that the instability of the LLH might be a significant issue in the minimization process, which is reduced by a higher oversampling factor. However, it should be noted that using a very high oversampling significantly increases the reconstruction time. The reconstruction time of the event in Figure 6.12 from the initial reconstruction sample using 5000 oversampling took a total of 3 hours to complete, whereas the new reconstruction took 16.5 hours to complete.

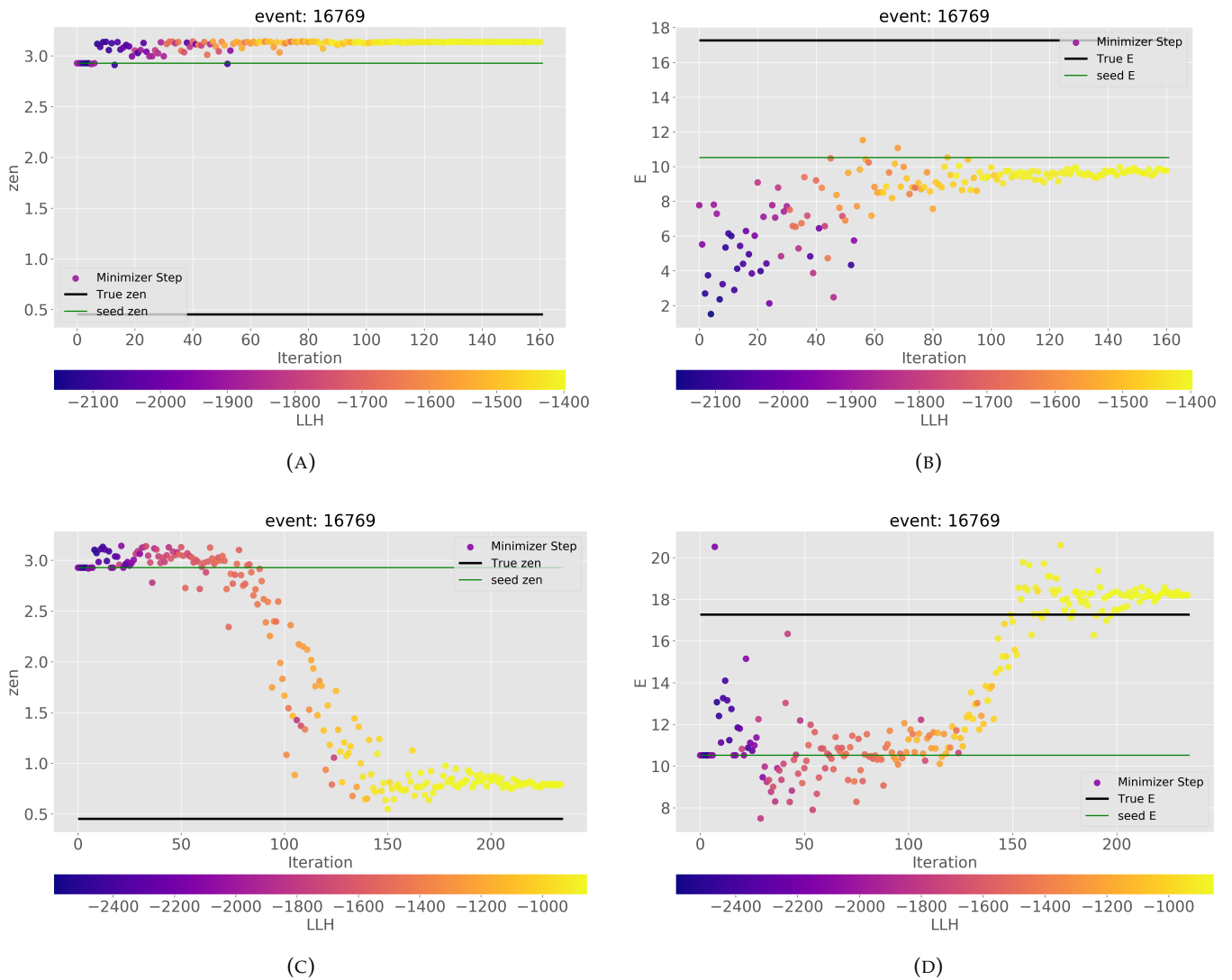


FIGURE 6.12: Minimizer movement in θ and E space from the reconstruction of an event using (a-b) 5000 oversampling and (c-d) 20,000 oversampling.

6.9 Future Work

This section highlights some of the observations that were made during the investigation of direct reconstruction algorithm, but was never explicitly tested because of time limitations and priorities.

6.9.1 Simulation and PMT Response

The Monte Carlo simulation currently used in direct reconstruction does not include the GENIE generator. GENIE is the code that generates particles from neutrino interactions, while GEANT4 and PROPOSAL propagate the particles and generate photons. The direct simulation is currently based on a cascade parametrization modeled as a point-like emission source. Potential improvements in the direct reconstruction could be obtained from using the full simulation though it might come at a cost in runtime, which is already a pressing issue.

In addition, the linear relationship between the energy of the cascade being simulated and the oversampling used was never fully verified. Tests should be made confirming that a 1 GeV cascade being simulated 20 times corresponds to a 20 GeV cascade being simulated once, which has been the assumption.

The photons in direct simulation are currently being treated slightly different than how they are treated when constructing the spline-tables. When tables are constructed, the photons returned from the photon propagation in CLSim are either accepted or rejected based on the calculated detection probability. If the photon is accepted, it counts as 1 PE in the associated bin. In direct simulation, photons are not accepted or rejected, and what is saved in the associated time bin is the detection probability. It is uncertain whether the result of the two methods give identical results, but it might be worth investigating.

6.9.2 LLH Stability and Minimization

As shown in Figure 6.2, the LLH value computed using the same hypothesis can fluctuate a lot, depending on the oversampling factor being used. Possible issues in the minimization process from the instability of the LLH at low oversampling was observed in the ICU reconstruction.

Having a fluctuating LLH caused by statistical uncertainties from the simulation might result in the minimizer sometimes being discouraged from moving in the correct direction if the hypothesis being evaluated computes an unlucky LLH. Currently, the only way to mitigate the uncertainty of the LLH is by increasing the oversampling factor, in turn increasing the reconstruction time.

The statistical uncertainties from the simulation are not present in the same way for the spline-tables as for direct simulation, during the minimization process. Even though the spline fits are affected by the statistical uncertainties of the simulation, the LLH being computed when evaluating a hypothesis is the same every time; thus instability in the LLH is not present during the minimization process, as seen from the perspective of the minimizer. Whether this effect is what separates the performance of direction reconstruction and table reconstruction has not been concluded.

7 Conclusion

It has been shown in this thesis that direct reconstruction is a functional reconstruction method, though it is still faced by some fundamental issues that must be studied and corrected.

From the investigation of the direct reconstruction algorithm, trends were observed in the reconstructed energy for increasing oversampling. It was shown that with the removal of the time bins in millipede the trend disappeared. However, removing the time bins entirely is not a proper solution to the problem, as the time bins are important for other reconstruction parameters such as θ .

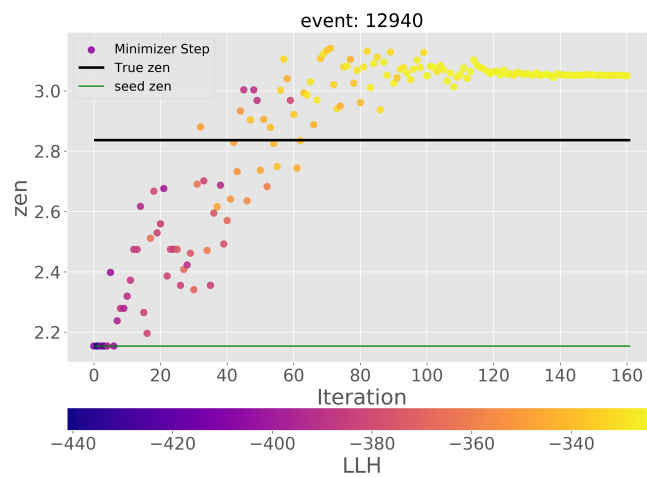
The final results from DeepCore show comparable performance in reconstructed θ between the direct reconstruction and table reconstruction methods. Direct reconstruction is still being outperformed by table reconstruction in E , especially at low energies. In theory, direct reconstruction should perform just as well or better than the table reconstruction, since the light yield is calculated using a direct simulation instead of a multi-dimensional spline fit parameterization. Why direct reconstruction is still being outperformed is not a simple question, and might depend on several different issues.

As shown from the direct reconstruction in the ICU, badly reconstructed events might be related to issues in the minimization process. It was shown that often when given a bad initial seed the minimizer did not properly explore the θ dimension. Tests redoing the reconstruction using an oversampling of 20,000 instead of 5000, which was initially used, showed a significant improvement for some of the badly reconstructed events, though at the cost of a much longer reconstruction time.

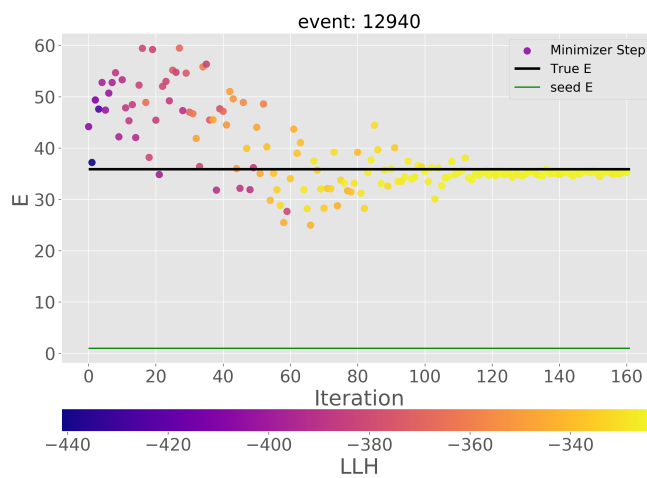
From the results in the ICU, the direct reconstruction method has been shown to work correctly using the new geometry and the new multi-PMT modules. The direct reconstruction method has shown some potential, and might become a viable candidate for replacing tables in the future, as new reconstruction methods are needed for the ICU. However, improvements in the performance and reconstruction times are still needed for it to become a viable reconstruction method, and solutions must be found for some of the issues addressed in this thesis.

For the next step in the development of the direct reconstruction method, checks must be made of the fundamental lower level elements in the direct simulation as well as the minimization process. The effects of oversampling and time binning should be rigorously investigated, down to the level of impact on individual DOMs. In addition, it should be understood how the statistical uncertainties on the log-likelihood evaluations affect the minimizer's behavior, and whether increasing oversampling is the only solution to this problem.

A Minimizer Movement

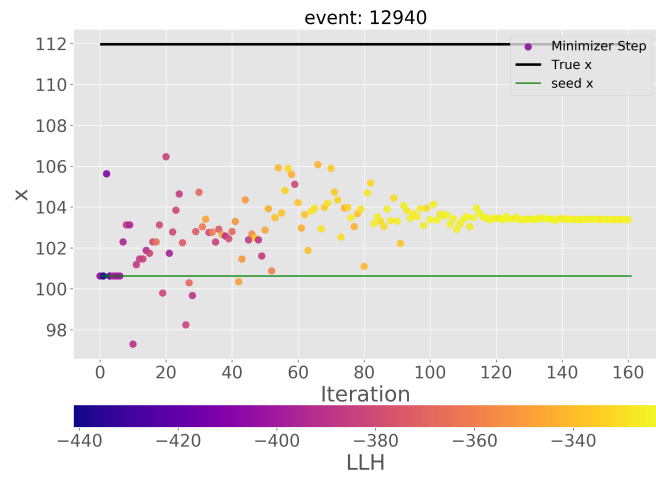


(A)

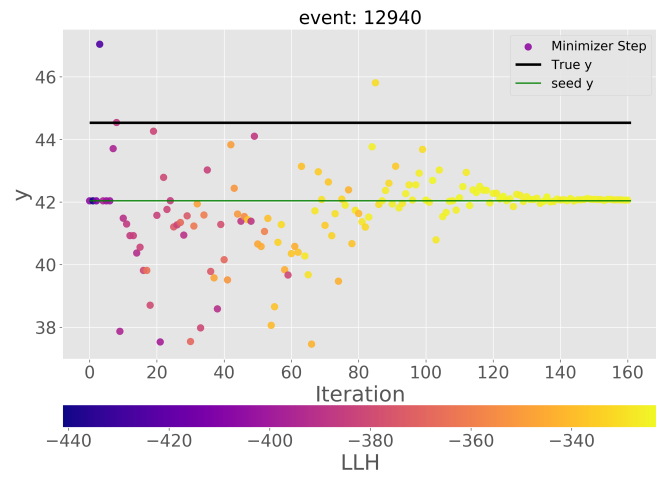


(B)

FIGURE A.1: (a) Movements in (b) Anti-neutrino cross section as a function of energy, shown for different nucleon scattering processes.

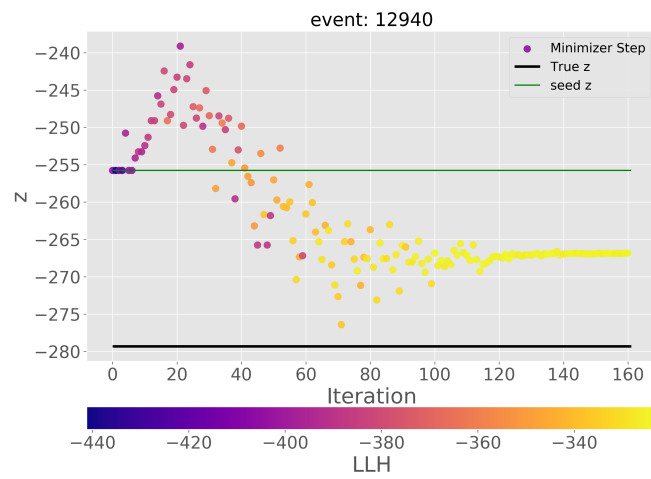


(A)

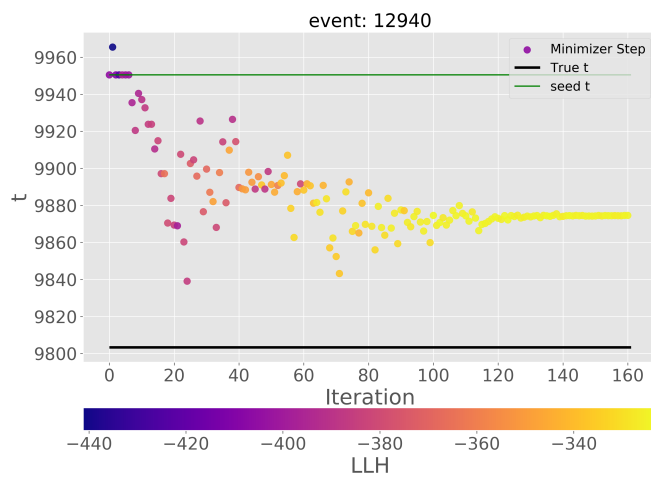


(B)

FIGURE A.2: (a) Movements in (b) Anti-neutrino cross section as a function of energy, shown for different nucleon scattering processes.

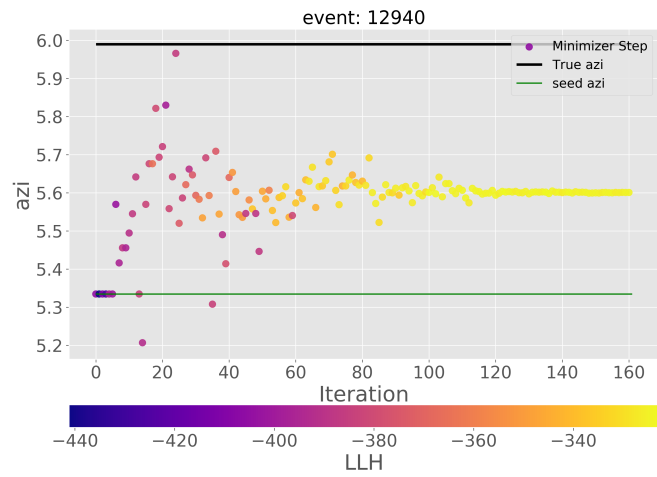


(A)



(B)

FIGURE A.3: (a) Movements in (b) Anti-neutrino cross section as a function of energy, shown for different nucleon scattering processes.



(A)

FIGURE A.4: (a) Movements in (b) Anti-neutrino cross section as a function of energy, shown for different nucleon scattering processes.

Bibliography

- [1] W. Pauli. “Dear radioactive ladies and gentlemen”. In: *Phys. Today* 31N9 (1978), p. 27.
- [2] Enrico Fermi. “Tentativo di una teoria dell’emissione dei raggi beta”. In: *Ric. Sci.* 4 (1933), pp. 491–495.
- [3] S. Schael et al. “Precision electroweak measurements on the Z resonance”. In: *Phys. Rept.* 427 (2006), pp. 257–454. DOI: [10.1016/j.physrep.2005.12.006](https://doi.org/10.1016/j.physrep.2005.12.006). arXiv: [hep-ex/0509008](https://arxiv.org/abs/hep-ex/0509008) [hep-ex].
- [4] Wikipedia contributors. *Chirality (physics)*. [Online; accessed 28-Aug-2019]. 2019. URL: [https://en.wikipedia.org/wiki/Chirality_\(physics\)](https://en.wikipedia.org/wiki/Chirality_(physics)).
- [5] C. S. Wu et al. “Experimental Test of Parity Conservation in Beta Decay”. In: *Phys. Rev.* 105 (1957), pp. 1413–1414. DOI: [10.1103/PhysRev.105.1413](https://doi.org/10.1103/PhysRev.105.1413).
- [6] Takaaki Kajita. “ATMOSPHERIC NEUTRINOS AND DISCOVERY OF NEUTRINO OSCILLATIONS”. In: *Proc. Japan Acad.* B86 (2010), pp. 303–321. DOI: [10.2183/pjab.86.303](https://doi.org/10.2183/pjab.86.303).
- [7] X. Qian and P. Vogel. “Neutrino Mass Hierarchy”. In: *Prog. Part. Nucl. Phys.* 83 (2015), pp. 1–30. DOI: [10.1016/j.pnpnp.2015.05.002](https://doi.org/10.1016/j.pnpnp.2015.05.002). arXiv: [1505.01891](https://arxiv.org/abs/1505.01891) [hep-ex].
- [8] P. A. R. Ade et al. “Planck 2015 results. XIII. Cosmological parameters”. In: *Astron. Astrophys.* 594 (2016), A13. DOI: [10.1051/0004-6361/201525830](https://doi.org/10.1051/0004-6361/201525830). arXiv: [1502.01589](https://arxiv.org/abs/1502.01589) [astro-ph.CO].
- [9] Marius Wallraff and Christopher Wiebusch. “Calculation of oscillation probabilities of atmospheric neutrinos using nuCraft”. In: *Comput. Phys. Commun.* 197 (2015), pp. 185–189. DOI: [10.1016/j.cpc.2015.07.010](https://doi.org/10.1016/j.cpc.2015.07.010). arXiv: [1409.1387](https://arxiv.org/abs/1409.1387) [astro-ph.IM].
- [10] P. F. de Salas et al. “Status of neutrino oscillations 2018: 3σ hint for normal mass ordering and improved CP sensitivity”. In: *Phys. Lett.* B782 (2018), pp. 633–640. DOI: [10.1016/j.physletb.2018.06.019](https://doi.org/10.1016/j.physletb.2018.06.019). arXiv: [1708.01186](https://arxiv.org/abs/1708.01186) [hep-ph].
- [11] K. A. Olive et al. “Review of Particle Physics”. In: *Chin. Phys.* C38 (2014), p. 090001. DOI: [10.1088/1674-1137/38/9/090001](https://doi.org/10.1088/1674-1137/38/9/090001).
- [12] Morten A. Medici. “Search for Dark Matter Annihilation in the Galactic Halo using IceCube”. PhD thesis. Niels Bohr Institute, University of Copenhagen, Nov. 2016.
- [13] J. A. Formaggio and G. P. Zeller. “From eV to EeV: Neutrino cross sections across energy scales”. In: *Rev. Mod. Phys.* 84 (3 2012), pp. 1307–1341. DOI: [10.1103/RevModPhys.84.1307](https://doi.org/10.1103/RevModPhys.84.1307). URL: <https://link.aps.org/doi/10.1103/RevModPhys.84.1307>.
- [14] M. G. Aartsen et al. “Energy Reconstruction Methods in the IceCube Neutrino Telescope”. In: *JINST* 9 (2014), P03009. DOI: [10.1088/1748-0221/9/03/P03009](https://doi.org/10.1088/1748-0221/9/03/P03009). arXiv: [1311.4767](https://arxiv.org/abs/1311.4767) [physics.ins-det].
- [15] R. Abbasi et al. “The Design and Performance of IceCube DeepCore”. In: *Astropart. Phys.* 35 (2012), pp. 615–624. DOI: [10.1016/j.astropartphys.2012.01.004](https://doi.org/10.1016/j.astropartphys.2012.01.004). arXiv: [1109.6096](https://arxiv.org/abs/1109.6096) [astro-ph.IM].

- [16] Julien Nou et al. "A new approach to the real-time assessment of the clear-sky direct normal irradiance". In: *Applied Mathematical Modelling* 40 (Mar. 2016). DOI: [10.1016/j.apm.2016.03.022](https://doi.org/10.1016/j.apm.2016.03.022).
- [17] M. G. Aartsen et al. "The IceCube Neutrino Observatory: Instrumentation and On-line Systems". In: *JINST* 12.03 (2017), P03012. DOI: [10.1088/1748-0221/12/03/P03012](https://doi.org/10.1088/1748-0221/12/03/P03012). arXiv: [1612.05093](https://arxiv.org/abs/1612.05093) [astro-ph.IM].
- [18] A Achterberg et al. "First year performance of the Ice Cube neutrino telescope". In: (Aug. 2019).
- [19] University of Wisconsin-Madison Physical Sciences Lab. *Photograph of Digital Optical Module*. [Online; accessed 8-Aug-2019]. URL: <http://www.ps1.wisc.edu/projects/large/icecube/more-icecube/dom>.
- [20] Albert Einstein. "Über einen die Erzeugung und Verwandlung des Lichtes betreffenden heuristischen Gesichtspunkt. (German) [On the production and transformation of light from a heuristic viewpoint]". German. In: 322.6 (1905). English translation in [Arons:1965:EPP], pp. 132–148. ISSN: 0003-3804 (print), 1521-3889 (electronic). DOI: <https://doi.org/10.1002/andp.19053220607>. URL: <http://www.gsjournal.net/Science-Journals/Essays/View/2490>; <http://www.gsjournal.net/Science-Journals/Essays/View/2491>; <http://www.zbp.univie.ac.at/einstein/einstein1.pdf>.
- [21] Sumit Kumar. *Schematic of a photomultiplier tube*. [Online; accessed 8-Aug-2019]. URL: <http://analyticalprofessional.blogspot.com/2013/05/photomultiplier-tube.html>.
- [22] R. Abbasi et al. "Calibration and characterization of the IceCube photomultiplier tube". In: *Nuclear Instruments and Methods in Physics Research Section A: Accelerators, Spectrometers, Detectors and Associated Equipment* 618.1 (2010), pp. 139–152. ISSN: 0168-9002. DOI: <https://doi.org/10.1016/j.nima.2010.03.102>. URL: <http://www.sciencedirect.com/science/article/pii/S0168900210006662>.
- [23] Nathan Bramall et al. "A deep high-resolution optical log of dust, ash, and stratigraphy in South Pole glacial ice". In: *Geophys. Res. Lett* 32 (Nov. 2005). DOI: [10.1029/2005GL024236](https://doi.org/10.1029/2005GL024236).
- [24] Martin Rongen. "Measuring the optical properties of IceCube drill holes". In: *EPJ Web Conf.* 116 (2016), p. 06011. DOI: [10.1051/epjconf/201611606011](https://doi.org/10.1051/epjconf/201611606011).
- [25] M. G. Aartsen et al. "Measurement of South Pole ice transparency with the IceCube LED calibration system". In: *Nucl. Instrum. Meth.* A711 (2013), pp. 73–89. DOI: [10.1016/j.nima.2013.01.054](https://doi.org/10.1016/j.nima.2013.01.054). arXiv: [1301.5361](https://arxiv.org/abs/1301.5361) [astro-ph.IM].
- [26] Michael J. Larson. "A Search for Tau Neutrino Appearance with IceCube-DeepCore". PhD thesis. Niels Bohr Institute, University of Copenhagen, June 2018.
- [27] M. G. Aartsen et al. "Measurement of Atmospheric Tau Neutrino Appearance with IceCube DeepCore". In: *Phys. Rev. D* 99.3 (2019), p. 032007. DOI: [10.1103/PhysRevD.99.032007](https://doi.org/10.1103/PhysRevD.99.032007). arXiv: [1901.05366](https://arxiv.org/abs/1901.05366) [hep-ex].
- [28] IceCube collaboration. *NSF mid-scale award sets off the first extension of IceCube*. [Online; accessed 8-Aug-2019]. URL: <https://icecube.wisc.edu/news/view/661>.
- [29] IceCube collaboration, Niels Bohr Institute. *NSF Awards Funding for the IceCube Upgrade*. [Online; accessed 8-Aug-2019]. URL: <https://icecube.nbi.ku.dk/nsf-awards-funding-for-the-icecube-upgrade/>.

- [30] Lew Classen et al. "The mDOM - A multi-PMT digital optical module for the IceCube-Gen2 neutrino telescope". In: *PoS ICRC2017* (2018), p. 1047. DOI: [10.22323/1.301.1047](https://doi.org/10.22323/1.301.1047).
- [31] D. Heck et al. "CORSIKA: A Monte Carlo code to simulate extensive air showers". In: (1998).
- [32] C. Andreopoulos et al. "The GENIE Neutrino Monte Carlo Generator". In: *Nucl. Instrum. Meth. A*614 (2010), pp. 87–104. DOI: [10.1016/j.nima.2009.12.009](https://doi.org/10.1016/j.nima.2009.12.009). arXiv: [0905.2517](https://arxiv.org/abs/0905.2517) [hep-ph].
- [33] S. Agostinelli et al. "GEANT4: A Simulation toolkit". In: *Nucl. Instrum. Meth. A*506 (2003), pp. 250–303. DOI: [10.1016/S0168-9002\(03\)01368-8](https://doi.org/10.1016/S0168-9002(03)01368-8).
- [34] Dmitry Chirkin and Wolfgang Rhode. "Muon Monte Carlo: A High-precision tool for muon propagation through matter". In: (2004). arXiv: [hep-ph/0407075](https://arxiv.org/abs/hep-ph/0407075) [hep-ph].
- [35] Dmitry Chirkin. "Photon Propagation with GPUs in IceCube". In: *Proceedings, GPU Computing in High-Energy Physics (GPUHEP2014): Pisa, Italy, September 10-12, 2014*. 2015, pp. 217–220. DOI: [10.3204/DESY-PROC-2014-05/40](https://doi.org/10.3204/DESY-PROC-2014-05/40).
- [36] John E. Stone, David Gohara, and Guochun Shi. "OpenCL: A Parallel Programming Standard for Heterogeneous Computing Systems". In: *Computing in science & engineering* 12.3 (2010). 21037981[pmid], pp. 66–72. ISSN: 1521-9615. DOI: [10.1109/MCSE.2010.69](https://doi.org/10.1109/MCSE.2010.69). URL: <https://www.ncbi.nlm.nih.gov/pubmed/21037981>.
- [37] Y. Hasegawa. *Analysis of Charge Response functions of the IceCube PMTs*. URL: <http://www.ppl.phys.chiba-u.jp/research/IceCube/pmt/SPE/CRAanalysis.html>.
- [38] IceCube collaboration. *Direct Reconstruction*. [Online; accessed 17-Aug-2019]. URL: https://wiki.icecube.wisc.edu/index.php/Direct_reconstruction.
- [39] Sarah Nowicki. *DirectReco update - in transition*. [Online; accessed 18-Aug-2019]. URL: https://events.icecube.wisc.edu/event/106/contributions/1220/attachments/911/993/madison_recosyst_directreco_update_05032019.pdf.
- [40] Alexander Wallace. "Direction Reconstruction of IceCube Neutrino Events with Millipede". MA thesis. The University of Adelaide, School of Physical Sciences, Department of Physics, May 2016.
- [41] G I Angelis et al. "The performance of monotonic and new non-monotonic gradient ascent reconstruction algorithms for high-resolution neuroreceptor PET imaging". In: *Physics in medicine and biology* 56 (July 2011), pp. 3895–917. DOI: [10.1088/0031-9155/56/13/010](https://doi.org/10.1088/0031-9155/56/13/010).
- [42] John A. Nelder and Roger Mead. "A simplex method for function minimization". In: *Computer Journal* 7 (1965), pp. 308–313.
- [43] Dmitry Chirkin. "Likelihood description for comparing data with simulation of limited statistics". In: *arXiv e-prints*, arXiv:1304.0735 (2013), arXiv:1304.0735. arXiv: [1304.0735](https://arxiv.org/abs/1304.0735) [astro-ph.IM].